Graphene Quantum Dot Based Electronic Devices

Xuan Pan

Doctor of Philosophy

August 2018

Department of Electrical and Electronic Engineering

THE UNIVERSITY OF MELBOURNE

Submitted in partial fulfilment of the requirement of the degree

To my beloved father and mother

ABSTRACT

Among all graphene derivatives, the graphene quantum dot (GQD), a fragment limited in size, or domains, of a single-layer two-dimensional graphene crystal, has been investigated with much interest by the global research community, because of its unique electrical, optical and mechanical properties that arise from quantum confinement effects. Among all properties, negative differential resistance (NDR) has been of particular interest. NDR devices exhibit abnormal electrical characteristics, for instance, the non-ohmic current-voltage (I-V) curve, which enables a number of very important applications. An understanding of the electronic band structure may help build a deeper insight into the NDR phenomenon and guide the building of GQD based devices.

This thesis uses models of electronic band structure from solid-state physics and relates the impact of band structure on observed NDR effect. Attention is also given to evaluate electronic transport properties of GQD based two-terminal devices, specifically energy filters and resistor-type memory devices (memristors), by using a non-equilibrium Green function technique implemented within the framework of extended Hückel method. All the numerical simulations use the platform in the commercial Atomistix ToolKit (ATK) package.

A two-dimensional GQD structure is shown to offer a promising route for the design of electron energy filters to produce low-power and low-noise electronics as well as volatile memristors utilizing only single layer graphene.

DECLARATION

This is to certify that:

i. the thesis comprises only my original work towards the PhD except where indicated in the Preface,

ii. proper acknowledgement has been made in the text to all other materials used,

iii. the thesis is fewer than 100 000 words in length, exclusive of tables, figures, bibliographies and appendices.

Signed: Xuan PAN

Name: Xuan Pan

Date: August 23rd, 2018

PREFACE

This thesis summarizes the research I performed in the Graphene Electronics Group of Prof. Stan Skafidas at the "Center for Neural Engineering" from 2015 to 2018. The research work would have been impossible to complete without receiving support and help in a few different ways.

The concept referred to in Chapter 3 and 4 were originally stemmed from myself and my supervisor Prof. Stan Skafidas. The data collection and analysis in Chapter 3-5 are my original work. Experiments conducted in Chapter 5 were supported under a form of research collaboration by Dr Omid Kavehei at RMIT University and Dr Kumar Ganesan at the University of Melbourne.

Chapter 3 of this thesis has been published in a journal as X. Pan, W. Qiu, and E. Skafidas, "Energy-filtered Electron Transport Structures for Low-power Low-noise 2-D Electronics", *Sci. Rep.*, vol. 6, Oct. 2016, and in a conference paper as X. Pan and E. Skafidas, "Structure-property relationships for graphene quantum dot based electronic devices", in *International Conference on Nanoscience and Nanotechnology (ICONN)*, 2018, pp. 541. Chapter 4 of this thesis has been published in a journal as X. Pan and E. Skafidas, "Resonant tunneling based graphene quantum dot memristors", *Nanoscale*, vol. 8, no. 48, pp. 20074–20079, Dec. 2016. In all the publications, I was responsible for the data collection and analysis as well as the manuscript composition. W. Qiu contributed to manuscript edits. E. Skafidas is the supervisory author and was involved with concept formation and manuscript edits.

ACKNOWLEDGEMENT

To my parents, Feng Pan and Ping Sheng: because I owe it all to you. Many thanks for providing me through moral and emotional support in my life! I am also grateful to my other family members and friends who have supported me along the way.

My primary supervisor Prof. Stan Skafidas: thank you for the continuous support of my Ph.D. study. His immense knowledge and rich experience helped me in all the time of research. The rest of my research advisory committee, ex co-supervisor Dr. Wanzhi Qiu, co-supervisor Porf. Kenneth Crozier, and chair Prof. Ampalavanapillai Nirmalathas: thank you for insightful comments and encouragement which motivated me to widen my research in various perspectives.

A very special gratitude goes out to all down at CQC^2T, MNRF and MNTF for helping and supporting the experiment work.

With a special mention to Dr. Babak Nasr, Dr. Kumar Ganesan, Dr. Brett Johnson, Dr. Dru Morrish and Associate Professor Sharath Sriram, it was fantastic to have the opportunity to work majority of my experiment program in your facilities.

And finally, last but not the least, also to everyone in the CfNE. It was great sharing laboratory with all of you during last three and a half years.

TABLE OF CONTENTS

LIST OF FIGURES

LIST OF TABLES

LIST OF ABBREVIATIONS

2D	Two-dimensional
2DEG	Two-dimensional Electron Gas
GQD	Graphene Quantum Dot
GNR	Graphene Nanoribbon
QD	Quantum Dot
CD	Carbon Dot
NDR	Negative Differential Resistance
NFT	Nearly Free Electron
TB	Tight-binding
DFT	Density Functional Theory
EHT	Extended Hückel Theory
ATK-SE	ATK-SemiEmpirical
AO	Atomic-orbital
rGO	Reduced Graphene Oxide
GO	Graphene Oxide
GrO	Graphite Oxide
HOPG	Highly Oriented Pyrolytic Graphite
CVD	Chemical Vapour Deposition
PECVD	Plasma-enhanced Chemical Vapour Deposition
PVD	Physical Vapour Deposition
CMG	Chemical Modified Graphene
GIC	Graphite Intercalated Compound
UHV	Ultrahigh Vacuum
SiC	Silicon Carbide
TiC	Titanium Carbide
h-BN	Hexagonal Boron Nitride
UNCD	Ultrananocrystalline Diamond
IC	Integrated Circuit
NIS	Normal-insulator-superconductor

SLG	Single-layer Graphene
RTA	Rapid Thermal Annealing
CFA	Conventional Furnace Annealing
EBL	Electron Beam Lithography
SNR	Signal-to-noise
PVCR	Peak-to-valley Current Ratio
LCOS	Local Density of States
RF	Radio-frequency
DLC	Diamond-like Carbon
SCD	Single-crystalline Diamond
GB	Grain Boundary
IPA	Isopropanol
DI	Deionized
XRD	X-ray Powder Diffraction
PMMA	Poly (methyl methacrylate)
EL	Ethyl Lactate
MIBK	Methyl Isobutyl Ketone

1. INTRODUCTION

In this thesis, a variety of novel nanoelectronic devices are defined and analysed via stringent quantum-mechanical simulations. Even though all the proposed devices have a diverse range of applications, they are mainly based on one unique electronic property of a GQD structure proposed in this thesis. This property is fundamentally attributed to the GQD distinct band structure. This chapter demonstrates the background of the research introduced in this thesis and points out the motivation behind it. An overview of the thesis is outlined, main contributions in the thesis are elucidated, and a list of derived publications is presented.

1.1. Background

As one of the most primary chemical elements in the universe, carbon has been of significant interest in modern science and technology. Graphene, after being isolated for the first time by Andre Geim and Konstantin Novoselov from the University of Manchester in 2004, has exploded in popularity since the two were awarded the 2010 Nobel Prize in Physics[1]. Studies have shown that this two-dimensional allotrope of carbon is able to provide a promising route for the development of various devices, such as solar cells[3], light emitting diodes[2], Li ion batteries[3], and so forth. Graphene possesses many exceptional thermal, mechanical, chemical and electronic properties, including unparalleled mechanical stiffness, intense elasticity, robust thermal stability, and high electrical conductivity (up to 100,000$cm^2/V{\cdot}s$ at room temperature for exfoliated graphene)[3–5]. These properties result in potential applications of graphene in fuel cells, tissue engineering, supercapacitors, Hall effect sensors, etc[6–9]. Tremendous theoretical and experimental studies have been triggered for the purpose of better understanding and more effectively utilizing this novel material.

1.1.1. Theoretical Research

In the area of theoretical research, significant work has been carried out on the analysis of electronic band structure theory. Despite graphene's many unusual but desirable characteristics, the main drawback of graphene is the zero bandgap which highly limits its widespread applications in low power electronic devices[10]. Although comprehensive research efforts have been focused to deal with this issue, and several pioneering methods are practical to open the energy gap, more innovative and functional strategies are required.

One method to introduce a bandgap is to trim graphene bulk into nanometre-scale pieces, either as graphene nanoribbons (GNRs) or graphene quantum dots (GQDs)[11]. Here quantum confinement, an intrinsic property of materials of finite size stemming from its infinite exciton Bohr radius, is exploited. The bandgap energy of GQD is largely determined by its size and can be made as large as approximately 3eV[11]. GQD-based devices have been reported by a number of research groups to display novel

charge transport phenomena. In comparison to conventional quantum dots (QDs), GQDs possess several other desirable chemical/physical properties, such as low cytotoxicity, consistent chemical inertness, excellent solubility, good biocompatibility, *etc*. As a result, GQDs find widespread applications in biosensors and biological imaging[12], solar cells[13,14], batteries[15], light emitting diodes[16], and so forth. Furthermore, owing to the low cytotoxicity and high biocompatibility features[17], enormous efforts have been devoted to the synthesis of an environmentally friendly substitute for conventional QDs.

In the literature, some researchers refer to carbon dots (CDs) as GQDs. Although they do present similar biocompatibility to other semiconductor QDs[18], these are two structurally unique materials (see Table 1.1)[4,19,20]. CDs are amorphous spherically-shaped carbon nanoparticles with size less than 15nm, whereas GQDs are crystalline nanostructures consisting of fewer than ten layers of graphene with size ranging from around 1.5 to 100nm.

Table 1.1 Differences between GQDs and CDs

	Crystallinity	Components	Scale	Sources for synthesis
GQDs	Crystalline	Single, double or multiple layers of graphene	~1.5-100nm	Graphene-based precursors or materials with graphene-like structures
CDs	Amorphous	Spherical carbon particles	<15nm	Organic precursors

In the early stage, major effort had been applied to the study of GQDs properties and the development of novel strategies to prepare GQDs with acceptable quality. Progressively, the research interest turned toward the physical explanation of GQDs characteristics and the application of GQDs-based technology in electronic, optical and energy storage and conversion devices[3,21,22].

GQDs exhibit high electron mobility at room temperature[5]. In contrast to the diffusion-drift related transport in conventional solids, electrons in a GQD film possess a ballistic form of transport and behave as particles in a viscous flow, which is attributed to different levels of electron-electron interactions. Such a transport behaviour could give rise to multiple unexpected phenomena, among which is the well-known negative differential resistance (NDR) due to the electron movement against the electric field[11,23].

NDR effect describes an unusual characteristic of certain electrical components, in which an increase in the voltage across the device terminals brings about a decrease in the electric current passing through the system. In an ordinary resistor, however, an increase in bias always gives rise to a proportional increase in current. At the macroscopic level, the NDR effect is considered as a critical feature of the current-voltage (I-V) property of resonant tunneling devices.

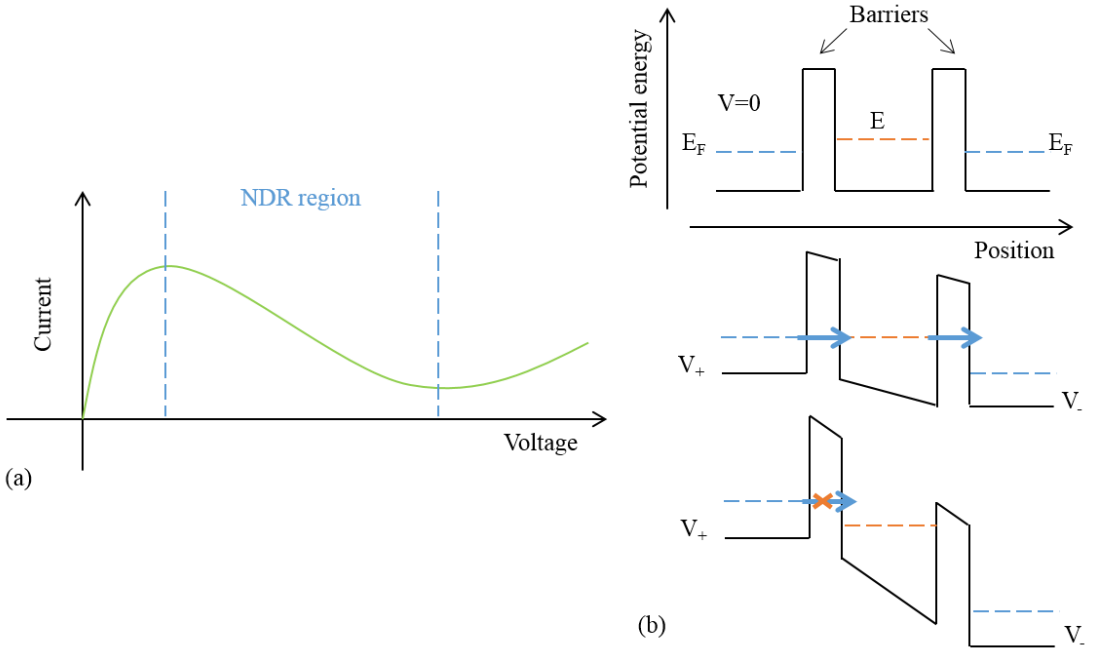

Figure 1.1 (a) A schematic illustration of the NDR phenomenon for resonant tunneling diodes. (b) The intrinsic mechanism responsible for the NDR effect. E_F represents the Fermi level of left and right electrodes, whilst E refers to one quasi-bound state energy level of the well.

The underlying principles of the NDR effect can be understood by the diagram in Fig. 1.1(b), in which one assumption made is that the quantum well of the structure contains only a single quasi-bound state energy level. Resonant tunneling occurs when the electron passes through the energy eigenstate of the quantum well. However, the bias voltage not only changes the chemical potentials of the left and right electrodes, but also distorts the energy bands, including a movement in the position of the quantum well resonant states. The current maximum takes place when the bias voltage applied to the barrier layers shifts the Fermi energy at the cathode side and makes it align with the resonant level in the potential well. Consequently, in experiment, resonant tunneling is manifested as a peak in the tunneling current at the bias voltage near the quasi-stationary state of the quantum well.

In the past few decades, detailed knowledge of the NDR effect was mainly elucidated via the energy band theory particularly with respect to an inclusion of complicated electronic band structures in the quantum orbital motion and electron scattering. The foundation of the most intricate preliminary transport investigations was the Boltzmann transport equation and the Fermi's golden rule to report scattering incidents[24]. Fundamentally, the core of band theory is the examination of the permissible quantum mechanical wave functions and the solution of various mathematical equations, including the important Schrodinger equation whose general time-independent form is[25]:

$$E\psi = H\psi \tag{1.1}$$

where E describes the overall energy of the quantum system under consideration, H is the Hamiltonian operator, ψ is the wave function of the system.

To date, several theories or models have been developed to study the electronic structure of many-body systems, describe certain physical properties and lay the foundation for the intuitive comprehension of solid-state electronics. Among them, the nearly free electron model (NFE model), the tight-binding model (TB model), the density functional theory (DFT) and the extended Hückel theory (EHT) are well-known and regularly used.

1) The NFE model depends on several simplifications but is widely accepted for investigating crystal energy bands. One of the main assumptions is that interactions between electrons are so weak that can be completely ignored, which enables the use of the Bloch's theorem. The theorem points out a fact, which sets the basis for the electronic band structure concept, that electrons under a periodically-repeating environment have wave functions which are periodic along wave vectors and contain a basis comprising of Bloch wave energy eigenstates[26]. Mathematically, the effect of this periodicity can be expressed via the Bloch wave function in the following form[27]:

$$\psi_{n\boldsymbol{k}}(\boldsymbol{r}) = e^{i\boldsymbol{k}\cdot\boldsymbol{r}} u_{n\boldsymbol{k}}(\boldsymbol{r}) \tag{1.2}$$

where ψ is the Bloch wave, n is the band index that refers to the n-th atomic energy level, $\boldsymbol{k}$ is the wave vector representing the direction of the electron motion, $\boldsymbol{r}$ is the position in the crystal lattice, u is a periodic function whose periodicity equals to that of the crystal.

This approximation is particularly useful to calculate the band structure for metallic materials in which the atomic orbital-overlaps are comparatively large. In fact, the NFE-modelled bands are rather similar to the real bands for metals such as Na and Al in both theoretical calculation and experimental practice[25]. However, since NFE model requires a fairly long electron mean-free-path, it behaves poorly for non-metal materials.

2) Contrary to the NFE model, which includes a weak periodic perturbation, in the TB model, interactions between electrons are, to a large extent, considered. This model is also known as the Linear Combination of Atomic Orbitals (LCAO) approximation, generally describing the characteristics of tightly-bound electrons in solid materials. It assumes that the electronic wave function is a linear combination of certain energy- and time-independent orbitals, each related to an identified atom in which electrons are firmly restricted to nuclei. The atomic wave function is defined as[26]

$$\psi_{n\boldsymbol{k}}(\boldsymbol{r}) = \sum_{\boldsymbol{R}} e^{-i\boldsymbol{k}\cdot(\boldsymbol{R}-\boldsymbol{r})} a_n(\boldsymbol{r}-\boldsymbol{R}) \tag{1.3}$$

where $\boldsymbol{R}$ refers to certain atomic site, $a_n(\boldsymbol{r}, \boldsymbol{R})$ is known as the Wannier function and can be expressed as[28]:

$$a_n(\boldsymbol{r}-\boldsymbol{R}) = \frac{V_C}{(2\pi)^3} \int d\boldsymbol{k} e^{-i\boldsymbol{k}\cdot(\boldsymbol{R}-\boldsymbol{r})} u_{n\boldsymbol{k}} \tag{1.4}$$

where V_C is the crystal potential and the integral is applied over the Brillouin zone.

This model provides good qualitative results in materials with finite atomic orbital overlaps, for example, semiconductors and ionic insulators. One of its advantages is that it can predict the properties of the band structure in terms of only a few atomic energy levels and overlap parameters, which can be presented in a simple function composed of the nearest neighbour distances. Besides, the

TB model can be easily combined with the NFE model, resulting in a hybrid NFE-TB method for the description of the wide NFE conduction band and the narrow TB d-band in the case of transition metals[29]. Still, the TB model suffers from some major limitations. Due to its assumptions, the interatomic distances can be too small, and the charges on the atoms or ions in the lattice are wrong. Therefore, the model works reasonably only in the vicinity of atoms, leaving the interstitial regions between atoms unmodeled.

3) In the current nanoscience literature, DFT is the most popular and versatile method employed in the calculation of electronic band plots. As a theory, rather than a model, it studies the structural properties, especially the ground state, of many-electron systems. Even though the laws of quantum mechanics governing the behaviour of electrons can be described using the Schrodinger equation, it is not realistic to get the numerical solutions in the many-electron case, because of the complex inter-electron electrostatic forces of repulsion. Therefore, instead of directly approaching solutions, DFT reformulates the equation such that properties of a many-electron system are purely determined by a functional of the electron density where system energy is minimized. In an *N*-electron system, the one-to-one relationship between the wave function ψ and the ground-state electron density $n(\boldsymbol{r})$ is expressed as[30]:

$$n(\boldsymbol{r}) = N \int d\boldsymbol{r}_2 \cdots d\boldsymbol{r}_N \, \psi(\boldsymbol{r}, \boldsymbol{r}_2, \cdots, \boldsymbol{r}_N) \, \psi^*(\boldsymbol{r}, \boldsymbol{r}_2, \cdots, \boldsymbol{r}_N) \tag{1.5}$$

This means that one matrix density function is sufficient for describing large numbers of electrons. It is no longer required to definitely identify the independent three-dimensional wave functions that constitute the entire election density for any one electron[30–32]. The functional of electron density F[n] is defined in the following form[30,33]:

$$F[n] = T_s[n] + \frac{1}{2} \int n(\boldsymbol{r}) \, \Phi(\boldsymbol{r}) d\boldsymbol{r} + E_{xc}[n] \tag{1.6}$$

where T_s is the system kinetic energy without considering the electron-electron interactions, Φ is the classical Coulomb potential, E_{xc} is the exchange-correlation energy describing the many-body effect.

This method holds a distinct capability of carrying out practical calculations on intricate quantum many-body systems, for instance, large organic molecules. Generally, DFT-calculated electronic bands turn out to be consistent with experimentally ascertained bands, with the band shape being particularly well reproduced. The accuracy of DFT calculation is largely influenced by the knowledge of exchange-correlation energy functionals whose exact expressions are, unfortunately, unknown except for the case of a free electron gas. Therefore, in semiconductors and insulators, the HOMO-to-LUMO band gap is systematically underestimated by an approximately 40%[30]. In addition, the heavy computational burden is also a problem especially for nanodevices calculations.

4) In electronic band structure theories, a specific balance between flexibility and accuracy is required. As mentioned above, empirical methods (such as NFE and TB approaches) are efficient and practical, but are only benchmarked for given geometries and generally not transferable beyond deformations. On the other hand, first-principles techniques (such as DFT-based models) are rigorous but computationally quite prohibitive for systems containing over 200 atoms [34–36]. It is essential to devise a practical compromise, which promotes the development of the EHT principle. The EHT is a semi-empirical technique working with explicit atomic-orbital (AO) basis functions on which the Hamiltonian elements are based in both periodic and non-periodic electronic systems. It calculates electronic interactions in a relatively easy way for which repulsions between electrons are underemphasized and the total energy is merely a linear combination of the term for each electron. The basis functions in EHT are usually Slater-type orbitals (STOs) with the following expression form[36–38]:

$$\Phi_{nlm} = cr^{n-1}e^{-\zeta r}Y_{lm}(\theta, \varphi) \tag{1.7}$$

where c is a normalization coefficient, r is the electron-to-nucleus distance, ζ is the Slater orbital exponent which controls the width of the orbital, Y is the Laplace's spherical harmonics, θ and φ are the spherical angular coordinates, n, l, and m are natural numbers that denotes the principal, azimuthal, and magnetic quantum numbers respectively. The individual AO wave functions are then

estimated by a linear combination of the basis functions, with coefficients and exponents $\{c_i, \zeta_i\}$ fitted for each STO to match the band structure information[36]. The EHT brings about many advantages including a substantial reduction in the amount of parameters required for adjustment, an improvement in parameter transferability under diverse conditions, and intrinsic scaling rules for interactions involved in AOs. It is especially useful in the study of electronic structure and quantum transport for a given material, since up to 1,000 atoms can be easily reached in the simulation[34,35]. Yet, the drawback of this method is also clear. In EHT, adjustments are mainly applied on parameters strongly related to the basis functions and the diagonal elements of the Hamiltonian matrix. As a result, this approach works reasonably for particles such as boron hydrides, because the small gap between boron and hydrogen atomic electronegativity leads to considerably similar diagonal matrix elements, but acts poorly for molecules containing atoms of highly distinct electronegativity[39,40].

1.1.2. Experimental Research

Apart from the theoretical study, the experimental fabrication is the other significant part in the field of graphene-related research. Graphene derivatives such as GQDs are generally prepared based on well-produced graphene sheets via techniques including the strong sonication[61], the lithographic approaches[59], the hydrothermal or electrochemical or plasma treatment[57,58,60], *etc.* Since the now world-renowned Scotch tape exfoliation method realized the first isolation of graphene in 2004 by Andre Geim and Konstantin Novoselov, numerous processes have been developed to produce single, double or few layers of graphene. High electron mobility and low defect density are the two key criteria for high-quality synthesized graphene samples. In terms of the quality and performance, the mechanical exfoliation method is still considered as the best until now, as it produces graphene flakes with electron/hole mobilities (15,000$cm^2V^{-1}s^{-1}$ at the range of 10~100K[41]) and defect densities that are superior to other methods[42]. However, the most obvious disadvantage of this method is the excessive processing time which greatly reduces the possibility of its application in large scale production. Yet, long-standing interest continuously exists in the production of large-scale graphene appropriate for applications in flexible electrical and electronic devices. Important

concerns in the mass production include the quality and conformity among samples as well as the cost and intrinsic difficulty of the method.

To date, a tremendous amount of graphene production techniques has been developed to meet various requirements. For the sake of a systematic comparison, an agreement has been reached among researchers to split graphene synthesis into two categories: the "top-down" and "bottom-up" approach. Fig. 1.2 briefly illustrates the two procedures.

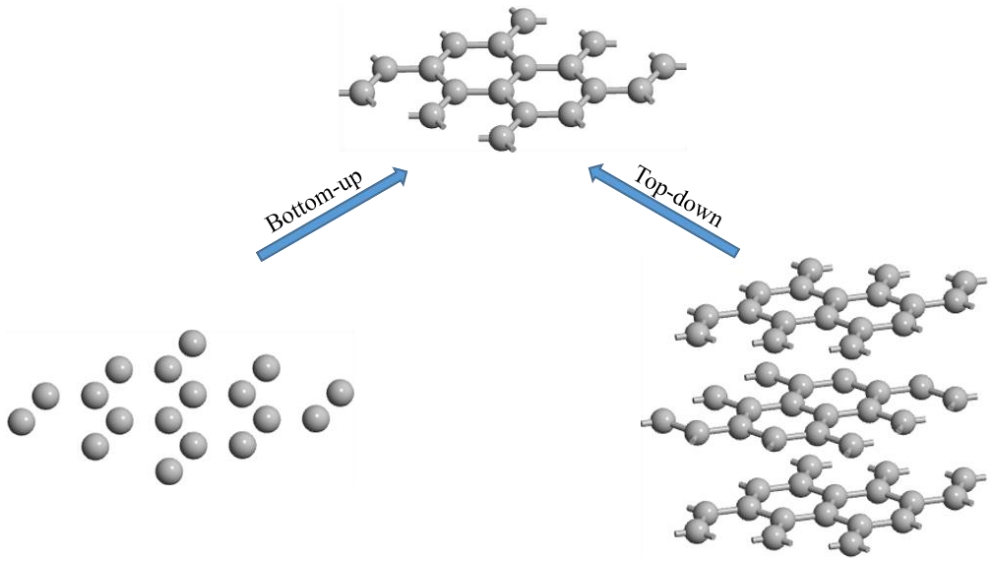

Figure 1.2 A schematic diagram of the "top-down" and "bottom-up" graphene production techniques. The grey balls represent carbon atoms.

Generally speaking, the top-down method correlates with breaking apart large dimensional structures to yield functional devices with required shapes and/or characteristics by using nanofabrication implements. Contrarily, the bottom-up approach attempts to synthesize graphene by using atomic or molecular elements from other available carbon-related sources[43,44]. In detail, the former approach focuses much on dealing with the van der Waals forces between layers. Crucial challenges are the effectual disassembly of layers with the least defects generated on the sheets and the prevention of the afterwards possibly occurred re-agglomeration behaviour. This approach commonly shows demerits include multiplex processing steps, low productivity, etc. The latter approach, on the other hand, usually involves simple processes and can be used to grow large size graphene sheets on certain substrates. One of its main drawbacks is the higher densities of defects than observed in the top-down method. Besides, high temperature is usually required for the superior levels of graphitization and then the production of good quality materials.

Table 1.2 displays a brief statement of some of the most frequently used techniques for single and few layered graphene syntheses. Among them, the exfoliation and reduced graphene oxide (rGO) are the "top-down" methods, while the chemical vapour deposition (CVD) and epitaxial growth belong to the "bottom-up" group. Each method has its own merits and demerits, depending exclusively on the nature and scale of the preferred application.

Table 1.2 Comparison of four synthesis methods of graphene[4,45]

	Graphene quality	Yield	Reproducibility	Cost
Exfoliation	High	Low	Low	Low
rGO	Low	High	High	Low
CVD	High	High	High	High
Epitaxial Growth	High	Low	High	High

Exfoliation can be achieved via either mechanical or chemical routes.

1) Mechanical cleavage is the first generally recognized method used to experimentally synthesize graphene flakes on preferred substrates. In this technique, a longitudinal or transverse force is exerted on the surface of graphitic materials, such as highly oriented pyrolytic graphite (HOPG), single- or poly-crystalline graphite, or amorphous graphite[2,46]. Graphite is a planar structure with individual layers stacked together via week van der Waals forces. The distance between layers is 0.335nm and the interlayer binding energy is around 2eV/nm^2. With the assumption of ~1 friction coefficient between graphite and the substrate, an approximate 300nN/um^2 normal force is supposed to apply for cleaving off one graphene layer from graphite[46,47]. Through repetitive exfoliation, the consequently generated single-, double- or few-layer graphene flakes are normally distinguished by optical microscopy and Raman spectroscopy over exceptionally prepared SiO_2/Si wafers. The flakes commonly turn out to have remarkable qualities especially high electron/hole mobilities, therefore are typically appropriate for fundamental studies on graphene properties. Still, several further enhancements on the mechanical exfoliation approach are required to achieve large-scale and efficient graphene production.

2) Chemical exfoliation mainly contains two steps: the increase of the interlayer distance via the reduction of the van der Waals forces between layers; the exfoliation of single- to few-layer graphene based on ultrasonic treatment or rapid heating technique[46,48]. In this method, graphene or chemical modified graphene (CMG) are produced via various types of colloidal suspensions generated from graphite or its derivatives such as graphite oxide (GO) and graphite intercalated compounds (GICs). This approach is famous for its scalability, possibility in mass production, and adaptability to miscellaneous chemical functionalization. These virtues result in a wide application of this method in energy-storage materials, polymer composites, transparent conductive devices, and so forth[46,49]. The most serious shortcoming, however, is the demand of violent chemicals, sometimes hazardous and non-environmentally friendly reagents[50].

Obtaining graphene flakes from the reduced graphene oxide (rGO) is a type of chemical synthesis method. It contains several steps: the production of graphite oxide (GrO) by deeply oxidizing natural graphite based commonly on the Hummers method; the generation of graphene oxide (GO) with the exfoliation of GrO typically via water sonication; the creation of graphene through the thermal or chemical reduction of graphene oxide[43,46]. This established method is primarily valued for being able to efficiently develop graphene in significant amounts. Due to the disruption of the sp^2 hybridization among the stacked graphene layers during oxidizing graphite, the interlayer distance doubles from 3.35Å in graphite to around 6.8Å in GrO, which reduces the interlayer interaction and facilitates the following GrO delamination[51]. Yet, this oxidation process also induces high-level defects, and therefore undermines the properties of the final products[43].

Chemical vapour deposition (CVD) is also a chemical process where the formation of graphene is based on the decomposition of certain precursors mostly under a high temperature environment. Precursors for graphene synthesis are carbon containing gases generated by vapouring/heating carbon-related liquid/gas sources. In this method, the graphene growth mainly happens on transition metal substrates with practices especially on copper and nickel. Various types of CVD procedures have been developed

so far, among which the thermal CVD and plasma-enhanced CVD (PECVD) are most renowned[43,46].

1) In the thermal CVD process, chemical reactions occur when the substrate is heated up (usually 600°C~800°C) and exposed to gaseous precursors, which results in the deposition on the substrate surface. The chemical mechanism relies on either surface catalysis or segregation. For the former case, the graphene formation takes place only when the precursors contact the substrate metal surface. Once the surface is covered by a graphene layer and the path between precursors and the surface is blocked, no further decomposition will happen, therefore the graphene growth is considered as self-limiting to monolayer. One example under this mechanism is the graphene growth on copper. For the latter case, the graphene formation makes use of the carbon solubility in metals under different temperatures. Carbon atoms from precursors first dissolve in the bulk metal during heating and then diffuse to the surface. In the cooling process, the carbon solubility reduces as the temperature goes down, bringing about the carbon segregation from the surface and the growth of graphene layers. Graphene growth on nickel is agreed to proceed by means of this mechanism. Compared to the surface-catalysed reaction, the number of graphene layers generated via segregation can hardly be limited to only one because it is affected by multiple elements such as the cooling rate and the dissolved carbon amount. However, no ultrahigh vacuum (UHV) environment is required in the segregation mechanism.
2) In the PECVD process, chemical reactions are contingent not on the high temperature but on the plasma of gaseous precursors. Commonly, the creation of plasma is caused by discharging reacting gases between two electrodes with direct current or radio frequency. The introduction of plasma accelerates the chemical reaction, making the following deposition possible occur at a comparatively low temperature. This property is highly important for the application of this method in the area of large-scale industrial manufacture. The low-temperature condition also contributes to the deposition of organic coatings, for instance plasma polymers, which are commonly used in functionalizing nanoparticle surfaces. Yet, the cost of PECVD is not low.

Last but not least, epitaxial growth of graphene, as one of the most admired approaches, was first applied on silicon carbide (SiC) substrates. Generally, epitaxy can be categorized into homoepitaxy and heteroepitaxy. In the former process, the deposited epitaxial film possesses the identical composition with the substrate. This process aims at the production of purer films or layers under dissimilar doping degrees. In the latter process, different materials are performed for the epitaxial layer compared to the substrate. This technology mainly focuses on the growth of integrated crystalline layers for which crystals can hardly or impossibly be acquired. This is the case for the graphene epitaxial growth. During the experiment, the carbide resolves under a high-temperature and UHV condition, followed by the recombination of the carbon components and the evaporation of the non-carbon ones[52]. The quality of produced graphene is affected by multiple parameters, such as pressure, temperature, and forming gas composition[45]. In addition, the development of epitaxial growth technique makes other carbides and 2D materials been utilized in the synthesis. Examples include graphene on titanium carbide (TiC)[53], hexagonal boron nitride (h-BN)[54] and ultrananocrystalline diamond (UNCD)[55]. Epitaxy holds advantages in a strong control over the film composition, the corresponding lattice arrangement and the interfacial energy of hybrid nanostructures[56]. However, the complex and expensive process restricts the commercial mass production of graphene[45,46].

In summary, tremendous efforts have been put on the both the theoretical and experimental study of graphene-related structures. Considering the unique properties of graphene and its derivatives (such as GQD), it is quite appealing, even though challenging, to build completely two-dimensional electronic devices. The quest for ultimate planar devices triggers the motivation behind the research work presented in this thesis.

1.2. Motivation

There are many reasons that will hinder the further development of conventional electronic devices. Two long-standing concerns are: the miniaturization limit and the ability to use conventional electronic components in all applications.

Miniaturization is one of the key impetuses in the progress of electronic devices. The reduction in the size of individual components generally leads to more compactly built Integrated Circuit (IC) systems with more economical production costs. In the past few decades, the focus has centred on shortening the length (x-direction) and width (y-direction) of devices, while minimal effort was expended on reducing the thickness (z-direction). However, with the ground-breaking isolation of graphene, devices with truly atomically-thin planar structures became possible. It is significant to acknowledge that the two-dimensionality contributes to many compelling electronic properties, which is not only restricted to graphene but also applied to other novel nanoscale two-dimensional materials, making them promising candidates for next-generation high-performance electronic devices. For instance, in the area of FETs, compared to their 3D counterparts, the size reduction in 2D materials brings about the suppression of the short-channel effects and the enhancement in the mobility. The first reported 2D FET in 2011, the monolayer MoS_2 FET, presented a carrier mobility of ~184$cm^2/V{\cdot}s$. Graphene-based FETs produced afterwards can even reach a carrier mobility of more than 8,000 $cm^2/V{\cdot}s$ at room temperature[62,63]. However, although remarkable properties promote the popularity of graphene in all kinds of fields, there are still some areas that have not yet been completely studied, leaving plenty of rooms for deeper research. One example is energy filtering, driven by the increasing demand of lowering energy consumption.

Devices that are able to act as energy filters are essential in realizing high-performance energy-efficient nanoelectronic systems. Although quantum-dot refrigeration is already available, due to the material applied, most quantum dot refrigerators do not hold obvious advantages in miniaturization, flexibility, compatibility, or many other aspects. Therefore, it is quite appealing that high-performance energy filters can be achieved together with more intrinsic features, such as good tunability and miniaturization capability, by utilizing novel materials. This idea triggers the endeavour taken in this thesis in exploring the possible application of graphene and especially its derivatives (GQD) to realize nanoscale 2D energy filters.

The potential of GQD devices covers not only the field of energy filtering, but also many other areas with significant influence, including digital electronics. One of the properties that contributes to this fact is the NDR effect caused by the electron resonant

tunnelling, which enables the role of GQD devices as multi-state memories. In this application, information storage and its conversion among multiple logic states, rather than merely two states (known as the “ON” and “OFF” states), can be accomplished with one single device involved. This achievement can be considered as one that may cause revolution in electronics. However, due to the low peak-to-valley current ratio, many traditional NDR devices are not suitable in the memory application. Therefore, this thesis also probes the application of GQD to realize high-performance multi-state memory devices.

In summary, this thesis mainly focuses on investigating the potential of GQD in both the analogue electronics, such as energy filters, and the digital electronics, such as memristors. The general outline of this thesis is as follows:

In ***Chapter One***, background and motivation behind the study are elaborated. Emphases are greatly paid on detailed presentation of four dominant electronic band gap theories and four major categories in material synthesis. This chapter offers the scope of the thesis and indicates three principal aspects discussed in the following chapters, which are the theoretical analysis, the model simulation, and the experiment design.

In ***Chapter Two***, literature reviews the topics of material based energy filters and memory devices as well as fabrication techniques. The current state of the art within each field is identified and described. This chapter highlights completed and generally accepted research, and points out current state of thinking. More importantly, research gaps are identified with potential ways to address the gaps articulated.

In ***Chapter Three***, GQD-based structures are investigated with the goal of generating energy filters for next generation lower-power lower-noise two-dimensional electronic systems. With the GQD as the basic building block, fundamental two-terminal energy filters are constructed. Electron transport properties of the proposed devices are evaluated in order to demonstrate electron energy filtering and the device tunability. Theoretical analyses indicate that the attempt of applying GQDs in the energy filters is valuable and provides a novel idea for the production of low-power and low-noise electronics.

In ***Chapter Four***, the GQD structure discussed in chapter three is modified and applied into the field of memory devices, realizing the first all GQD-based memristor. It is revealed that the resistive switching is driven by the resonant electron tunneling. Electronic properties of devices are examined and turn out to be unique, which yields interesting findings on an encouraging category of resistive memory devices.

Chapter Five investigates the fabrication process for the two-dimensional GQD structure utilised in the previous two chapters. This process contains several steps and relies largely on the e-beam lithography (EBL) and the rapid thermal annealing (RTA) required for the epitaxial growth of the graphene layer. Experimental results for partial steps are interpreted. The fabrication of the GQD is in its infancy and this chapter describes some of the first steps in achieving this goal.

Finally, ***Chapter Six*** summarizes all studies presented in the thesis. Main arguments are restated, important evidences are reiterated, and a number of recommendations for future work are put forward.

1.3. Main Contributions

This section summarizes the key novelty and contributions of the research work presented in this thesis.

Chapter Three:

- Proposed a new concept of noise and energy filters by making use of the quantum tunnelling effect rather than relying on the cryogenic techniques.
- Investigated the effect of the quantum dot geometry on NDR characteristics, showing that with the appropriate dimensioning of quantum dot structures can cause large differences on the observed tunnelling.
- Investigated how the position and magnitude of the energy passband are controlled by the device dimensioning, confirming the tunability of the NDR and energy filtering effect.

Chapter Four:

- Proposed the application of two-dimensional GQDs for resistive memory systems and investigated an all-GQD based memristor.
- Studied the effect of device geometry on the memory characteristics, including position, number and noise margin of logic states, indicating the adaptability of the system.
- Presented the function of an isolated gate terminal in enhancing the flexibility of the upgraded memory system, showing an increase of logic states with the system simplicity being maintained.

Chapter Five:

- Proposed and studied the selective growth of graphene utilizing a carbon segregation strategy, indicating the potential of high-quality GQD structures in the wafer scale.
- Investigated the crystal orientation of the deposited Ni layer and the Raman spectrum of the generated graphene layers, showing the viability of RTA in realizing uniform graphene production.
- Investigated the sample condition after the EBL process using helium ion microscopy (HIM) to put forward possible solutions to overcome current fabrication barriers and offered suggestions to other researchers who are interested in implementing similar experiments in the future.

1.4. Publications

This section lists publications resulting from this thesis. They are listed below:

Journal Papers

[1] Chapter Three: X. Pan, W. Qiu, and E. Skafidas, "Energy-filtered Electron Transport Structures for Low-power Low-noise 2-D Electronics", *Sci. Rep.*, vol. 6, Oct. 2016.

[2] Chapter Four: X. Pan and E. Skafidas, "Resonant tunneling based graphene quantum dot memristors", *Nanoscale*, vol. 8, no. 48, pp. 20074–20079, Dec. 2016.

Conference Paper

[1] Chapter Three: X. Pan and E. Skafidas, “Structure-property relationships for graphene quantum dot based electronic devices”, in *International Conference on Nanoscience and Nanotechnology (ICONN)*, 2018, pp. 541.

References

1. Li, X., Rui, M., Song, J., Shen, Z. & Zeng, H. Carbon and Graphene Quantum Dots for Optoelectronic and Energy Devices: A Review. *Adv. Funct. Mater.* **25,** 4929–4947 (2015).
2. Cooper, D. R. *et al.* Experimental Review of Graphene. *ISRN Condens. Matter Phys.* **2012,** 1–56 (2012).
3. Bak, S., Kim, D. & Lee, H. Graphene quantum dots and their possible energy applications: A review. *Curr. Appl. Phys.* **16,** 1192–1201 (2016).
4. Ozhukil Valappil, M., K. Pillai, V. & Alwarappan, S. Spotlighting graphene quantum dots and beyond: Synthesis, properties and sensing applications. *Appl. Mater. Today* **9,** 350–371 (2017).
5. Geim, A. K. & Novoselov, K. S. The rise of graphene. *Nat. Mater.* **6,** 183–191 (2007).
6. Lalwani, G. *et al.* Two-Dimensional Nanostructure-Reinforced Biodegradable Polymeric Nanocomposites for Bone Tissue Engineering. *Biomacromolecules* **14,** 900–909 (2013).
7. Petruk, O. *et al.* Sensitivity and Offset Voltage Testing in the Hall-Effect Sensors Made of Graphene. in *Recent Advances in Automation, Robotics and Measuring Techniques* 631–640 (Springer, Cham, 2014). doi:10.1007/978-3-319-05353-0_60
8. Singh, C., S, N., Jana, A., Kumar Mishra, A. & Paul, A. Proton conduction through oxygen functionalized few-layer graphene. *Chem. Commun.* **52,** 12661–12664 (2016).
9. Stoller, M. D., Park, S., Zhu, Y., An, J. & Ruoff, R. S. Graphene-Based Ultracapacitors. *Nano Lett.* **8,** 3498–3502 (2008).
10. Abergel, D. S. L., Apalkov, V., Berashevich, J., Ziegler, K. & Chakraborty, T. Properties of graphene: a theoretical perspective. *Adv. Phys.* **59,** 261–482 (2010).

11. Li, X. *et al.* Graphene and related two-dimensional materials: Structure-property relationships for electronics and optoelectronics. *Appl. Phys. Rev.* **4,** 021306 (2017).
12. Shen, J., Zhu, Y., Yang, X. & Li, C. Graphene quantum dots: emergent nanolights for bioimaging, sensors, catalysis and photovoltaic devices. *Chem. Commun.* **48,** 3686–3699 (2012).
13. Kamat, P. V. Quantum Dot Solar Cells. Semiconductor Nanocrystals as Light Harvesters. *J. Phys. Chem. C* **112,** 18737–18753 (2008).
14. Guo, C. X. *et al.* Layered Graphene/Quantum Dots for Photovoltaic Devices. *Angew. Chem. Int. Ed.* **49,** 3014–3017 (2010).
15. Chao, D. *et al.* Graphene Quantum Dots Coated VO2 Arrays for Highly Durable Electrodes for Li and Na Ion Batteries. *Nano Lett.* **15,** 565–573 (2015).
16. Son, D. I. *et al.* Emissive ZnO–graphene quantum dots for white-light-emitting diodes. *Nat. Nanotechnol.* **7,** 465–471 (2012).
17. Dong, Y. *et al.* Graphene Quantum Dot as a Green and Facile Sensor for Free Chlorine in Drinking Water. *Anal. Chem.* **84,** 8378–8382 (2012).
18. Wu, Z. L., Liu, Z. X. & Yuan, Y. H. Carbon dots: materials, synthesis, properties and approaches to long-wavelength and multicolor emission. *J. Mater. Chem. B* **5,** 3794–3809 (2017).
19. Choi, S.-H. Unique properties of graphene quantum dots and their applications in photonic/electronic devices. *J. Phys. Appl. Phys.* **50,** 103002 (2017).
20. Zhou, S., Xu, H., Gan, W. & Yuan, Q. Graphene quantum dots: recent progress in preparation and fluorescence sensing applications. *RSC Adv.* **6,** 110775–110788 (2016).
21. Zhang, Z. Z., Chang, K. & Peeters, F. M. Tuning of energy levels and optical properties of graphene quantum dots. *Phys. Rev. B* **77,** 235411 (2008).
22. Bacon, M., Bradley, S. J. & Nann, T. Graphene Quantum Dots. *Part. Part. Syst. Charact.* **31,** 415–428 (2014).
23. Xu, B. & Dubi, Y. Negative differential conductance in molecular junctions: an overview of experiment and theory. *J. Phys. Condens. Matter* **27,** 263202 (2015).
24. *Negative Differential Resistance and Instabilities in 2-D Semiconductors*. **307,** (Springer US, 1993).
25. Martin, R. M. *Electronic Structure: Basic Theory and Practical Methods*. (Cambridge University Press, 2004).

26. Kittel, C. *Introduction to solid state physics*. (Wiley, 1971).
27. Altmann, S. L. *Band theory of metals: the elements*. (Pergamon Press, 1970).
28. C, M. D. *Many-body Problem, The: An Encyclopedia Of Exactly Solved Models In One Dimension (3rd Printing With Revisions And Corrections)*. (World Scientific, 1993).
29. Harrison, W. A. *Electronic structure and the properties of solids: the physics of the chemical bond*. (Dover Publications, 1989).
30. Jones, R. O. Density functional theory: Its origins, rise to prominence, and future. *Rev. Mod. Phys.* **87,** 897–923 (2015).
31. Fiolhais, C., Nogueira, F. & Marques, M. A. L. *A Primer in Density Functional Theory*. (Springer Science & Business Media, 2003).
32. Jain, A., Shin, Y. & Persson, K. A. Computational predictions of energy materials using density functional theory. *Nat. Rev. Mater.* **1,** 15004 (2016).
33. Berland, K. *et al.* van der Waals forces in density functional theory: a review of the vdW-DF method. *Rep. Prog. Phys.* **78,** 066501 (2015).
34. Martins, A. de S. & Veríssimo-Alves, M. Group-IV nanosheets with vacancies: a tight-binding extended Hückel study. *J. Phys. Condens. Matter* **26,** 365501 (2014).
35. Raza, H. & Kan, E. C. An extended Hückel theory based atomistic model for graphene nanoelectronics. *J. Comput. Electron.* **7,** 372–375 (2008).
36. Kienle, D., Cerda, J. I. & Ghosh, A. W. Extended Hückel theory for band structure, chemistry, and transport. I. Carbon nanotubes. *J. Appl. Phys.* **100,** 043714 (2006).
37. Ribeiro, I. A., Ribeiro, F. J. & Martins, A. S. An extended Hückel study of the electronic properties of III–V compounds and their alloys. *Solid State Commun.* **186,** 50–55 (2014).
38. Lee, M., Leiter, K., Eisner, C., Crone, J. & Knap, J. Extended Hückel and Slater's rule initial guess for real space grid-based density functional theory. *Comput. Theor. Chem.* **1062,** 24–29 (2015).
39. Hoffmann, R. & Lipscomb, W. N. Boron Hydrides: LCAO—MO and Resonance Studies. *J. Chem. Phys.* **37,** 2872–2883 (1962).
40. Webster, C. E. & Hall, M. B. Chapter 40 - Forty years of Fenske-Hall molecular orbital theory. in *Theory and Applications of Computational Chemistry* (eds. Dykstra, C. E., Frenking, G., Kim, K. S. & Scuseria, G. E.) 1143–1165 (Elsevier, 2005). doi:10.1016/B978-044451719-7/50083-4

41. Novoselov, K. S. *et al.* Two-dimensional gas of massless Dirac fermions in graphene. *Nature* **438,** 197–200 (2005).

42. Kusmartsev, F. V., Wu, W. M., Pierpoint, M. P. & Yung, K. C. Application of Graphene Within Optoelectronic Devices and Transistors. in *Applied Spectroscopy and the Science of Nanomaterials* 191–221 (Springer, Singapore, 2015). doi:10.1007/978-981-287-242-5_9

43. S. Edwards, R. & S. Coleman, K. Graphene synthesis: relationship to applications. *Nanoscale* **5,** 38–51 (2013).

44. Biswas, A. *et al.* Advances in top–down and bottom–up surface nanofabrication: Techniques, applications & future prospects. *Adv. Colloid Interface Sci.* **170,** 2–27 (2012).

45. Tan, H., Wang, D. & Guo, Y. Thermal Growth of Graphene: A Review. *Coatings* **8,** 40 (2018).

46. Bhuyan, M. S. A., Uddin, M. N., Islam, M. M., Bipasha, F. A. & Hossain, S. S. Synthesis of graphene. *Int. Nano Lett.* **6,** 65–83 (2016).

47. Zhang, Y., Small, J. P., Pontius, W. V. & Kim, P. Fabrication and electric-field-dependent transport measurements of mesoscopic graphite devices. *Appl. Phys. Lett.* **86,** 073104 (2005).

48. Xia, Z. Y. *et al.* The Exfoliation of Graphene in Liquids by Electrochemical, Chemical, and Sonication-Assisted Techniques: A Nanoscale Study. *Adv. Funct. Mater.* **23,** 4684–4693 (2013).

49. Park, S. & Ruoff, R. S. Chemical methods for the production of graphenes. *Nat. Nanotechnol.* **4,** 217–224 (2009).

50. Rao, K. S., Senthilnathan, J., Liu, Y.-F. & Yoshimura, M. Role of Peroxide Ions in Formation of Graphene Nanosheets by Electrochemical Exfoliation of Graphite. *Sci. Rep.* **4,** 4237 (2014).

51. Compton Owen C. & Nguyen SonBinh T. Graphene Oxide, Highly Reduced Graphene Oxide, and Graphene: Versatile Building Blocks for Carbon-Based Materials. *Small* **6,** 711–723 (2010).

52. de Heer, W. A. *et al.* Epitaxial graphene. *Solid State Commun.* **143,** 92–100 (2007).

53. Terai, M., Hasegawa, N., Okusawa, M., Otani, S. & Oshima, C. Electronic states of monolayer micrographite on TiC(111)-faceted and TiC(410) surfaces. *Appl. Surf. Sci.* **130–132,** 876–882 (1998).

54. Yang, W. *et al.* Epitaxial growth of single-domain graphene on hexagonal boron nitride. *Nat. Mater.* **12,** 792–797 (2013).

55. Berman, D. *et al.* Metal-induced rapid transformation of diamond into single and multilayer graphene on wafer scale. *Nat. Commun.* **7,** 12099 (2016).

56. Tan, C., Chen, J., Wu, X.-J. & Zhang, H. Epitaxial growth of hybrid nanostructures. Nat. Rev. Mater. 3, 17089 (2018)

57. Pan, D., Zhang, J., Li, Z. & Wu, M. Hydrothermal Route for Cutting Graphene Sheets into Blue-Luminescent Graphene Quantum Dots. Adv. Mater. 22, 734–738 (2010).

58. Li, Y. et al. An Electrochemical Avenue to Green-Luminescent Graphene Quantum Dots as Potential Electron-Acceptors for Photovoltaics. Adv. Mater. 23, 776–780 (2011).

59. Lee, J. et al. Uniform Graphene Quantum Dots Patterned from Self-Assembled Silica Nanodots. Nano Lett. 12, 6078–6083 (2012).

60. Moon, J. et al. One-Step Synthesis of N-doped Graphene Quantum Sheets from Monolayer Graphene by Nitrogen Plasma. Adv. Mater. 26, 3501–3505 (2014).

61. Zhu, H. et al. One-step synthesis of graphene quantum dots from defective CVD graphene and their application in IGZO UV thin film phototransistor. Carbon 100, 201–207 (2016).

62. Stoller, M. D., Park, S., Zhu, Y., An, J. & Ruoff, R. S. Graphene-Based Ultracapacitors. *Nano Lett.* 8, 3498–3502 (2008).

63. Kim, S. *et al.* Realization of a high mobility dual-gated graphene field-effect transistor with Al2O3 dielectric. *Appl. Phys. Lett.* **94**, 062107 (2009).

2. LITERATURE REVIEW

In this chapter, the graphene literature is reviewed and analysed. The reviews focus on examining the evolution of particular research throughout a period of time and categorized into three sections: energy filters, memristors, and fabrication techniques. In each section, both relationships and areas for future research between each work to the others are described.

2.1. Electron Energy Filters

Energy waste or dissipation is considered as one of the major challenges in integrated electronics. It restricts the performance of electrons in a wide range of applications, e.g. from portable devices to mass data storage systems, all essentially depending on silicon micro/nanotechnology[1]. One of the fundamental cause underlying these excessive dissipation cases is noise resulting from the intrinsic electron thermal excitation, which degrades the performance of electronic devices[2]. In spite of the fact that intense progress has been achieved over the past few decades, current mainstream devices such as silicon transistors are still under one thousandth less energy-efficient than the limit set in theoretical physics. It has been estimated that the limit approximates $3k_BT$, which is around 10^{-20}J, for a binary switch when considered under the room temperature, where k_B and T are the Boltzmann constant and the absolute temperature respectively[3]. Therefore, an approach aiming at the electron thermal excitation control is an important area of research.

Considering the development on modern micro/nanoscale materials and devices, improvement on energy efficiency is promising. Studies by other researchers have revealed the possibility in inhibiting the electron thermal excitation by making effective use of the tunneling effect observed in particularly designed structures. Classically, the energy dissipation for electronic devices is predicted in the most rudimentary way as the product of the current through and the voltage drop on it. However, when taking account of the tunneling transport encountered in mesoscopic systems, the traditional interpretation becomes too simple for analysing such dissipation. In fact, it has been investigated via more sophisticated approaches, such as the Monte Carlo simulation[4–6]. The crucial identity of dissipation near the energy barrier is that the barrier acts as a filter of the carrier distribution function. As schematically illustrated in Fig. 2.1, carriers with higher energy hold higher possibilities in tunneling across the barrier, resulting in temperature-based carrier distributions of carriers on the two sides of the barrier.

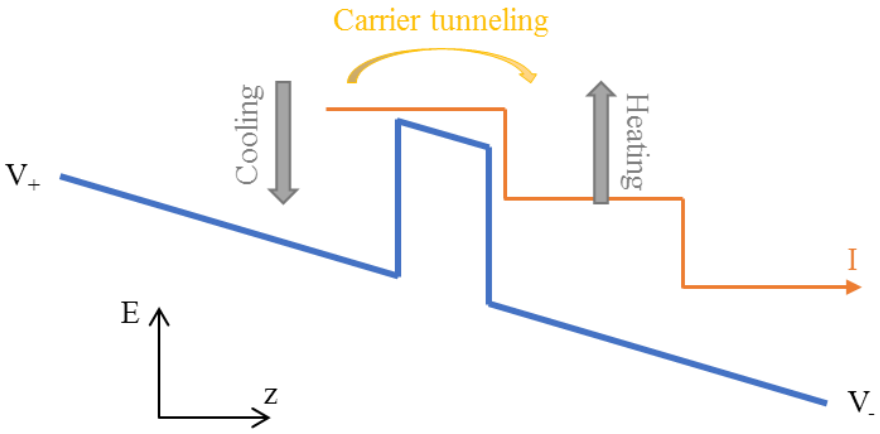

Figure 2.1 A schematic illustration of the energy dissipation near an energy barrier. The barrier plays an role as a filter, leading to the positive/negative energy dissipation of carriers on the right/left sides of the barrier[1].

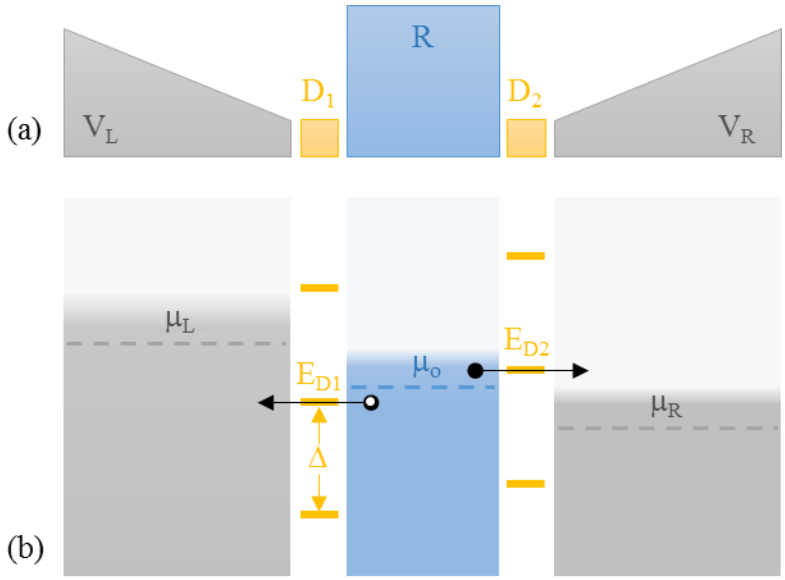

Figure 2.2 The (a) schematic illustration and (b) energy-level diagram of the quantum-dot refrigerator structure. The resonant tunneling from the reservoir R to the two electrodes sharpens the Fermi-Dirac distribution of the reservoir, and consequently cools it down[7].

In other words, the left-sided carriers are practically cooled down, whilst the right-sided ones are correspondingly heated up. This phenomenon relies on the barrier structural features (such as shape and height), and the external factors (such as the current direction).

The utilization of the tunneling effect for the purpose of reducing energy dissipation can be traced back to the work of Edwards *et al*. in 1993, where a quantum-dot refrigerator was theoretically designed. Fig. 2.2 shows the schematic illustration and

energy-level diagram of the device. Quantum dots D_1 and D_2 make the reservoir (R) coupled to the left (V_L) and right (V_R) electrode respectively. Energy levels of both quantum dots are divided by Δ; R, V_L and V_R are sufficiently close to quantum dots for resonant tunneling, The chemical potentials μ_L and μ_R in V_L and V_R are tuned by externally applied DC voltages to have their difference less than Δ, whilst the chemical potential μ_o in R is adjusted between μ_L and μ_R. Since an electron is almost impossible to realize resonant tunneling unless its energy matches with one of the energy states in the barrier, in this quantum-dot model, the resonant tunnelling to V_R aims at the depletion of electron states above μ_o in R, and holes below μ_o in R resonant tunnel to V_L likewise. Consequently, the Fermi-Dirac distribution in R is sharpened, which then leads to electron refrigeration. This quantum-dot refrigerator is predicted to be capable of effectively cooling electrons of a mesoscopic two-dimensional electron gas (2DEG) reservoir at micro-kelvins, and of a macroscopic reservoir under even lower temperatures[7,8].

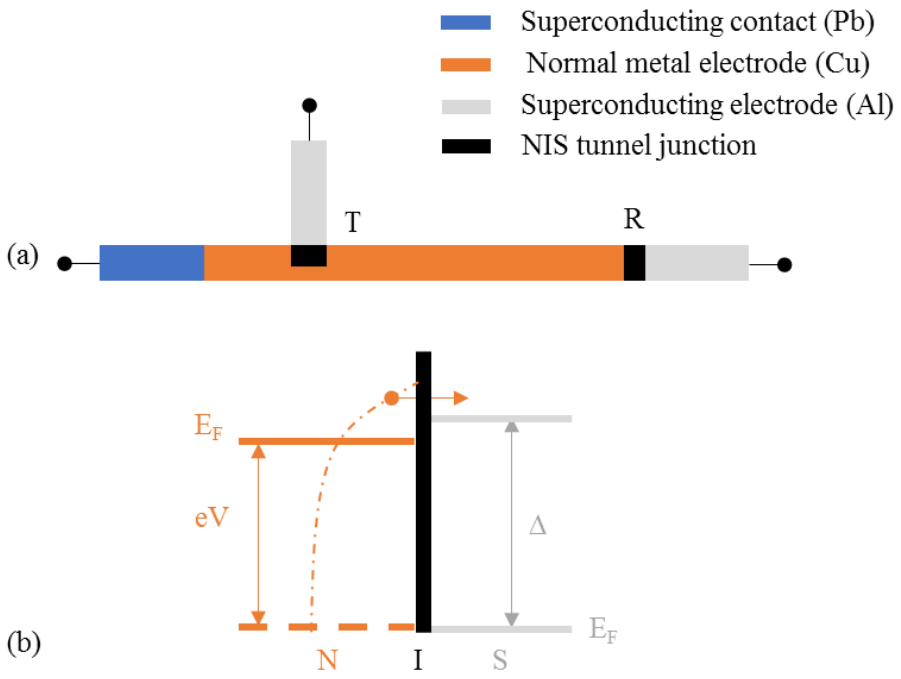

Figure 2.3 (a) The schematic illustration of the electronic micro-refrigerator. Two NIS tunnel junctions are labelled as T and R. (b) The energy-level diagram of the refrigerator junction. Δ is the energy gap of the superconducting electrode, E_F is the Fermi energy level[9].

Due to the difficulty of nanofabrication in the early 1930s, the concept of the quantum-dot refrigerator was not put into practice immediately. Instead, an electronic micro-

refrigerator was reported by Nahum *et al*. in 1994 with the base on a normal-insulator-superconductor (NIS) tunnel junction. Fig. 2.3 illustrates the schematic of the device and the energy-level diagram of the refrigerator junction.

A normal metal electrode is connected to a superconducting contact and other two superconducting electrodes to generate two NIS tunnel junctions, which act as both a refrigerator and a sensitive thermometer for the electrons. By electrically biasing the refrigerator junction around the gap Δ, electrons whose energies are higher than Fermi energy E_F tunnel out of the normal metal electrode. Therefore, high-energy thermal excitations are taken away from the electrons, resulting in the cooling effect. It is also pointed out that the current-voltage characteristic of the junction is only controlled by the electron temperature in the normal metal electrode and is irrelevant to that in the superconducting part. The current (I) expression is demonstrated in the following form[9]:

$$I = \frac{1}{eR_N}\int_{\Delta}^{\infty} \frac{E}{\sqrt{E^2-\Delta^2}\left[\exp\left(\frac{E-eV}{k_BT}\right)+1\right]}dE \qquad (2.1)$$

where T is the temperature of electrons in the normal metal electrode, R_N is the junction resistance under the normal state. Apparently, the current decreases as the temperature drops, which leads to the reduction of the energy dissipation.

It is noteworthy that two years later in 1996, based on the abovementioned NIS structure, Leivo *et al*. symmetrized the system by pairing two NIS junctions in series, which was later known as the SINIS configuration[10]. Advantages of this structure, compared to the asymmetric single-junction one, include easier fabrication process and more efficient electron cooling capability. Subsequently, further experimental arguments of electron cooling effect within SINIS configurations were demonstrated. Examples are the design of an on-chip electron refrigerator composed of arrays of submicron tunnel junctions by Leoni *et al*.[11] in 1998, the development of a sub-kelvin refrigeration method based on quasiparticle tunneling in a $Cu/AlO_x/Al/AlO_x/Cu$ structure on a bulk Si substrate by Pekola *et al*.[12] in 2000, the discussion on an electron-tunneling thin-film refrigerator with Al-Mn\Al-Mn oxide\Al as the metal\insulator\superconductor material respectively by Clark *et al*.[13] in 2004, the proposal of a three-terminal Coulomb-blockaded device in the form of a SINIS single-electron refrigerator by Pekola *et al*.[14] in 2007, and so forth. Fig. 2.4 gives an illustration of the schematic of a typical $Cu/Al_2O_3/Al/Al_2O_3/Cu$ SINIS micro-refrigerator and the energy-level diagram of the

structure to demonstrate its operational principle. As is shown in the figure, the electric current flows into the normal metallic area via the junction on one side and out via the other side, whereas the heat flows out of the normal metal via both tunnel junctions.

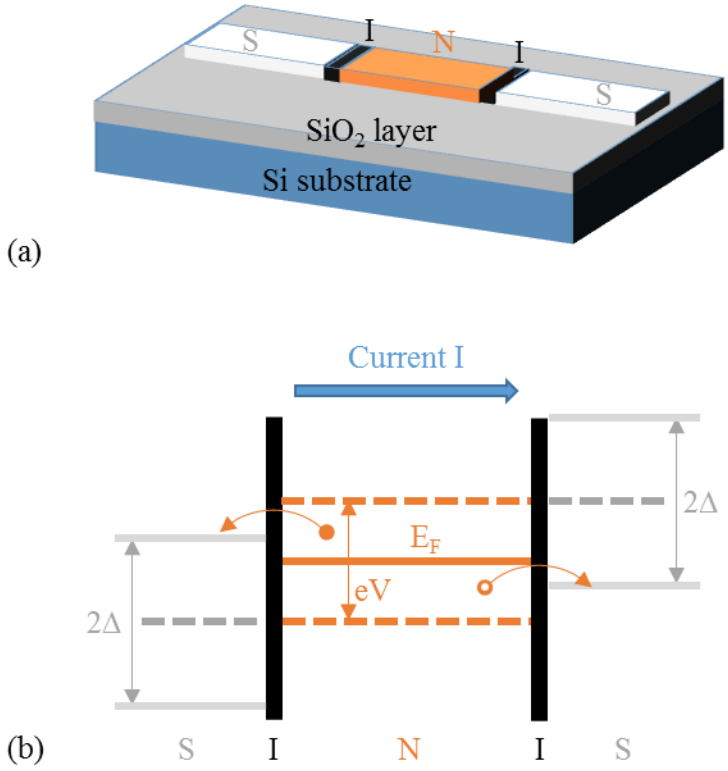

Figure 2.4 (a) The schematic picture of a commonly-used metallic SINIS micro-refrigerator. Two NIS junctions are connected in series on bulk Si/SiO₂ substrate[12]. (b) The energy-level diagram of a voltage-based refrigerator junction illustrating cooling in the system. With a proper applied bias voltage, hot electrons above the Fermi level tunnel away, while cold electrons below the Fermi level tunnel into the normal metallic region[15].

It is not until 2009 when Prance *et al*[16]. tested and demonstrated the system that Edwards *et al*. initially suggested. A 6μm^2 central area of an isolated two-dimensional electron gas (2DEG) was cooled down through utilizing the energy-dependent tunneling between two quantum dots. Structure details of the whole device are: a GaAs/AlGaAs heterostructure was used as the substrate, on which NiCr/Au gates were patterned via e-beam lithography. The 2DEG, whose density is approximately 1.37×10^{11}cm^{-2}, was located 90nm-beneath the surface of the substrate and contacted by AuGeNi electrodes. Three quantum dots were put on the left/right/top of the 2DEG region, although the right dot was not used in the experiment. Clear electrostatic effect was observed during the measurement, followed by the development of a model used

to explain it. The model explains experimental data reasonably when ambient electron temperatures are over 120mK; while at temperatures below it, results are not consistent with predictions because of the small electron-electron scattering rate. Possible improvements were proposed on three aspects: increasing controllable quantum dots to optimize the device for lowest base temperatures, expanding the central region for denser states per unit energy, and amplifying the capacitance of the central region to obscure electrostatic effects, which in the long run enables the generation of a universal platform for extra-low temperature measurements.

Two years later in 2011, a similar but upgraded 2DEG reservoir was demonstrated by Gasparinetti *et al*[17]. In this work, based on the detailed examination on the CB (Coulomb blockade) peaks under certain temperature biases, a method was proposed for the detection of the local temperature in a 2DEG region, as well as for the application in exploring the energy-relaxation mechanism in a microscale electronic domain. Fig. 2.5 displays the scanning electron micrograph of the device and schematically shows the measurement setup.

Al Schottky gates, defining a $16\mu m^2$ central region, were patterned on a GaAs/AlGaAs heterostructures by e-beam lithography. The electron density of the 2DEG is around $2.26\times10^{11}cm^{-2}$. Experiments were conducted under extra-low temperatures in a cryostat filled with ^3He. When a DC current I was driven over the QPC1-domain-QPC2 circuit, the central domain was heated up. At the same time, the differential conductance under a zero bias was probed across the QPC3-domain-QD route. The electron temperature was measured to be dependent on the heating power. With the coupling reduction between the 2DEG domain and the quantum point contacts (QPCs), a crossover regime was observed, in which surplus heat was eliminated due to the high-temperature quasiparticle tunneling through the QPCs.

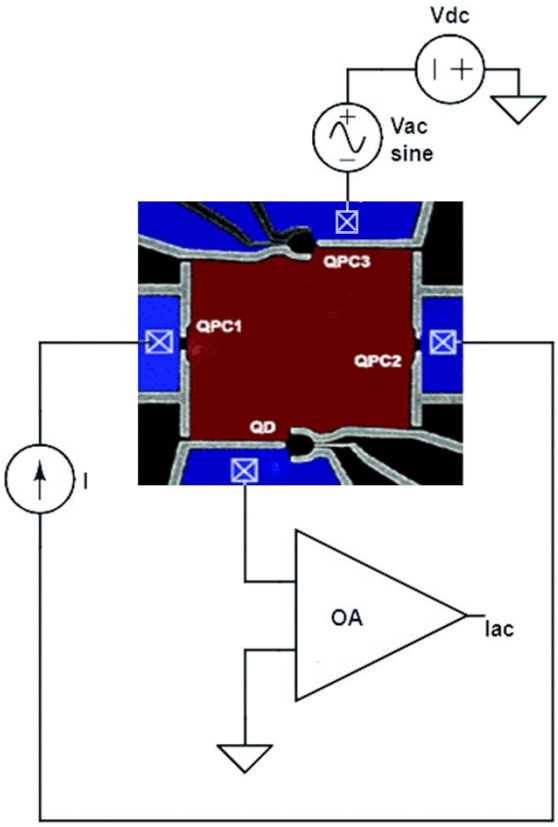

Figure 2.5 The false-colour SEM image of the device and the schematic diagram of the measurement configuration. The 16μm^2 central domain is defined by Al Schottky gates (light grey) and connected to the surrounding 2DEG zones through a bottom QD and three QPCs located in the top and left/right side. Ohmic contacts to the 2DEG are suggested by four crossed squares[17].

Compared to a metal hybrid, the semiconducting quantum dot is more promising in energy-related fields as its potential in bringing about efficient refrigeration based on firmly established experimental techniques. More recently, since the graphene and its derivatives have emerged as novel materials for electronics, their outstanding thermal and electrical performances make them substantially popular in nanoelectronic systems with targets such as energy efficiency. According to studies, devices built with carbon nanomaterials possess several advantages: (a) electron/hole mobilities up to 100 times higher than the traditional silicon, which implies the reduction in scattering as well as energy and power dissipation[1]; (b) superior thermal conductivity attributed to the strong sp^2 bonding, which, under the room temperature, is quantitatively around 13.5-40.5 times higher than Si, 5-15 times higher than Cu, and 2-6 times higher than pure diamond[18,19]; (c) high optical-phonon energies (three times larger than that of silicon), indicating a low probability of electron scattering at the low-field region as well as near

room temperature. Therefore, the realization of all graphene-based energy filters would be appealing for the field, which is one of the major investigations demonstrated in this thesis and is explicitly discussed in ***Chapter Three***.

2.2. Resistor-type Memory Devices

The development of information technology results in an astounding progress in the field of memory electronics during past decades. Conventionally, memory devices are based on semiconductor materials such as silicon. The requirement of large-capacity data storage and fast information access brings about an increasing amount of components been assembled into one single chip, which suggests a decrease in the feature size of semiconductor devices. However, several drawbacks appear as the dimension of silicon-based devices reduces to certain value (usually around 22 nm), which includes less stability, lower read reliability due to serious crosstalk, unexpected power consumption, undesirable heat generation, and so forth. Therefore, to achieve advanced information storage, novel memory technologies are essential[20].

Basically, the primary goal of a memory device is to store and retrieve information via the "0" and "1" encoding. In typical silicon-based memory devices, the data storage is determined by the amount of charge stored in the electronic elements. According to different criteria, memory devices can be categorized in various methods, among which, there are two forms of classification that are widely accepted:

1) Based on the data storage standard, electronic memory devices are generally divided into two main categories: volatile and non-volatile. Volatile memory requires the support of a continuous power supply or a periodical pulse to maintain the information stored in the chip. Any interruption on power results in a complete data loss. Random-access memory (RAM) is the most well-known example in this case. As a common term, it refers to any semiconductor gadget in which data can be frequently read and written. Ultrafast responding performance and structural simplicity are the major advantages that make volatile memory be the most widely-used type of primary data storage in computers. Non-volatile memory, on the other hand, needs no power to retain digital information. It can preserve the data stored in the memory chip even in

the case of power failure. This property makes non-volatile memory typically used for the mission of second storage. Examples include read-only memory (ROM) and flash memory. Compared to volatile memory, non-volatile devices generally have longer write endurance, respond in lower speed, and generate more cost[21,22].

2) Based on the device structure standard, electronic memory devices are usually classified into three principal categories: resistor-type, transistor-type, and capacitor-type. Fig. 2.6 illustrates the configuration and schematic diagram of the three types of memory devices[23,24]. The transistor-type memory commonly comprises the following principal elements: three basic electrodes (source, drain and gate), one dielectric layer made of insulators and one active layer made of semiconductors. Materials for the electrodes can be doped semiconductors, polymer mixtures, alloys or pure metals, according to practical requirements[25]. Source-drain and source-gate are considered as two pairs of the terminals in the memory system. When a voltage is applied across one pair, the current through the other pair is affected correspondingly. Fig. 2.6(a) indicates a source-gate voltage (V_G), a source-drain voltage (V_D) and its relevant current (I_D). Since in semiconductors, doped or undoped, the free electron concentration is low, when V_G equals to zero, the channel current I_D has a small value, which represents an OFF state of the transistor device. As the value of V_G grows, an accumulation of charge carriers occurs at the semiconductor/dielectric interface, resulting in an increase on the carrier concentration in the semiconductor layer. Consequently, I_D begins to grow significantly and turns the device to the ON state. Compared to the transistor-type device, capacitor-type memory has a simpler structure. Under certain applied electric field, chargers are kept within the two parallel electrodes. The charge amount determines the encoded bit level ("0" or "1"), and the medium between electrodes determines the storage property of the memory (volatile or non-volatile). Memory devices based on a dielectric-medium capacitor are volatile as the information cannot be retained without periodical refreshment; while if the medium has a ferroelectric property, devices are non-volatile as ferroelectric materials are intrinsically capable of maintaining permanent electric polarization and repeatedly shifting among stable states. Last but not least, devices with resistive switching materials embodied are regularly defined as resistor-type memory or memristors[26]. This

type of memory is different from the two above-mentioned types in not only the structure but also the operation mechanism. Resistor-type memory does not requests particular cell structures and usually has a straightforward configuration with the medium layer sandwiched between two electrodes on a substrate, as shown in Fig. 2.6(c). Besides, no structural equilibrium is required for the top and bottom electrodes, which means they can be either symmetric or asymmetric in the layout. In the respect of data storage, resistor-type memory has an entirely distinct and more diverse feature. The electric conductivity characteristic of the medium material is the key factor that decides the states of devices in the circumstance of an applied electric field. The electric conductance switching causes electrical bi-stability and can be interpreted by a variety of mechanisms, in which charge transfer effect[27], reduction-oxidation (redox) reaction[28], filament conduction[29], and charge trapping[30] are extensively reported.

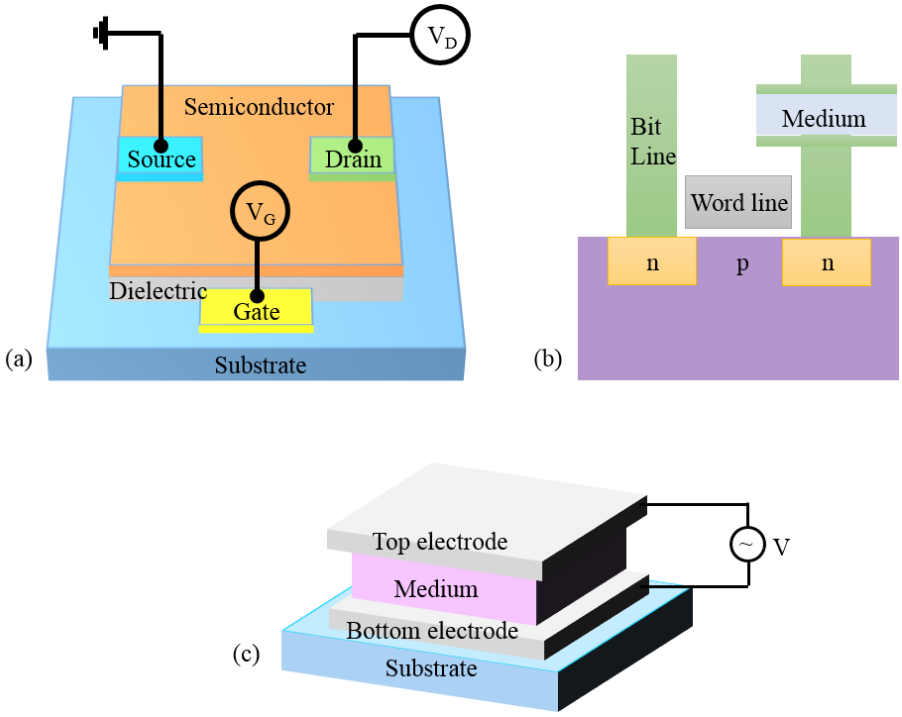

Figure 2.6 (a) The configuration of a top-contact transistor-type memory device. (b) The schematic setup of a typical capacitor-type memory cell. (c) The schematic diagram of a fundamental resistor-type memory structure.

As is discussed in previous paragraphs, new memories are in need for triggering the further development on information storage, because conventional silicon technology is encountering a severe bottleneck in contemporary nano-age. Graphene is considered

as a competitive material for new-generation high-performance memory devices due to its unique and well-proven characteristics. Its excellent carrier mobility could facilitate a high operating speed; its atomic-thin architecture provides encouraging possibilities for flexible nano-electronics and could lead to a remarkable integration density; its good compatibility could bring about low-cost products. These benefits cause active attention to utilize graphene-related materials for high-speed, high-density and energy-efficient memory devices[31,32]. Numerous studies have been carried out on theoretically investigating and practically fabricating graphene-based memory cells, although between the realistic results and the ideal expectations still exists a considerable performance gap. In the following discussion, graphene-based resistive memories are focused and several exciting research reports are highlighted.

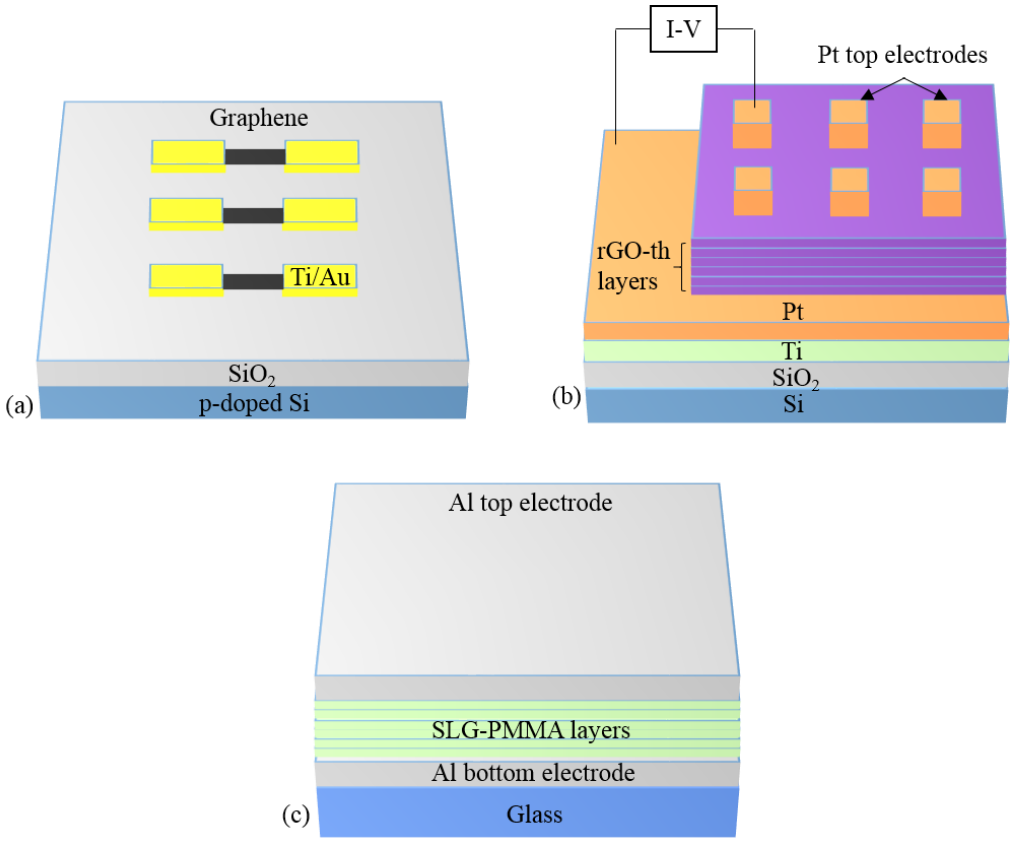

Figure 2.7 (a) The schematic configuration of the two-terminal graphene/SiO_2 multilevel resistive memory device. (b) The schematic diagram of the rGO-th based memory device. The rGO-th layers were grown on a commercial Pt/Ti/SiO_2/Si substrate, followed by the deposition of Pt top electrodes. (c) The schematic illustration of the SLG-PMMA nanocomposite based memristor.

The development of chemical vapour deposition (CVD) technique makes possible the growth of graphene on SiO_2 substrate. In 2012, He *et al*[33] investigated a non-volatile resistive memory based on a planar graphene/SiO_2 nanogap structure (see Fig. 2.7(a)). The multilayered graphene nanoribbon (GNR) film was grown and patterned on a commercial SiO_2 (300nm)/p-doped Si substrate using e-beam lithography and reactive ion etching (RIE) techniques. The following Ti/Au (2nm/30nm) deposition for electrodes was also carried out by e-beam lithography. Experimental results proved the good quality of this memory device, as its switching speed goes down to 500ns and retention time reaches up to over 10^5s. The switching mechanism is attributed to a reversible redox reaction process taken place at the breakdown area in the SiO_2 layer, which is significantly affected by the ambient temperature.

Except for pure graphene layer, derivatives of graphene are also popular in the memory industry, among which graphene oxide is one of the easiest forms. In 2012, Hu *et al*[34] reported a theoretical explanation and an experimental realization of a controllable electron transfer effect between the reduced graphene oxide (rGO) sheet and thionine (th) molecules, and demonstrated a non-volatile memory device based on this mechanism. The device configuration is displayed in Fig. 2.7(b). The rGO-th was synthesized by means of reducing graphene oxide in the thionine-mixed graphene oxide aqueous solution. It then turned into a 40nm-thin film by using the vacuum filtration technique at room temperature, and was transferred onto the platinum (Pt) surface. Experimental results indicate a satisfying performance of the memory device, as it exhibits bistable electrical switching with the ON/OFF ratio higher than 10^4, the switching speed less than 5ns, and the retention time longer than 10^5s. Although the rGO-th structure study provides a promising route in fabricating memory devices based on the mechanism of electron transfer, the disadvantage of graphene oxide introduction cannot be ignored, as defects generated during the synthesis process negatively affect the essential characteristics of graphene and therefore the performance of the subsequent electric devices.

Attracted by the favourable biocompatibility of organic materials, graphene/polymer nanomaterials are also utilized in fabricating memory devices. Wu *et al*[35] proposed a single-layer graphene (SLG)-poly (PMMA) hybrid structure based memristor in 2014. As shown in Fig. 2.7(c), the SLG-PMMA film, acting as the active layer, was

sandwiched between Al top and bottom electrodes. The film was spin-coated from a solution generated by dissolving the SLG/PMMA stacking configuration in the chloroform. The dispersed graphene nanosheets play the role of electron acceptors, and the electron trapping/detrapping effect is considered as the key factor attributed to the switching behaviour. As the carrier transport is largely influenced by thermally-excited charge emission processes, the quantity of electrons injected and captured varies greatly, depending on the voltage applied across the Al electrodes. The increase of bias voltage promotes the electron trapping process, while the decrease gradually leads to the thorough detrapping, which macroscopically displays as the switching between two stable states of the device. Practical measurement results prove the expected good performance of the system. As a volatile memristor, the retention time reaches several seconds (three times magnitude larger than the traditional resistive memory devices), and the ON/OFF ratio is in the magnitude of 10^6.

The aforementioned studies reveal the progress of unconventional graphene based memory devices. Intriguing features are demonstrated, however, limitations should still be discussed for promoting a further development especially in the circuit level. Firstly, the absence of bandgap set a barrier to the minimum static power consumption that graphene can achieve as a component in the logic circuits. Secondly, although hybrid structure is able to make up for the bandgap deficiency, it is detrimental to the scale-down operation. Therefore, the remaining tasks include the enhancement of the active element properties as well as the research toward system-level integration. In view of this fact, a nanoscale graphene quantum dot based memory device is a promising choice, which is the other primary topic present in this thesis and is well elucidated in ***Chapter Four***.

2.3. Fabrication Techniques

The fabrication of graphene-related nanodevices depend on several state-of-the-art techniques. Those relevant to this thesis work are demonstrated as follows.

2.3.1. Rapid Thermal Annealing (RTA)

Rapid thermal annealing refers to a heat treatment method frequently used in the region of semiconductor device fabrication. Compared to conventional furnace annealing

(CFA), RTA brings about particular changes to the atomic arrangement of a wafer surface in a more efficient and effective way. Take the commonly-used doped-Si wafer as an example. In principle, any thermal treatment on samples should be conducted without affecting the doping profile. However, when the classical furnace annealing is applied, the processing duration usually lasts so long (calculated in hours) that dopants are activated and redistributed and the junction depth is changed, which may result in completely different electrical properties. RTA overcomes this drawback due to its much higher heating rates (generally accomplished in minutes or even seconds)[36,37]. Besides, shorter processing duration reduces energy consumption, making RTA environmental-friendly. During RTA, a wafer is directly heated in the process chamber by utilizing the lamp radiation. Electric power applied on the lamp determines the radiation intensity and therefore the temperature inside the chamber. For the purpose of accurate controlling, the temperature is sensed by the thermocouple linked to the susceptor on which the wafer is located. Because of its ability in achieving more uniform and precise results[38], RTA rather than CFA is much more popular in the nanofabrication, especially the epitaxial growing field.

2.3.2. Physical Vapor Deposition (PVD)

Physical vapor deposition is exclusively used to manufacture thin films for specific functions based on physical processes. As a well-developed technique, it is widely used in fields ranging from decorative art to semiconductor thin-film electronics[39,40]. Advantages of PVD coating include high impact strength and remarkable abrasion resistance. As shown in Fig. 2.8, the PVD process is characterized by the transformation of a solid-state source into a gas phase and its reversion to a condensed phase with changes in physical morphology. A variety of materials can be used as the source, both organic and inorganic. By continuously applying heat to the source, particles in the material gain increased kinetic energy, making them capable of overcoming the separation energy and becoming vapor. The heating process can be conducted by using an electron beam or a cathodic arc, and the average kinetic energy varies according to the source material and evaporation temperature. The deposition step generally starts when the gas pressure in the chamber drops below 10^{-5}torr to avoid oxidation. The thickness of the deposited film can be as small as a few angstroms or several millimetres, depending on applications[41].

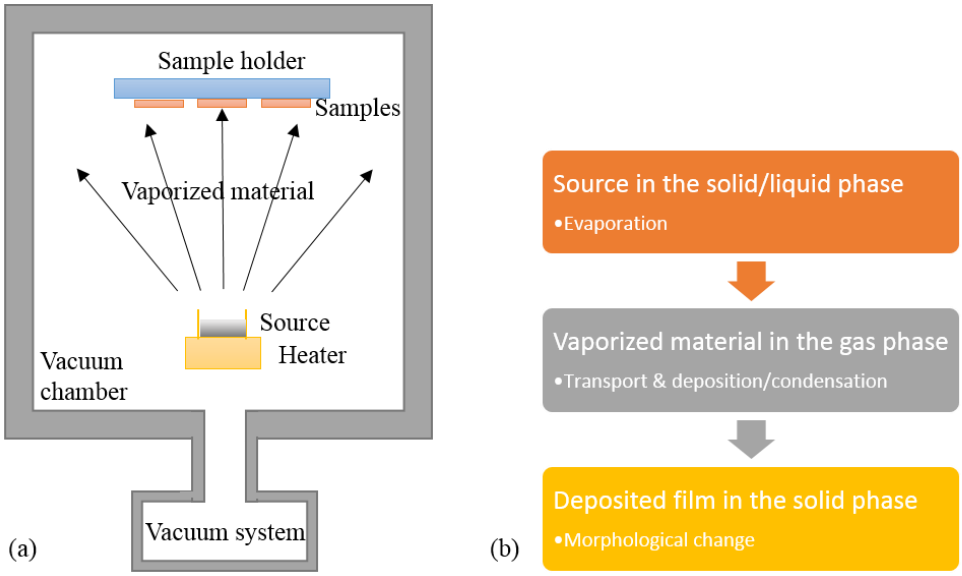

Figure 2.8 The (a) schematic setup and (b) process flow diagram of the general physical vapor deposition technique.

2.3.3. Electron Beam Lithography (EBL)

Electron beam lithography is considered as the most commonly-used lithography technique in the nanoscale field. It is a practical tool in creating structures in the microscopic level. Compared to conventional photolithography, EBL is primarily advantageous for its capability of direct patterning and ultra-high resolution. It has been reported to be able to generate versatile patterns with resolution as high as 10nm[42,43]. Fig. 2.9 illustrates the schematic diagram of a general EBL system in which the beam blanker acts as a switch and the beam deflector affects the position of the beam[44]. Normally, the resist-coated sample is exposed one pixel at a time with a finely focused electron beam performing either raster scan or vector scan. The total writing time is determined by three other parameters and is expressed as follows[44]:

$$T = (D \cdot A)/I \qquad (2.1)$$

where T is the exposure length, D is the exposure dose, A is the exposed area, and I is the electron beam current. Since the exposure speed of EBL is low (single pixel at a time), the overall writing time is usually long, which means a low throughput.

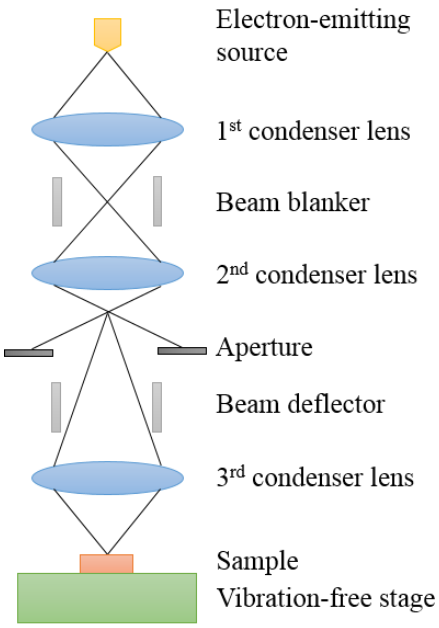

Figure 2.9 The schematic illustration of a maskless EBL (direct writing).

However, in spite of the throughput handicap, EBL has been successfully used in many applications due to its ability to produce patterns with nanometer feature sizes. It needs to be pointed out that the ultimate resolution of EBL is not only influenced by the electron optical system whose resolution can go down to 0.1nm, but more importantly determined by the electron scattering effect in the resist[45]. Forward scattering and back scattering are the two main scattering types. Forward scattering occurs more frequently but in a small angle, while backscattered electrons, even though occasionally generated, can lead to much larger unexpected exposure areas. Scattering is unavoidable, but can be decreased by adjusting the electron beam energy or changing the resist properties.

References

1. Pop, E. Energy dissipation and transport in nanoscale devices. *Nano Res.* **3,** 147–169 (2010).
2. Bhadrachalam, P. *et al.* Energy-filtered cold electron transport at room temperature. *Nat. Commun.* **5,** (2014).
3. Cavin, R. K., Zhirnov, V. V., Herr, D. J. C., Avila, A. & Hutchby, J. Research directions and challenges in nanoelectronics. *J. Nanoparticle Res.* **8,** 841–858 (2006).
4. Lake, R. & Datta, S. Energy balance and heat exchange in mesoscopic systems. *Phys. Rev. B* **46,** 4757–4763 (1992).

5. Bowers, A. S. E. Y. L. D. L. S. V. N. J. E. Thermoelectric Effects in Submicron Heterostructure Barriers. *Microscale Thermophys. Eng.* **2,** 37–47 (1998).
6. Koswatta, S. O., Lundstrom, M. S. & Nikonov, D. E. Influence of phonon scattering on the performance of p-i-n band-to-band tunneling transistors. *Appl. Phys. Lett.* **92,** 043125 (2008).
7. Edwards, H. L., Niu, Q. & de Lozanne, A. L. A quantum-dot refrigerator. *Appl. Phys. Lett.* **63,** 1815–1817 (1993).
8. Giazotto, F., Heikkilä, T. T., Luukanen, A., Savin, A. M. & Pekola, J. P. Opportunities for mesoscopics in thermometry and refrigeration: Physics and applications. *Rev. Mod. Phys.* **78,** 217–274 (2006).
9. Nahum, M., Eiles, T. M. & Martinis, J. M. Electronic microrefrigerator based on a normal-insulator-superconductor tunnel junction. *Appl. Phys. Lett.* **65,** 3123–3125 (1994).
10. Leivo, M. M., Pekola, J. P. & Averin, D. V. Efficient Peltier refrigeration by a pair of normal metal/insulator/superconductor junctions. *Appl. Phys. Lett.* **68,** 1996–1998 (1996).
11. Leoni, R., Arena, G., Castellano, M. G. & Torrioli, G. Electron cooling by arrays of submicron tunnel junctions. *J. Appl. Phys.* **85,** 3877–3881 (1999).
12. Pekola, J. P. *et al.* Microrefrigeration by quasiparticle tunnelling in NIS and SIS junctions. *Phys. B Condens. Matter* **280,** 485–490 (2000).
13. Clark, A. M., Williams, A., Ruggiero, S. T., van den Berg, M. L. & Ullom, J. N. Practical electron-tunneling refrigerator. *Appl. Phys. Lett.* **84,** 625–627 (2004).
14. Pekola, J. P., Giazotto, F. & Saira, O.-P. Radio-Frequency Single-Electron Refrigerator. *Phys. Rev. Lett.* **98,** (2007).
15. Luukanen, A., Leivo, M. M., Suoknuuti, J. K., Manninen, A. J. & Pekola, J. P. On-Chip Refrigeration by Evaporation of Hot Electrons at Sub-Kelvin Temperatures. *J. Low Temp. Phys.* **120,** 281–290 (2000).
16. Prance, J. R. *et al.* Electronic Refrigeration of a Two-Dimensional Electron Gas. *Phys. Rev. Lett.* **102,** (2009).
17. Gasparinetti, S. *et al.* Probing the local temperature of a 2DEG microdomain with a quantum dot: measurement of electron-phonon interaction. *Phys. Rev. B* **83,** (2011).

18. Yu, C., Shi, L., Yao, Z., Li, D. & Majumdar, A. Thermal Conductance and Thermopower of an Individual Single-Wall Carbon Nanotube. *Nano Lett.* **5,** 1842–1846 (2005).

19. Nika, D. L., Pokatilov, E. P., Askerov, A. S. & Balandin, A. A. Phonon Thermal Conduction in Graphene. *ArXiv08120518 Cond-Mat* (2008).

20. Lee, J.-S. Review paper: Nano-floating gate memory devices. *Electron. Mater. Lett.* **7,** 175 (2011).

21. Arora, A. *Foundations of Computer Science*. (Laxmi Publications, 2006).

22. Mittal, S. & Vetter, J. S. A Survey of Software Techniques for Using Non-Volatile Memories for Storage and Main Memory Systems. *IEEE Trans. Parallel Distrib. Syst.* **27,** 1537–1550 (2016).

23. Ling, Q.-D. *et al.* Polymer electronic memories: Materials, devices and mechanisms. *Prog. Polym. Sci.* **33,** 917–978 (2008).

24. Mao, D. *et al.* Ferroelectric random access memory based on one-transistor–one-capacitor structure for flexible electronics. *Org. Electron.* **14,** 505–510 (2013).

25. Zhang, B., Chen, Y., Neoh, K.-G. & Kang, E.-T. CHAPTER 1:Organic Electronic Memory Devices. in *CHAPTER 1:Organic Electronic Memory Devices* 1–53 (2015).

26. Chua, L. Resistance switching memories are memristors. *Appl. Phys. A* **102,** 765–783 (2011).

27. Tseng, R. J. *et al.* Charge transfer effect in the polyaniline-gold nanoparticle memory system. *Appl. Phys. Lett.* **90,** 053101 (2007).

28. Syu, Y. E. *et al.* Redox Reaction Switching Mechanism in RRAM Device With $hboxPt/CoSiO_Xhbox/hboxTiN$ Structure. *IEEE Electron Device Lett.* **32,** 545–547 (2011).

29. Kwan, W. L., Lei, B., Shao, Y. & Yang, Y. Understanding the switching mechanism of polymer memory. *Curr. Appl. Phys.* **10,** e50–e53 (2010).

30. Hwang, S. K. *et al.* Flexible Multilevel Resistive Memory with Controlled Charge Trap B- and N-Doped Carbon Nanotubes. *Nano Lett.* **12,** 2217–2221 (2012).

31. Geim, A. K. & Novoselov, K. S. The rise of graphene. *Nat. Mater.* **6,** 183–191 (2007).

32. Kim, K., Choi, J.-Y., Kim, T., Cho, S.-H. & Chung, H.-J. A role for graphene in silicon-based semiconductor devices. *Nature* **479,** 338–344 (2011).

33. He, C. *et al.* Multilevel Resistive Switching in Planar Graphene/SiO2 Nanogap Structures. *ACS Nano* **6,** 4214–4221 (2012).

34. Hu, B. *et al.* Electrically controlled electron transfer and resistance switching in reduced graphene oxide noncovalently functionalized with thionine. *J. Mater. Chem.* **22,** 16422–16430 (2012).

35. Wu, C., Li, F. & Guo, T. Formation and carrier transport properties of single-layer graphene/poly (methyl methacrylate) nanocomposite for resistive memory application. *Vacuum* **101,** 246–249 (2014).

36. Lie, D. Y. C., Song, J. H., Nicolet, M. -A. & Theodore, N. D. Advantage of rapid thermal annealing over furnace annealing for P-implanted metastable Si/Ge0.12Si0.88. *Appl. Phys. Lett.* **66,** 592–594 (1995).

37. Tripathy, N., Das, K. C., Ghosh, S. P., Bose, G. & Kar, J. P. Effect of rapid thermal annealing on the structural and electrical properties of RF sputtered CCTO thin film. *IOP Conf. Ser. Mater. Sci. Eng.* **178,** 012009 (2017).

38. Juang, M. H. & Cheng, H. C. Conventional furnace and rapid thermal annealing of cobalt films on Si(111). *Thin Solid Films* **216,** 219–224 (1992).

39. Fortunato, E., Barquinha, P. & Martins, R. Oxide Semiconductor Thin-Film Transistors: A Review of Recent Advances. *Adv. Mater.* **24,** 2945–2986

40. Selvakumar, N. & Barshilia, H. C. Review of physical vapor deposited (PVD) spectrally selective coatings for mid- and high-temperature solar thermal applications. *Sol. Energy Mater. Sol. Cells* **98,** 1–23 (2012).

41. Reichelt, K. & Jiang, X. The preparation of thin films by physical vapour deposition methods. *Thin Solid Films* **191,** 91–126 (1990).

42. Tseng, A. A., Chen, K., Chen, C. D. & Ma, K. J. Electron beam lithography in nanoscale fabrication: recent development. *IEEE Trans. Electron. Packag. Manuf.* **26,** 141–149 (2003).

43. Chen, Y. Nanofabrication by electron beam lithography and its applications: A review. *Microelectron. Eng.* **135,** 57–72 (2015).

44. Parker, N. W., Brodie, A. D. & McCoy, J. H. High-throughput NGL electron-beam direct-write lithography system. in (ed. Dobisz, E. A.) 713–720 (2000). doi:10.1117/12.390042

45. Broers, A. N., Hoole, A. C. F. & Ryan, J. M. Electron beam lithography—Resolution limits. *Microelectron. Eng.* **32,** 131–142 (1996).

3. ENERGY-FILTERED ELECTRON TRANSPORT STRUCTURES FOR LOW-POWER LOW-NOISE 2-D ELECTRONICS

In addition to cryogenic techniques, energy filtering has the potential to achieve high-performance low-noise 2-D electronic systems. Assemblies based on graphene quantum dots (GQDs) have been demonstrated to exhibit interesting transport properties, including resonant tunnelling. In this chapter, GQDs based structures are investigated with the goal of producing energy filters for next generation lower-power lower-noise 2-D electronic systems. Electron transport properties of the proposed GQD device structures are evaluated to demonstrate electron energy filtering and the ability to control the position and magnitude of the energy passband by appropriate device dimensioning. It is also showed that the signal-to-(thermal) noise ratio performance of the proposed nanoscale device can be modified according to device geometry. The tunability of two-dimensional GQD structures indicates a promising route for the design of electron energy filters to produce low-power and low-noise electronics.

3.1. Introduction

In electron-based transport systems, such as 2-D graphene electronics, the electrons have an energy distribution that is described by the Fermi-Dirac statistic which indicates that the kinetic energy of electrons participating in charge transport varies considerably. Electrons with high kinetic energies have higher momentum and impart higher momentum, upon collision, to the lattice as they traverse the device channel, in the process generating more heat, noise and leading to undesirable effects such as electromigration.

The spatial power dissipation within structures can be calculated using the drift-diffusion approach[1–4]:

$$P_V = \boldsymbol{J} \cdot \boldsymbol{E} + (R - G)(E_G + 3k_B T) \tag{3.1}$$

where $\boldsymbol{J}$ is the current density which counts all carriers that are participating in charge transport, $\boldsymbol{E}$ is the electric field, (R-G) is the net non-radiative recombination rate, E_G is the semiconductor band gap, k_B is the Boltzmann constant and T is the lattice temperature. The total power dissipated is determined by integrating P_V (power density per unit volume) over the device volume.

The total current density[5] is given by:

$$\boldsymbol{J} = \frac{\boldsymbol{I}}{a} = \frac{q}{ah}\int_{\mu_R}^{\mu_L} T(E)[f(E-\mu_L) - f(E-\mu_R)]dE \tag{3.2}$$

where $\boldsymbol{I}$ is the current, a is the area coefficient, q is the electronic charge, h is the Planck constant, $T(E)$ is the transmission function at an energy level E, $\mu_{L,R}$ are the electrochemical potentials of the left and right electrodes, f is the Fermi-Dirac distribution of electrons.

The noise density at finite frequency ω for the energy band [E, E+dE] is[6–8]:

$$S(\omega, E)dE = \frac{4q^2}{h} f(E)[2 - f(E+\hbar\omega) - f(E-\hbar\omega)]dE \tag{3.3}$$

where $\hbar$ is the reduced Planck constant and f is the Fermi Dirac distribution. The total current noise is the integral of the noise density across the allowable energy ranges and

frequencies. As the power spectral density, *S(ω),* is a positive definite function, electron energy filtering is able to help decrease the noise, as is mathematically proved by the following functions[8]:

$$N_\infty(\omega) = \int_0^\infty S(\omega, E)dE = \frac{4q^2}{h}\int_0^\infty f(E)[2 - f(E+\hbar\omega) - f(E-\hbar\omega)]dE$$
$$= 2G\hbar\omega coth\frac{\hbar\omega}{2k_BT}$$

$$N_E(\omega) = \int_{E_2}^{E_1} S(\omega, E)dE = \frac{4q^2}{h}\int_{E_2}^{E_1} f(E)[2 - f(E+\hbar\omega) - f(E-\hbar\omega)]dE \quad (3.4)$$

$$N_E \leq N_\infty$$

where G is the total conductance, N_E is the current noise over a finite energy domain, and N_∞ is the generalized Nyquist noise formula which reduces to Johnson-Nyquist thermal noise $4K_BTG$ in the limit of $\hbar\omega \ll k_BT$ and the quantum zero-point noise $2\hbar\omega G$ in the limit of $\hbar\omega \gg k_BT$.

Reducing energy dissipation and noise in nanoscale electronics are important challenges in the design of 2-D circuits and systems. Considering equations (3.1) – (3.4), it can be seen that the decrease of noise can be achieved by reducing the energies of electrons that participate in the transport. This is because the total current noise is the integration of the noise density, a positive definite quantity, over all the allowable energy levels. If the integral interval is reduced, the value of the integral, because the noise power spectral density at any energy level is a positive number or zero, will also reduce. The reduction of the noise then leads to the reduction of the signal and consequently the power required to achieve the same signal-to-noise ratio (SNR). Dimensional confinement on devices leads to discrete energy levels[9–11] which can serve as energy filters as only electrons whose energies match the discrete energy levels are allowed to participate in the tunnelling[12] and transport, therefore helping to limit the total current noise and power dissipation.

The study of electron transport in QD-based devices has been one of the foci in quantum physics[13]. Because of the quantum confinement, quantum dots have sharper density of state distributions than higher dimensional structures, which has led to them being investigated for use in diode lasers, amplifiers, biological sensors, *etc*[13,14]. Unique electronic properties in quantum dots include: highly nonlinear I-V characteristics,

negative differential resistance (NDR) and electrical switching[15–17]. The discrete energy distribution in QDs allows for interesting current-voltage characteristics to be observed where contrary to the conventional Ohmic relationship holding, a decrease in current is noticed with the increase in applied bias when NDR is presented. This property can be considered in building electron energy band-pass filters.

Several methods have been investigated to obtain a pronounced NDR effect, including adsorption of different molecules on quantum dots, varying the shape of quantum dots, use of specific materials as electrodes, *etc*[18–21]. Zheng *et al.*[14] studied the electron transport properties of a C_{60}-based electronic device, where two C_{60}s were linked by an alkane chain, and highlighted that the NDR can be controlled by the length of the linker; Zhang *et al.*[22] focused on the transport properties of GQDs sandwiched between two semi-infinite zigzag-edged GNR electrodes, showing that the size of QDs effects the number and position of resonant peaks; Perrin *et al.*[23] reported upon experiments where a pronounced negative differential resistance was observed in the current-voltage characteristics of a single molecule located in a break junction. In the above-mentioned systems, even though NDR behaviours can be generated, they occur at a relatively high bias (1-2V), which can limit their application to low power electronics.

In this chapter, with a GQD as the basic building block, we construct a fundamental two-terminal energy filter where NDR is obtained at low bias and quantum tunnelling achieves high peak-to-valley current ratio (PVCR). In order to develop a design methodology to control the NDR effect, several versions of the structure are proposed. Doubling GQDs in a symmetrical way can lead to multiple negative resistance regions (and energy passbands), whilst the in-plane parallel GQDs structure causes a displacement of current peak without greatly affecting its magnitude.

3.2. Theory and Design

The model structures studied here are constructed as follows: in a two-terminal side-gate device, the metallic side gates in the device are graphene nanoribbons (GNRs) with widths of 6 carbon atoms, while the semiconducting channel is a zigzag GQD with a width of eight carbon atoms. The whole system is divided into three parts: the semi-infinite left electrode (L), the semi-infinite right electrode (R), and the central scattering region (C). The device geometry has been optimized and the coordinates have been

relaxed using the Brenner potential[28] with the maximum interatomic force no more than 0.05eV/Å.

The calculations are carried out using the Extended Hückel method as implemented in ATK-SemiEmpirical (ATK-SE) package[29]. This semi-empirical method determines the electron transport in the GQD structure by overlooking the non-elastic electron-electron repulsion and conveying the total energy as a linear sum of the term for each electron[35]. ETH is primarily cherished for its good transferability and decent computational burden without losing the calculation accuracy. In the Atomistix software, the mesh points are defined as uniformly spaced k points of 1×1×50 for all devices, with 50 sample points along the transport direction of the two-terminal structure. The conductance and nonlinear I-V characteristics are studied by the non-equilibrium Green's Function (NEGF) formalism[30,31] based on optimally localized orbitals[32,33]. The transmission function is obtained from the Landauer formula[34]:

$$T(E) = Trace[\Gamma_L G \Gamma_R G^+] \tag{3.5}$$

where G and G^+ are the retarded and advanced Green's functions of the central scattering region respectively, and $\Gamma_{L,R}$ describes the coupling of left/right electrodes with the central part. The coherent current through the system is given by the integration of the transmission function over the bias window:

$$I(V_L, V_R) = \frac{q}{h}\int_{\mu_R}^{\mu_L} T(E)[f(E-\mu_L) - f(E-\mu_R)]dE$$
$$\mu_R - \mu_L = q(V_L - V_R) \tag{3.6}$$

where $V_{L,R}$ are the left and right electrode potentials respectively, q is the electronic charge, h is the Planck constant, $\mu_{L,R}$ are the electrochemical potentials of the two electrodes, f is the Fermi-Dirac distribution of electrons.

3.3. Results and Discussion

The structure of the elementary GQD device studied here is shown in Fig. 3.1(a). It consists of one zigzag GQD surrounded by two carbon nano-ribbon electrodes. All dangling bonds were passivated with hydrogen atoms. The atomic structure was fully relaxed using the quick optimization calculation method. After relaxation, the potential

of the right electrode was set to be zero and the left electrode was set to be the bias voltage. A pronounced NDR feature is exhibited at a low bias: starting from 0.6V bias, the current increases initially, reaching a maximum of about 230nA at 0.7V, thereafter it sharply decreases (see Fig. 3.1(b)). The PVCR is defined as follows:

$$PVCR = \frac{C_p - C_v}{\delta V} \tag{3.7}$$

where Cp and Cv are peak and valley currents respectively, and δV is the corresponding voltage difference. The PVCR in our proposed device is approximately 2300 nA/V.

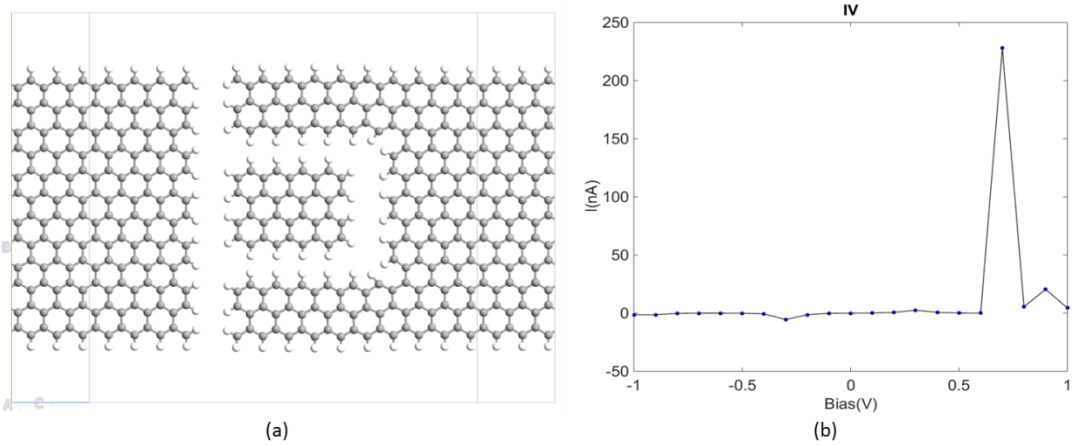

Figure 3.1 (a) The atomic structure of the graphene quantum dot side-gate device; grey and white spheres represent carbon and hydrogen atoms, respectively. (b) The calculated I-V curve.

To understand the operation of the GQD side-gate device, the equilibrium energy level diagram, with the assumption that no voltage was applied between the source and the drain, was illustrated in Fig. 3.2. A central factor in determining the current flow through the GQD is the location of the Fermi energy of the contacts relative to the energy levels of the GQD. Current flow requires the source to inject carriers into the GQD energy levels. The current is high if the Fermi level of the source aligns with one of the unoccupied energy levels[24]. However, this is not the case under equilibrium, where the Fermi level always lies close to the charge neutrality level near the center of the gap, leading to minimal current at contact/GQD interfaces. The onset of current flow occurs when electrons gain sufficient energy to tunnel from the chemical potential of the source to the LUMO. Under bias, the energy of the LUMO and the Fermi level of the source can be shifted by electrostatic and charging-induced changes in potential. So as the drain-source bias increases, when the chemical potential of the source

becomes close enough to the LUMO energy, charging on the GQD is non-negligible, and the current increases with the GQD charge. Finally, a maximum charge density is reached when the chemical potential is aligned with the LUMO, which is reflected as the current peak at 0.7V in Fig. 3.1(b). Further increases in applied bias lead to a decrease rather than an increase of the charging energy or the current flow, owing to the discrete band structure of the GQD and the misalignment between energy levels.

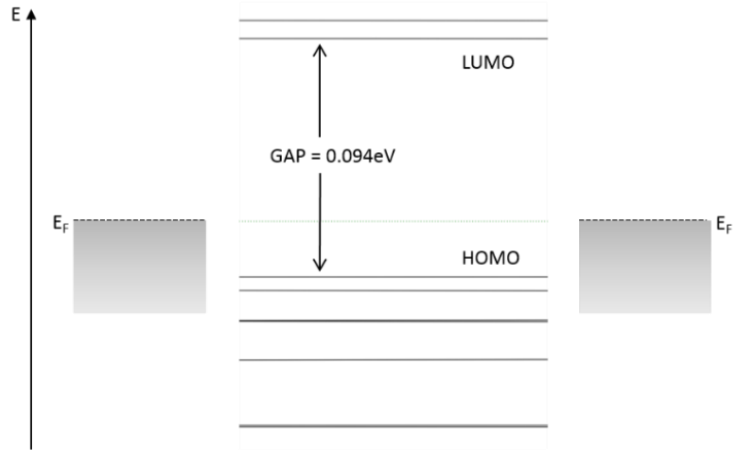

Figure 3.2 The schematic band diagram showing the energy levels in the bulk GQD side-gate device and the Fermi level (E_F) in the contacts. The highest occupied molecular orbital (HOMO) was separated by a gap of 0.094eV from the lowest unoccupied molecular orbital (LUMO).

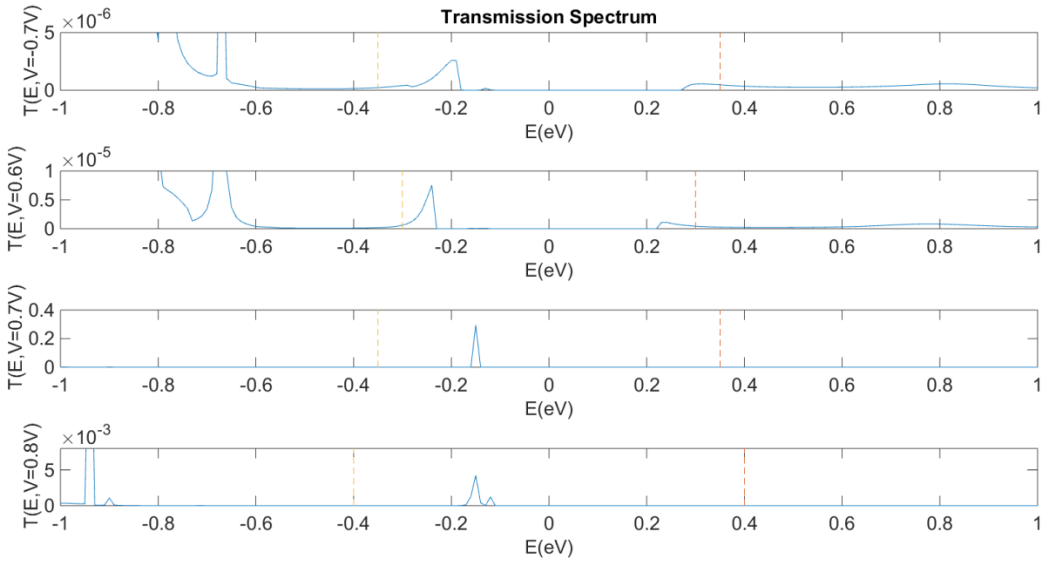

Figure 3.3 The evolution of the transmission spectrum as a function of bias voltage in the GQD side-gate device. The two vertical lines indicate the bias window.

The transmission functions T(E) for four biases were calculated and are plotted in Fig. 3.3. According to the Landauer formula, T(E) is the rate at which electrons with energy E are transmitted from the source to the drain by propagating through the device[25,26]. For a given bias voltage, the current can be calculated by integrating T(E) across the energy range of the bias window. In Fig. 3.3, with the bias voltage fixed at 0.7V, a sharp peak is located inside the bias window with an energy value of -0.15eV, relative to the Fermi level, and the T(E) value being 0.3. This value of the transmission function is larger than the corresponding ones under the other three simulated bias voltages (-0.7V, 0.6V and 0.8V) by at least two orders of magnitude.

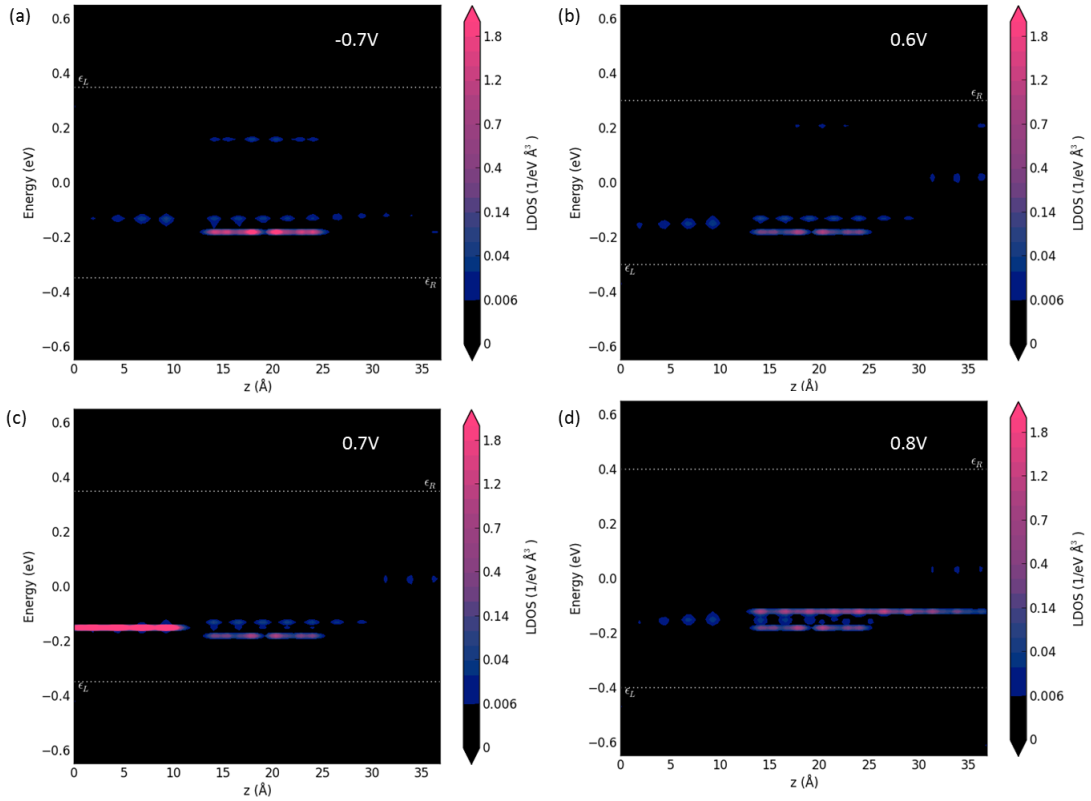

Figure 3.4 The position-dependent LDOS as a function of bias voltage in the GQD side-gate device. (a), (b), (c) and (d) are position-dependent LDOS plots under -0.7V, 0.6V, 0.7V and 0.8V bias voltages at -0.2eV, -0.25eV, -0.15eV, and -0.15eV respectively. The variable z indicates position along the transport direction.

The physical explanation for the features in T(E) can be derived from the density of states (DOS). The DOS shows the number of energy eigenstates in a material per unit energy, and is proportional to the quantum capacitance[5]. At certain energy level, the larger the DOS is, the larger the quantum capacitance will be, and the more charge can be transferred without shifting the level. From Fig. 3.2 we can see that the GQD has a

non-uniform density of states. Darker and thicker energy lines reflect increased DOS. Therefore, the transmission function varies depending on energy position, leading to peaks and valleys in the transmission spectrum.

Based on the structure's transmission spectrum at 0.7V and at 300K, the Nyquist thermal noise power with the GQD filter is -86.99dBm, whilst without the filter is equal to -21dBm.

Position-dependent local density of states (LDOS), which are plotted in Fig. 3.4 for various biases, offers another explanation for the occurrence of the NDR at 0.7V bias. The LDOS can be determined by solving time-independent Schrodinger equation[27]:

$$E\varphi(\boldsymbol{r}) = \left[\frac{-h^2}{2\mu}\nabla^2 + V(\boldsymbol{r})\right]\varphi(\boldsymbol{r}) \tag{3.8}$$

where $\varphi(\boldsymbol{r})$ is the wave function of the quantum system, μ is the reduced mass, ∇^2 is the Laplacian, $V(\boldsymbol{r})$ is the electrostatic potential energy, and E is the energy which directly corresponds to LDOS. Both $\varphi(\boldsymbol{r})$ and $V(\boldsymbol{r})$ are position-dependent. $V(\boldsymbol{r})$ can be written as:

$$V(\boldsymbol{r}) = V^* + \Delta V \tag{3.9}$$

where V^* is a constant that denotes the structure's intrinsic electrostatic potential and ΔV is the variation of electrostatic potential due to the applied bias voltage. In Fig. 3.4 the high number of LDOS manifests in the left electrode only when a bias of 0.7V is applied. It indicates that under this condition, electrons have a much greater probability of tunnelling from source, GQD and then drain, which contributes to the transmission peak in the transmission spectrum plots (Fig. 3.3). The integration window and the distribution of the transmission function give rise to the NDR peak at 0.7V in the I-V curve.

To study the impact of different sections (especially the quantum dot and the side gates) on the NDR effect, in Fig. 3.5(a), we show four comparable simulated structures, in which D1 is the key structure proposed here for energy filtering, whilst D2, D3, and D4 are all variants of the structure D1. The quantum dot and side gates were removed in D2 and D3 respectively, whilst D4 contains only one uniform gap with a width of 0.3nm.

From the plots (see Fig. 3.5(b) and 3.5(c)), we can establish that the sharp peak only occurs in structure D1 (The inclusion of side gates and quantum dot in combination with the nanoribbon control the NDR effect).

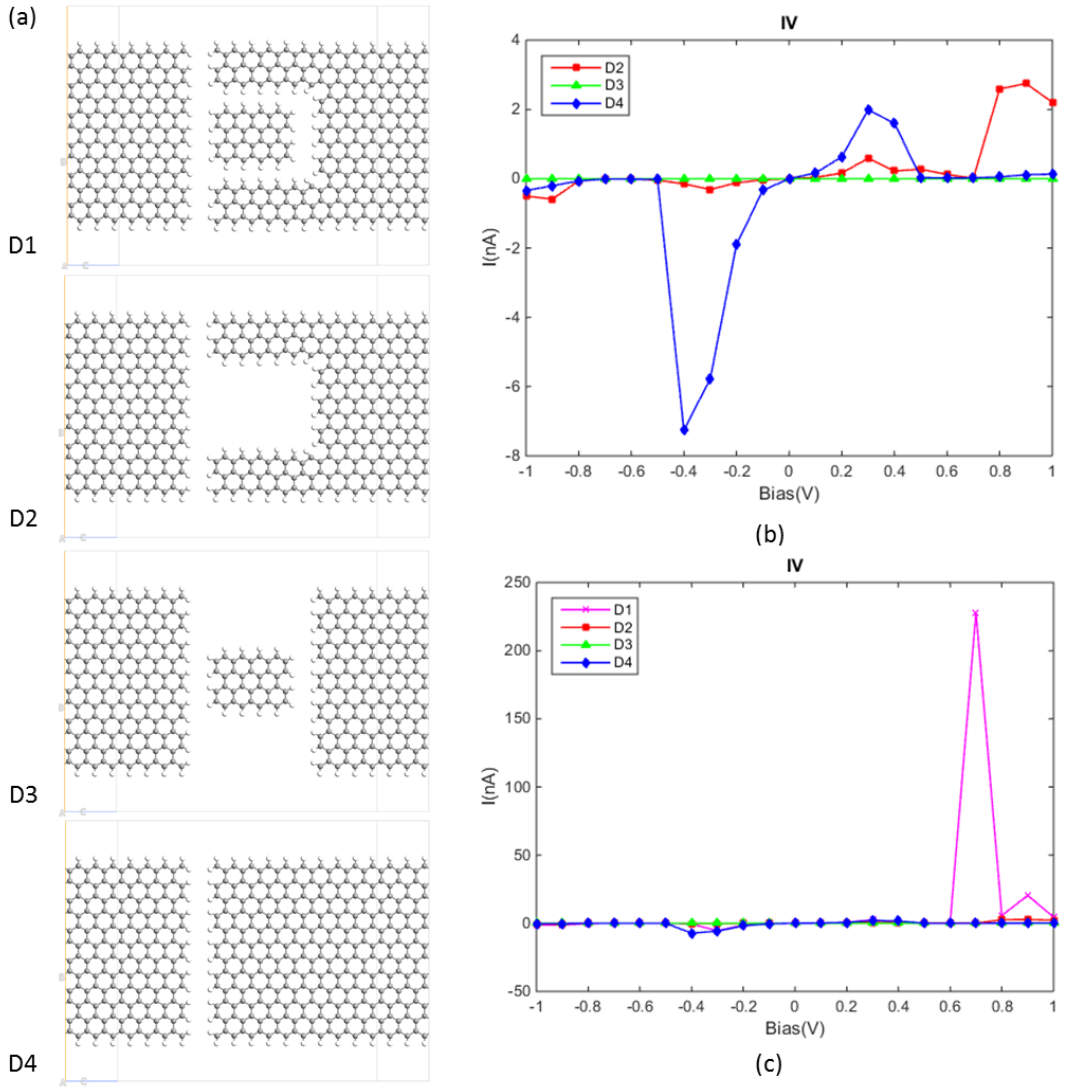

Figure 3.5 (a) Atomic structures of four different devices. (b) The calculated I-V curves for D2, D3, D4. (c) The calculated I-V curves for all four devices.

Table 3.1 The signal-to-thermal noise ratio for structures D1, D2, D3 and D4

Structures	Thermal noise power (dBm)	Signal power (dBm)	Signal-to-thermal noise ratio (dB)
D1	-86.99	-37.96	49.1
D2	-78.86	-56.14	22.7
D3	-33.37	-129.21	-95.9
D4	-84.81	-55.53	29.2

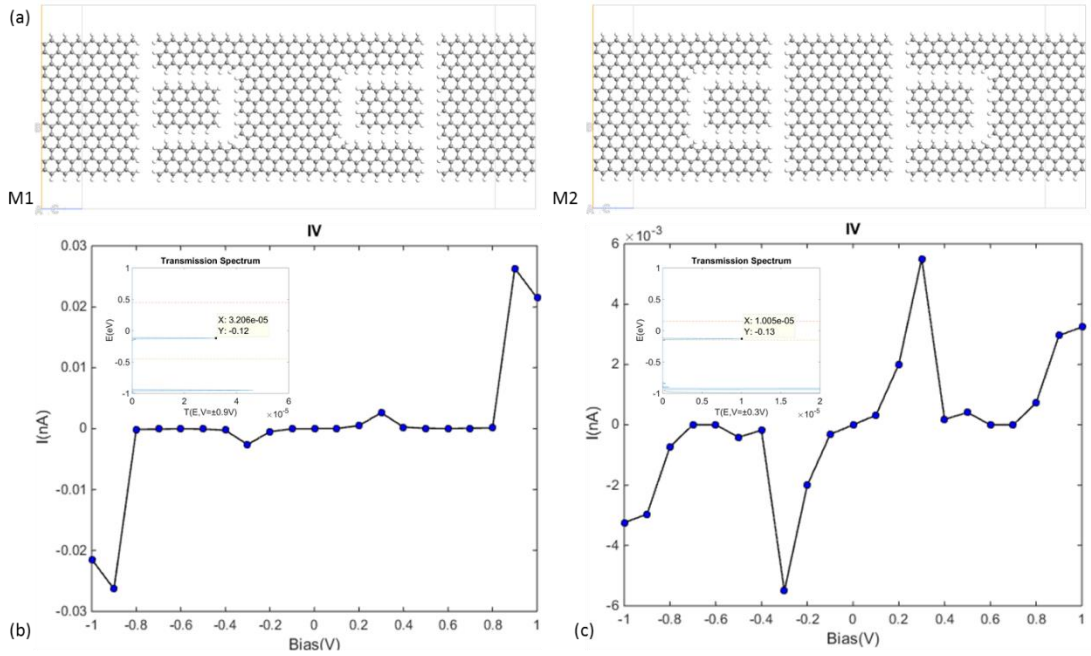

Figure 3.6 (a) Atomic structures of two geometrically symmetrical devices. (b) The calculated I-V curve for M1. Inset, the transmission spectrum under ±0.9V bias voltages. The peak of the energy passband locates at -0.12eV with the T(E) value being 3.2×10^{-5}. (c) The calculated I-V curve for M2. Inset, the transmission spectrum under ±0.3V bias voltages. The peak of the energy passband locates at -0.13eV with the T(E) value being 1.0×10^{-5}. The two horizontal lines indicate the bias window.

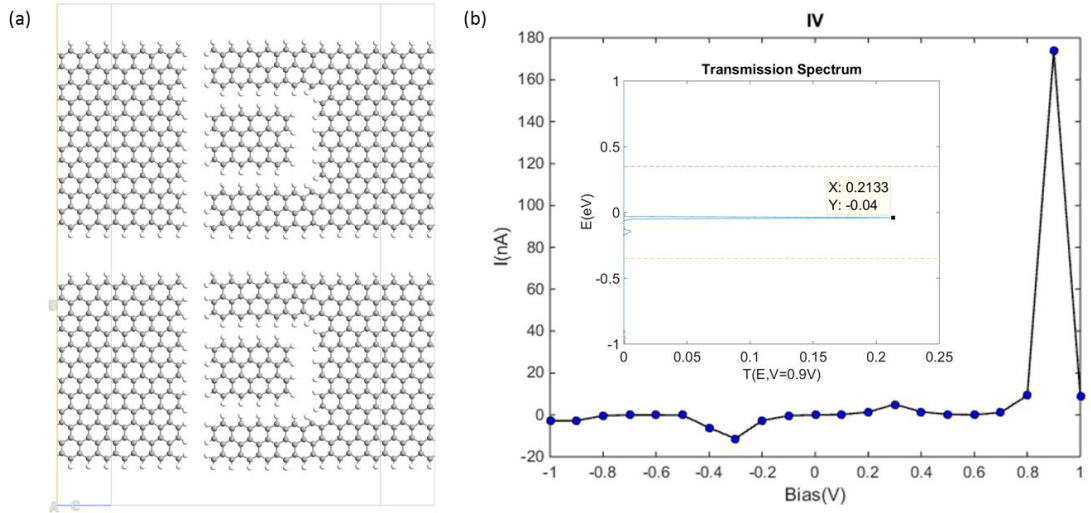

Figure 3.7 (a) The atomic structure of the double parallel-connected device. (b) The calculated I-V curve. Inset, the transmission spectrum under 0.9V bias. The two horizontal lines indicate the bias window.

Based on the equation (3.4), the signal-to-thermal noise ratio for structures D1 – D4 were calculated at room temperature (300K) (see Table 3.1). D1 exhibits the best signal-

to-thermal noise ratio performance because of its lowest thermal noise power and highest signal power, which is, in essence, attributed to the energy filtering and tunneling effect of the quantum dot structure. By adjusting the device configuration, the noise and signal power can be tuned separately. For example, D1 and D4 have approximately the same thermal noise power, whilst the signal power for D1 is higher by two orders of magnitude. D2 and D4, conversely, have more obvious difference lie in the thermal noise power. It is also noteworthy to point out that the ultra-low signal power level for D3 indicates the fact that the resonant tunneling almost does not happen in this case, which suggests the influence of channel width on the tunneling effect.

Since the NDR is affected by electrostatic distribution, its magnitude and position can be varied by changing the distribution of electrical field. As examples, we considered two kinds of symmetrical extensions on the central region of the fundamental device (see Fig. 3.6(a)). The role of the added GQD is to shift the Fermi level and build symmetry between the forward and reverse currents. After extension, double and multi-NDR effects were achieved. In contrast to the single GQD-based device, the I-V curves for the new structures are symmetrical for positive and negative bias. In M1 the positions of the current peaks shifted to ±0.9V whilst in M2 the NDR effects appeared most prominently at ±0.3V and ±0.9V (see Fig. 3.6(b) and 3.5(c)). The transmission spectrum plots (insets of Fig. 3.6(b) and Fig. 3.6(c)) reveal that the magnitudes of the energy passbands were tuned largely with little impact on their positions.

Furthermore, an in-plane parallel connection of multiple devices turned out to be able to tune the positions of the current peak as well as the energy passband without significantly influencing their magnitudes. In Fig. 3.7(b), the NDR started from 0.9V bias with the maximum current reaching 170nA, and the energy passband occurred in the domain of [-0.05eV, -0.03eV] with the peak value of 0.2.

3.4. Conclusion

Reduction in power consumption, reliability and noise are important considerations in 2-D electronics. In this chapter, we show that electron filtering and NDR can be achieve by the miniaturization of conductors and this can be exploited to reduce noise in electronic devices. We proposed several configurations of two-terminal devices with

GQD(s) as the basic building block and investigated their transport properties. We found that the electron conduction is mediated by the electrostatic potential distribution which attributes to the joint effect of the device structure and the external applied electric field. As the distribution varies, the energy filtering feature and the NDR effect appear. It is important to note that the proposed symmetrical multi-NDR effect can be realized by mirroring GQD based on different axes or in other ways that affect the relative positions of Fermi levels of electrodes and GQDs. The magnitude and position of energy passbands and the signal-to-thermal noise power ratio can also be tuned with the adjustment of the device geometry. The possibility of controlling both the energy filtering and the NDR effect provides design flexibility when devising GQD based electronic devices and can be used to adapt structures to meet different requirements on low power consumption and low current noise.

References

1. Wachutka, G. K. Rigorous thermodynamic treatment of heat generation and conduction in semiconductor device modeling. *IEEE Trans. Comput.-Aided Des. Integr. Circuits Syst.* **9,** 1141–1149 (1990).
2. Lindefelt, U. Heat generation in semiconductor devices. *J. Appl. Phys.* **75,** 942–957 (1994).
3. Sverdrup, P. G., Sungtaek Ju, Y. & Goodson, K. E. Sub-Continuum Simulations of Heat Conduction in Silicon-on-Insulator Transistors. *J. Heat Transf.* **123,** 130–137 (2000).
4. Lai, J. & Majumdar, A. Concurrent thermal and electrical modeling of sub-micrometer silicon devices. *J. Appl. Phys.* **79,** 7353–7361 (1996).
5. Datta, S. *Quantum Transport: Atom to Transistor*. (Cambridge University Press, 2005).
6. BERNARD, W. & CALLEN, H. B. Irreversible Thermodynamics of Nonlinear Processes and Noise in Driven Systems. *Rev. Mod. Phys.* **31,** 1017–1044 (1959).
7. Landauer, R. Johnson-Nyquist noise derived from quantum mechanical transmission. *Phys. Nonlinear Phenom.* **38,** 226–229 (1989).
8. Yamamoto, Y. *Fundamentals of Noise Processes*. (Cambridge University Press, 2004).

9. van der Wiel, W. G. *et al.* Electron transport through double quantum dots. *Rev. Mod. Phys.* **75,** 1–22 (2002).
10. van der Vaart, N. C. *et al.* Resonant Tunneling Through Two Discrete Energy States. *Phys. Rev. Lett.* **74,** 4702–4705 (1995).
11. Kouwenhoven, L. Coupled quantum dots as artificial molecules. *Science* **268,** 1440 (1995).
12. Bhadrachalam, P. *et al.* Energy-filtered cold electron transport at room temperature. *Nat. Commun.* **5,** (2014).
13. Ponomarenko, L. A. *et al.* Chaotic Dirac Billiard in Graphene Quantum Dots. *Science* **320,** 356–358 (2008).
14. Zheng, X., Lu, W., Abtew, T. A., Meunier, V. & Bernholc, J. Negative Differential Resistance in C60-Based Electronic Devices. *ACS Nano* **4,** 7205–7210 (2010).
15. Joo, S. S. *et al.* Graphene-quantum-dot nonvolatile charge-trap flash memories. *Nanotechnology* **25,** 255203 (2014).
16. Shi, X., Zheng, X., Dai, Z., Wang, Y. & Zeng, Z. Changes of Coupling between the Electrodes and the Molecule under External Bias Bring Negative Differential Resistance. *J. Phys. Chem. B* **109,** 3334–3339 (2005).
17. Gorman, C. B., Carroll, R. L. & Fuierer, R. R. Negative Differential Resistance in Patterned Electroactive Self-Assembled Monolayers. *Langmuir* **17,** 6923–6930 (2001).
18. Chen, J., Reed, M. A., Rawlett, A. M. & Tour, J. M. Large On-Off Ratios and Negative Differential Resistance in a Molecular Electronic Device. *Science* **286,** 1550–1552 (1999).
19. Lyo, I.-W. & Avouris, P. Negative Differential Resistance on the Atomic Scale: Implications for Atomic Scale Devices. *Science* **245,** 1369–1371 (1989).
20. Seminario, J. M., Zacarias, A. G. & Tour, J. M. Theoretical Study of a Molecular Resonant Tunneling Diode. *J. Am. Chem. Soc.* **122,** 3015–3020 (2000).
21. Seminario, J. M., Cordova, L. E. & Derosa, P. A. An ab initio approach to the calculation of current-voltage characteristics of programmable molecular devices. *Proc. IEEE* **91,** 1958–1975 (2003).
22. Zhang, Y., Xie, Y., Ouyang, T. & Chen, Y. Resonant transport and negative differential resistance in the graphene and graphyne quantum dots. *Phys. B Condens. Matter* **445,** 88–92 (2014).

23. Perrin, M. L. *et al.* Large negative differential conductance in single-molecule break junctions. *Nat. Nanotechnol.* **9,** 830–834 (2014).

24. Samanta, M. P., Tian, W., Datta, S., Henderson, J. I. & Kubiak, C. P. Electronic conduction through organic molecules. *Phys. Rev. B* **53,** R7626–R7629 (1996).

25. Meir, Y. & Wingreen, N. S. Landauer formula for the current through an interacting electron region. *Phys. Rev. Lett.* **68,** 2512–2515 (1992).

26. Jiříček, P. Measurement of the transmission function of the hemispherical energy analyser of ADES 400 electron spectrometer. *Czechoslov. J. Phys.* **44,** 261–267

27. Feit, M. D., Fleck, J. A. & Steiger, A. Solution of the Schrödinger equation by a spectral method. *J. Comput. Phys.* **47,** 412–433 (1982).

28. Brenner, D. W. *et al.* A second-generation reactive empirical bond order (REBO) potential energy expression for hydrocarbons. *J. Phys. Condens. Matter* **14,** 783 (2002).

29. Stokbro, K. *et al.* Semiempirical model for nanoscale device simulations. *Phys. Rev. B* **82,** 075420 (2010).

30. Brandbyge, M., Mozos, J.-L., Ordejón, P., Taylor, J. & Stokbro, K. Density-functional method for nonequilibrium electron transport. *Phys. Rev. B* **65,** 165401 (2002).

31. Fattebert, J.-L. & Bernholc, J. Towards grid-based O(N) density-functional theory methods: Optimized nonorthogonal orbitals and multigrid acceleration. *Phys. Rev. B* **62,** 1713–1722 (2000).

32. Wang, S., Lu, W., Zhao, Q. & Bernholc, J. Resonant coupling and negative differential resistance in metal/ferrocenyl alkanethiolate/STM structures. *Phys. Rev. B* **74,** 195430 (2006).

33. Nardelli, M. B., Fattebert, J.-L. & Bernholc, J. O(N) real-space method for ab initio quantum transport calculations: Application to carbon nanotube-metal contacts. *Phys. Rev. B* **64,** 245423 (2001).

34. Landauer, R. Spatial Variation of Currents and Fields Due to Localized Scatterers in Metallic Conduction. *IBM J. Res. Dev.* **1,** 223–231 (1957).

35. Kumar, R., Dhami, G. S. & Engles, D. Modeling the Charge Transport through Graphene Nano Ribbon (GNR) Between Electrodes of Different Materials. *Int. J. Sci. Eng. Res.* **4,** 2523 (2013).

4. RESONANT TUNNELING BASED GRAPHENE QUANTUM DOT MEMRISTORS

In this chapter, we model two-terminal all graphene quantum dot (GQD) based resistor-type memory devices (memristors). The resistive switching is achieved by resonant electron tunneling. We show that parallel GQDs can be used to create multi-state memory circuits. The number of states can be optimised with additional voltage sources, whilst the noise margin for each state can be controlled by appropriately choosing the branch resistance. A three-terminal GQD device configuration is also studied. The addition of an isolated gate terminal can be used to add further or modify the states of the memory device. The proposed devices provide a promising route towards volatile memory devices utilizing only atomically thin two-dimensional graphene.

4.1. Introduction

Graphene, because of its unique electrical and physical properties such as the extremely high carrier mobility (over 10 $m^2V^{-1}s^{-1}$), has been incorporated into a variety of memory architectures[1–8]. Three types of graphene memories have been demonstrated so far: transistor-type memory[6,9,10], capacitor-type memory[8,11], and resistor-type memory[7,10,12]. Resistor-type memory devices have several advantages over transistor or capacitor-type memory devices[13]. A resistor-type memory stores data based on electrical conductivity states that usually arise from changes in the intrinsic properties of materials, such as: charge transfer, conformational change or reduction-oxidation reaction, in response to an applied voltage or electric field[14–16].

Resistor-type memory devices using graphene are considered as promising candidates for realizing high performance inorganic volatile memories due to their high speed operation, excellent tuneability, and ability for feature size down scaling[8,17]. However, the lack of a bandgap limits the application of graphene in switching devices that require a high on/off current ratio[2,18–22]. Approaches, such as opening the bandgap by introducing a nanogap in the graphene/SiO_2 structure, have been studied, yet a vacuum or nitrogen environment was required for the set process[23].

To eliminate these disadvantages, the graphene quantum dot (GQD) structure has been proposed because it can be used to open a bandgap in graphene, with transport through the GQD achieved by electron resonant tunneling[24,25]. Double-barrier structures reveal interesting properties, including confined states, which makes them candidates for application in multi-level memory cells. Advantages, of multi-level memory cells, include the reduction of size and complexity of integrated circuits (ICs) because less transistors and other IC elements are needed[26,27].

To date, significant research has been on hybrid electronic memory devices in which nanometer-sized graphene, semiconductor nanoparticles or inorganic quantum dots (QDs) are embedded in organic composites[28–32]. In this chapter, a GQD channel-based resistor-type memory is proposed and simulation results showing its memory characteristics are presented. This is the first time an all GQD-based memory has been proposed. The device stores data based on the high and low-conductance response to

an applied voltage using a simple device configuration consisting of graphene nanoribbons as electrodes and a GQD as the active channel material and data storage medium. For multiple-valued memory cells, I-V characteristics with multiple current peaks are needed. By paralleling several GQD devices, multiple current peaks were achieved in a low voltage range, which can be used to construct multiple logic states. We show that the number and noise margin of states are adaptable via controlling external elements such as the load or branch resistance or the applied external voltage. We also proposed a three-terminal GQD-based resistor-type memory with the isolated gate terminal with added system flexibility, making it a desirable candidate for the next-generation high-performance, planar, graphene-based memory devices.

4.2. Theory and Design

The model structure studied here was constructed as follows: in a three-terminal device, a GQD was placed in the middle. The whole system was divided into four parts: the left electrode, the right electrode, the bottom electrode and the scattering central region. The device geometry was optimized such that the maximum interatomic force was smaller than 0.05eV/Å. All edge dangling bonds were passivated with hydrogen atoms. The length and width of the monolayer GQD structure was 5.42nm and 2.63nm respectively. The distance between the GQD and the h-BN layer was equal to 3.3 Å.

The calculations were carried out using the Extended Hückel method with self-consistent field (SCF) iteration as implemented in ATK-SE package[40]. ETH is practicable for this device model, as supported by many published work, principally due to the acceptable electronegativity difference between boron, nitrogen, hydrogen and carbon atoms.[44] The mesh points were defined as uniformly spaced k points of 1×1×50 for all devices, with 50 sample points along the transport direction of the three-terminal structure. The conductance and nonlinear I-V characteristics were studied by the non-equilibrium Green Function (NEGF) method[41,42]. The transmission function was obtained from the Landauer formula:[43]

$$T(E) = Trace[\Gamma_L G \Gamma_R G^+] \tag{4.1}$$

where G and G^+ are the retarded and advanced Green's function of the central scattering region respectively, and $\Gamma_{L,R}$ describes the coupling of left/right electrodes with the central part.

The coherent current through the system is given by the integration of the transmission function over the bias window:

$$I(V) = \frac{q}{h}\int_{\mu_R}^{\mu_L} T(E)[f(E-\mu_L) - f(E-\mu_R)]dE \tag{4.2}$$

where q is the electronic charge, h is the Planck constant, $\mu_{L,R}$ are the electrochemical potentials of the two electrodes, f is the Fermi-Dirac distribution of electrons.

4.3. Results and Discussion

The structure of the two-terminal planar GQD memory device studied here is shown in Fig. 4.1(a). It was formed by etching a trench across the graphene nanoribbon and a U-shaped trench creating a width-4 zigzag GQD in the middle, through which resonant electron tunneling occurs. The tunneling is controlled by a field set by the potential across the two device terminals. A hexagonal boron nitride (h-BN) layer was placed between the dielectric substrate and the graphene structure to decouple the graphene from the dielectric material.

To confirm the programmable memory characteristics of the GQD device, I-V characteristics were simulated under a DC voltage bias sweep (0→0.7→0→-0.2→0V) applied to the left electrode whilst the right electrode was grounded (Fig. 4.1(b)). During the application of a positive voltage sweep from 0 to 0.7V, the set process occurred at around 0.15V, where the cell switched from the high-resistance state (HRS, also known as the insulated OFF state) to the low-resistance state (LRS, also known as the conductive ON state). To bring the cell back to the HRS known as the RESET process, a reversed voltage sweep was applied. From Fig. 4.1(b), we can figure out that the RESET happened at 0.6V. The tunneling effect was prominent especially during the ON state throughout which a pronounced current peak was observed at a low bias: starting from 0V bias, the current initially increased, reaching a maximum of about 30nA at 0.2V, thereafter it sharply decreased.

The suspended GQD device configuration was also studied to determine the key contributing factor for the resistive switching characteristics (see Fig. 4.2). Compared to the h-BN/GQD structure on a silicon dioxide substrate, the suspended device showed similar memory characteristics with its peak current values in both ON and OFF states approximately 1.2 times as large. This similarity indicates that the GQD layer, rather than the h-BN, has the greatest impact on the device memory characteristics.

The non-linear I-V characteristics make the device suitable in constructing an inverter circuit with hysteresis which can be used as a static memory element with a greatly reduced number of electronic elements compared to conventional circuits[33,34]. Multi-state memory operation is possible if multiple current peaks are achieved, which can be attained by integrating multiple GQD devices in parallel (see Fig. 4.3(a)). The voltage across each GQD module can be modified by varying the series resistance, shifting the peak voltage of the module with respect to others. The I-V curve of the circuit exhibits as many current peaks as the number of GQD modules connected in parallel. This is a consequence of the superposition of current through each module and is shown in Fig. 4.3(b). Steady-state solutions are available at intersections of I-V characteristics for GQD devices $I=I_G(V)$ and the load line $I=I_L(V)$. Fig. 4.3(b) illustrates five such intersections whose stability can be examined by the following equation[35]:

$$V_{out} = Aexp\left\{-\frac{1}{C_G}\left(\frac{1}{R_L}+\frac{1}{R_i}\right)t\right\} + \frac{R_L R_i}{R_L + R_i}\left(\frac{V_{in}}{R_L} - I_i\right) \tag{4.3}$$

where V_{out} is the output voltage, V_{in} is the input voltage, A is a constant, R_i is the differential resistance of the GQD branch at intersection *i* (*i*=1,2,3,4,5), I_i is the current axis intersect of each piecewise function of $I=I_G(V)$, C_G is the equivalent capacitance of all GQDs, t is time and R_L is the load resistance.

The stability of each intersection is determined by the sign of the exponent $1/R_L + 1/R_i$. For large t the exponential function approaches to zero and the output voltage is stable if the sign is positive, whereas the exponential function approaches to infinity if the sign is negative. In the latter case, any small change in voltage or current around the steady-state point increases exponentially with time, the point is therefore unstable. In the case of Fig. 4.3(b), the labelled intersections 1, 3, 5 correspond to stable solutions,

whilst 2 and 4 are unstable ones. By changing the states, between these three stable points, high, middle or low, this circuit can function as a static memory.

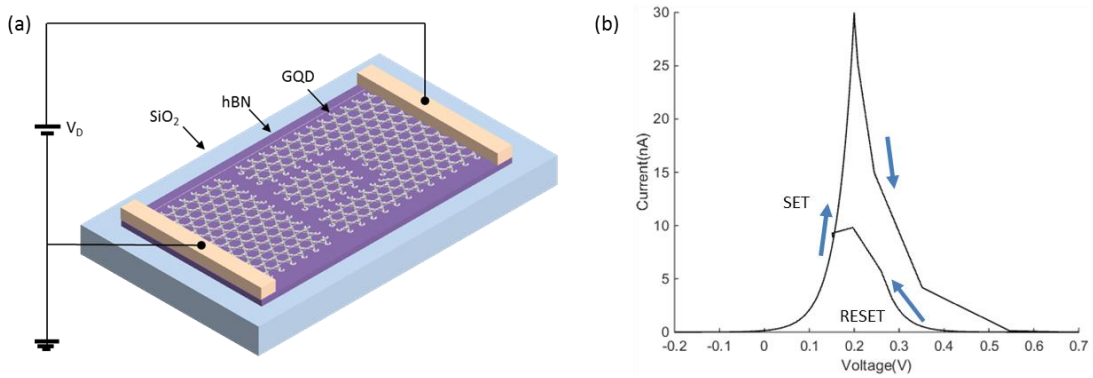

Figure 4.1 (a) The schematic and circuit diagram of the GQD resistive switching memory device. (b) The simulated I-V characteristics of the structure.

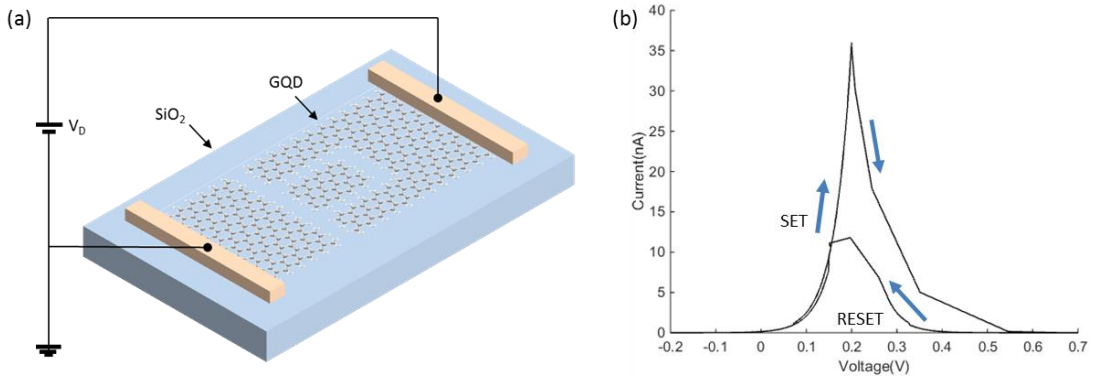

Figure 4.2 (a) The schematic and circuit diagram of the suspended GQD resistive switching memory device. (b) The simulated I-V characteristics of the structure.

The operation of the static memory is as follows. In the circuit shown in Fig. 4.3(a), if V_{in} increases from zero, V_{out} changes along the first rising part of $I_G(V)$, from zero through point 1 until it reaches the first peak voltage V_{p1}. Then, with a further increase in V_{in}, the output voltage jumps, or switches, to the second rising part of $I_G(V)$, changing all the way through point 3 to the second peak voltage V_{p2} which leads to the second voltage jump. When V_{in} decreases after the voltage jump, V_{out} decreases on a different line, through point 3 until it reaches V_v. A further decrease in V_{in} causes another step change in V_{out}, this time to the first rising part of $I_G(V)$. Therefore, plotting the output voltage, as a function of the source voltage, results in the characteristics shown in Fig. 4.3(c). The output voltage shows hysteresis whose width, in terms of V_{in}, determines the noise margin of the memory for the change in the supply voltage. Reading the state

of the memory cell is achieved by sensing the voltage at the output node. Writing information to the memory cell can be performed either by directly pulling the output node voltage up or down or by varying the input voltage.

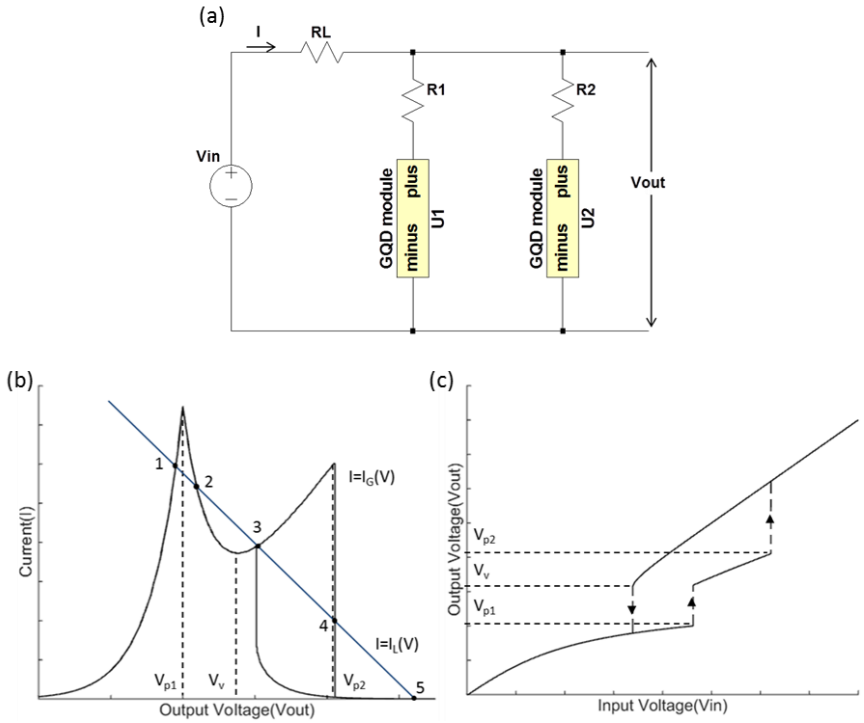

Figure 4.3 (a) The schematic of the multi-state GQD memory circuit setup. Two GQD modules are connected in parallel. The resistors R_1 and R_2 provide different biasing of the modules at the same source voltage V_{in}. The resistor R_L defines the load line for the device. (b) Piecewise modelling of the I-V characteristics for two parallel GQDs and a load line. With the resistors R_1 and R_2, the ground-state resonance is split up into two peaks. The operation points 1, 3, and 5 represent the logic levels low, middle, and high, respectively. (c) Input-output characteristic of the circuit.

Key parameters for the memory operation, such as the position, number, and noise margin of logic levels, can be controlled by external bias voltages or series resistances. Therefore, a circuit with desirable characteristics can be designed. The load resistance R_L affects the total hysteresis which can be seen in the comparisons shown in Fig. 4.4(a-c), whilst branch resistances R_1 and R_2 determine the position of the first and second logic switch locations respectively, with the noise margin of the unique middle state depending on the location of the two logic switch locations (Fig. 4.4(d-f)). In the circuit shown in Fig. 4.4(II), if a pulse with sufficient magnitude (here a rectangular pulse was applied with 10ns duration and 0.25V amplitude) is applied around the first state

switching point, it is possible that the logic level can change directly from low to high without passing through the middle state, resulting in the corresponding characteristic shown in Fig. 4.4(g).

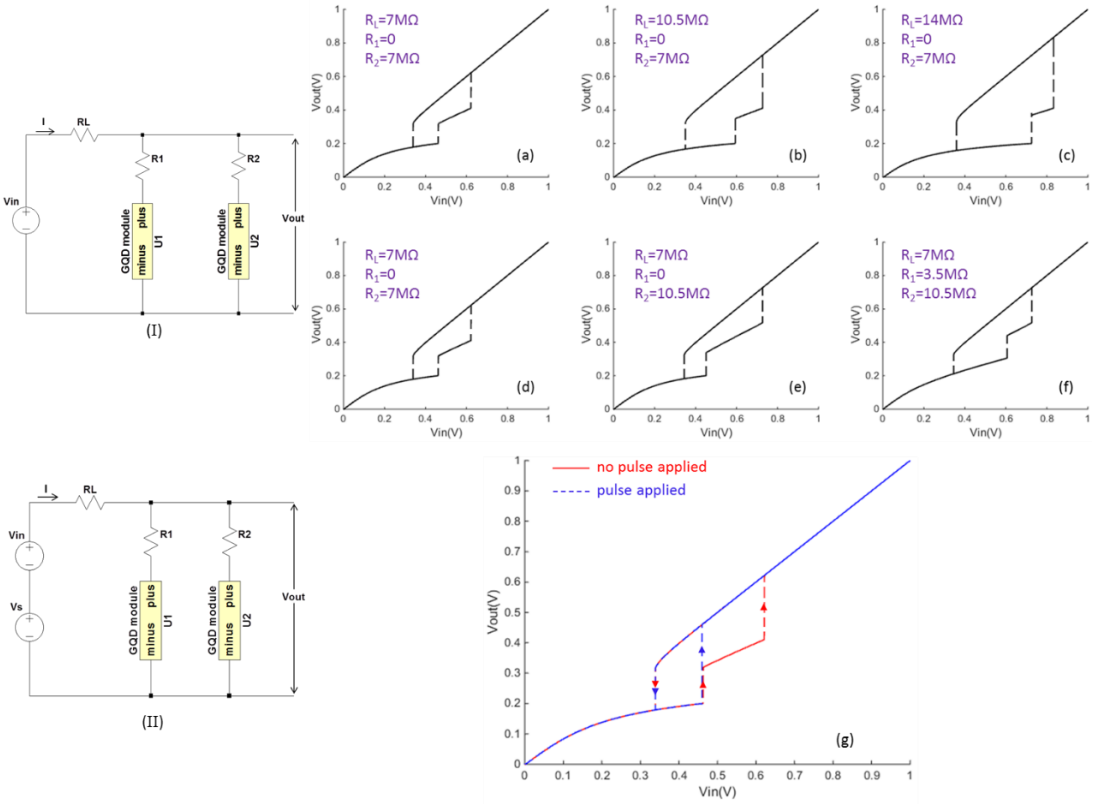

Figure 4.4 Demonstration of memory operation under different conditions. (I) Schematic of the same memory circuit setup shown in Fig. 4.3(a). (a-f) Calculated input-output characteristics of the memory cell shown in Fig. 4.4(I) with corresponding R_L, R_1, and R_2 values. (II) Schematic of the memory circuit setup with an additional pulse voltage. (g) Comparison of input-output characteristics of the memory cell shown in Fig. 4.4(II) under the no-pulse-applied (solid red) and the pulse-applied (dash blue) cases.

Fig. 4.5 offers more details regarding the pulse. Voltage pulses with positive and negative polarity were applied to the left electrode during SET and RESET respectively. Both SET and RESET require higher pulse voltage amplitudes for shorter pulse durations, while the SET process has a higher speed when compared to the RESET. Here we extend the definition of SET/RESET to the switch from the highest/lowest resistance state to the lowest/highest resistance state. The characteristics of the SET and RESET process are attributed to the energy required for the resonant electron tunneling. The energy gained/lost by electrons at the SET/RESET point can be expressed by[36]:

$$E = QV = \frac{V^2}{R}t \tag{4.4}$$

where E is the electric energy, Q is the electric charge, V is the pulse voltage, R is the resistance, t is the pulse duration or charging time.

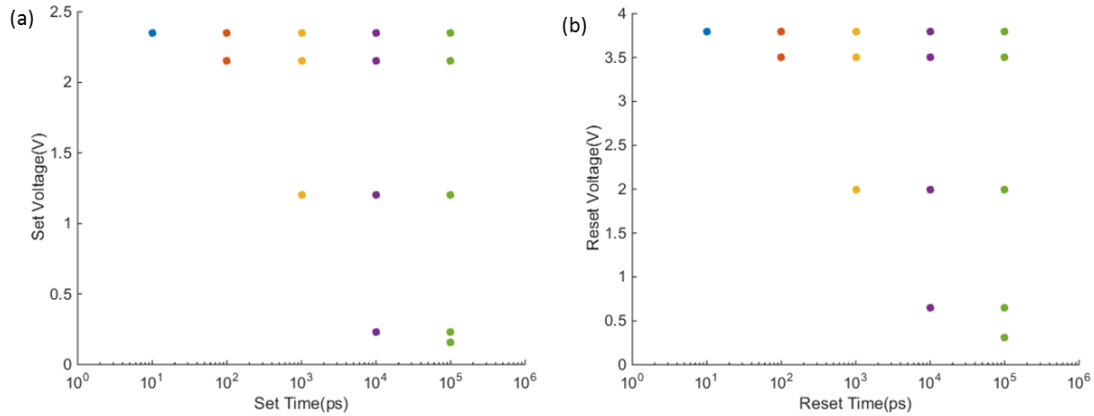

Figure 4.5 Dependence of SET and RESET pulse voltage amplitudes on pulse durations. The voltage amplitude was plotted as a function of time width of pulses able to SET (a) and RESET (b) a GQD memory cell.

During SET/RESET, a certain amount of energy is offered to/taken from electrons by the applied pulse, therefore electrons are able/unable to tunnel through the energy gap, resulting in the switch between the highest and lowest resistance states. The similarity observed in both SET and RESET can be explained by the inversely proportional relationship between the charging voltage and the charging time, as shown in formula (4.2). The difference is attributed to the larger energy gap on the RESET point (in our case, 0.11eV and 0.35eV at the SET and RESET point respectively), which means under the same pulse voltage amplitude, more charge or longer charging time is needed to decrease the energy of electrons to disable the resonant tunneling. The pulse duration also reflects that the GQD memory device is anticipated to have a higher switching speed than other material-based memory devices published so far (see Table 4.1).

Based on the described principle, memory cells with additional logic levels can be made by paralleling more GQD modules. However, the increase of parallel branches leads to the increase of series resistors, which impairs the compactness and miniaturization of the circuit. A viable solution is to add an isolated gate terminal to the GQD device. The I-V characteristic of the device can be tuned non-linearly by the applied gate potential,

which not only surpasses the linear function of pure series resistors but also greatly strengthens the flexibility of the circuit. Fig. 4.6 presents the structure of the three-terminal GQD device studied here and distinguishable I-V characteristics achieved under different gate voltages. Resonant electron tunneling appears both in the positive and negative voltage range.

Table 4.1 Comparison of different material-based memory concepts

Structures	Switching mechanism	Switching speed	Type	Testing condition
Graphene/SiO_2 nanogap[23]	Redox reaction in the breakdown region of SiO_2	500ns	Nonvolatile	Experiment
Oxygenated carbon[37]	Electrochemical redox reaction of carbon	≈10ns	Nonvolatile	Experiment
Graphene oxide (GO)[5]	Charge transfer between GO and thionine	<5ns	Nonvolatile	Experiment
Graphene/PMMA nanocomposite[38]	Electron-trapping and electric-screen effect of graphene	Not available	Volatile	Experiment
Graphene nanoribbon (GN) crossbar[39]	Charge transfer in GN multi-layers	<30ps	Volatile	Simulation
GQD (this work)	Resonant electron tunneling	≈10ps	Volatile	Simulation

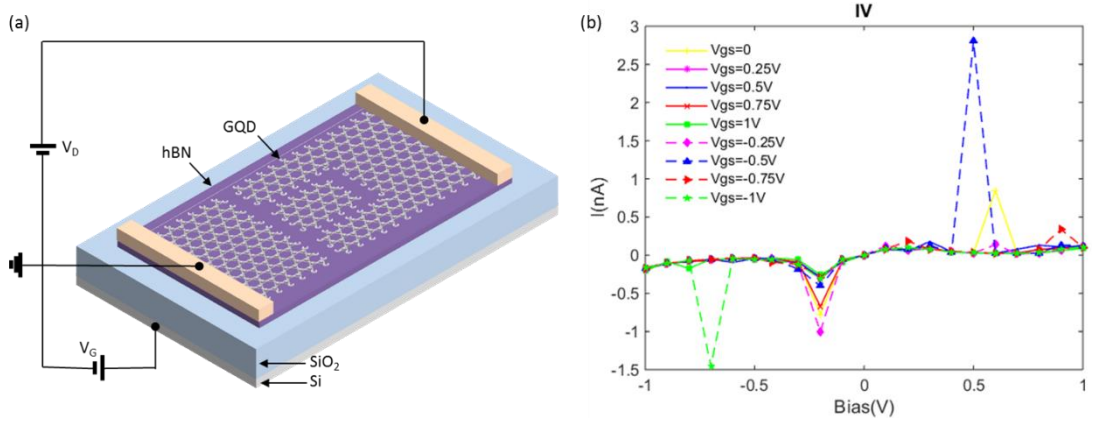

Figure 4.6 (a) The schematic and circuit diagram of the three-terminal GQD resistive switching memory device. (b) The calculated I-V curves with different gate applied voltages.

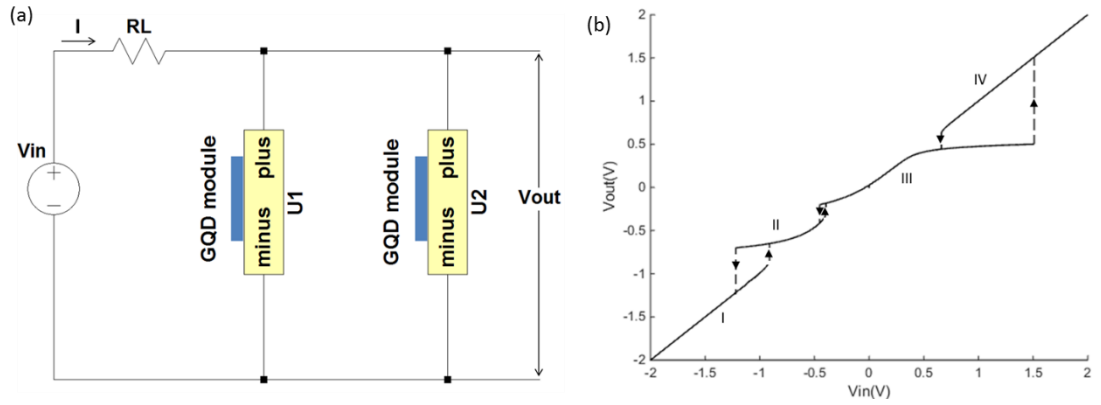

Figure 4.7 (a) The schematic of the three-terminal GQD memory circuit setup. The blue area represents the isolated gate. (b) Input-output characteristic of the circuit. I, II, III, and IV represent four different logic levels respectively.

Paralleling this three-terminal GQD device can generate new memory characteristics. Comparing to the resistor and two-dimensional GQD serial connection model where only the position of the current peak can be adjusted, the three-terminal module offers modification in the number of peaks and magnitude as well. This feature makes possible increased logic states with reduced number of GQD modules. In the circuit shown in Fig. 4.7(a), two GQD modules were selected, working under -0.5V and -1V gate-to-source potential respectively. When V_{in} was swept from -2V to 2V, four logic states were identified as shown in Fig. 4.7(b). The number, position and noise margin of logic states correspond to the number, position and magnitude of current peaks separately. By applying different voltages on each gate, various states can be realized on a single memory cell.

4.4. Conclusion

In summary, in this chapter we have demonstrated resistor-type memories using GQD as the resistive switching element. The resistive switching was achieved by resonant electron tunneling under the influence of an electric field. Memory circuits showed different hysteresis characteristics, depending on the I-V characteristic of the GQD and the values of branch resistors and the load resistance. The three-terminal GQD device was further designed to largely increase the tuneability of the memory cell without affecting the simplicity of the whole system. It is important to note that introducing the isolated gate terminal increases the number of logic states that can be achieved by one memory cell. Because of unique electronic properties and the memory being comprised

of a single material (graphene), the GQD memory, proposed here, has great potential to be used to construct memory devices on all graphene-based processes and circuits.

References

1. Hsu, J.-C., Liu, C.-L., Chen, W.-C., Sugiyama, K. & Hirao, A. A Supramolecular Approach on Using Poly(fluorenylstyrene)-block-poly(2-vinylpyridine):PCBM Composite Thin Films for Non-Volatile Memory Device Applications. *Macromol. Rapid Commun.* **32,** 528–533 (2011).
2. Liu, J. *et al.* Bulk Heterojunction Polymer Memory Devices with Reduced Graphene Oxide as Electrodes. *ACS Nano* **4,** 3987–3992 (2010).
3. Lian, S.-L., Liu, C.-L. & Chen, W.-C. Conjugated Fluorene Based Rod–Coil Block Copolymers and Their PCBM Composites for Resistive Memory Switching Devices. *ACS Appl. Mater. Interfaces* **3,** 4504–4511 (2011).
4. Gao, S., Song, C., Chen, C., Zeng, F. & Pan, F. Dynamic Processes of Resistive Switching in Metallic Filament-Based Organic Memory Devices. *J. Phys. Chem. C* **116,** 17955–17959 (2012).
5. Chen, C.-J., Hu, Y.-C. & Liou, G.-S. Electrically bistable memory devices based on poly(triphenylamine)–PCBM hybrids. *Chem. Commun.* **49,** 2804–2806 (2013).
6. Sup Choi, M. *et al.* Controlled charge trapping by molybdenum disulphide and graphene in ultrathin heterostructured memory devices. *Nat. Commun.* **4,** 1624 (2013).
7. Jeong, H. Y. *et al.* Graphene Oxide Thin Films for Flexible Nonvolatile Memory Applications. *Nano Lett.* **10,** 4381–4386 (2010).
8. Hong, A. J. *et al.* Graphene Flash Memory. *ACS Nano* **5,** 7812–7817 (2011).
9. Lee, S. *et al.* Impact of gate work-function on memory characteristics in Al2O3/HfOx/Al2O3/graphene charge-trap memory devices. *Appl. Phys. Lett.* **100,** 023109 (2012).
10. Ji, Y. *et al.* Organic nonvolatile memory devices with charge trapping multilayer graphene film. *Nanotechnology* **23,** 105202 (2012).
11. Yang, R. *et al.* Isolated nanographene crystals for nano-floating gate in charge trapping memory. *Sci. Rep.* **3,** (2013).
12. Liu, J. *et al.* Fabrication of Flexible, All-Reduced Graphene Oxide Non-Volatile Memory Devices. *Adv. Mater.* **25,** 233–238 (2013).

13. Zhang, B., Chen, Y., Neoh, K.-G. & Kang, E.-T. CHAPTER 1:Organic Electronic Memory Devices. in *CHAPTER 1:Organic Electronic Memory Devices* 1–53 (2015).
14. Chua, L. O. & Tseng, C.-W. A memristive circuit model for p-n junction diodes. *Int. J. Circuit Theory Appl.* **2,** 367–389 (1974).
15. Kondo, J., Lingalugari, M., Chan, P.-Y., Heller, E. & Jain, F. Quantum Dot Channel (QDC) Field Effect Transistors (FETs) and Floating Gate Nonvolatile Memory Cells. *J. Electron. Mater.* **44,** 3188–3193 (2015).
16. Li, D. *et al.* Nonvolatile Floating-Gate Memories Based on Stacked Black Phosphorus–Boron Nitride–MoS2 Heterostructures. *Adv. Funct. Mater.* **25,** 7360–7365 (2015).
17. Novikov, Y. N., Gritsenko, V. A., Krasnikov, G. Y. & Orlov, O. M. Multilayer graphene-based flash memory. *Russ. Microelectron.* **45,** 63–67 (2016).
18. Schwierz, F. Graphene transistors. *Nat. Nanotechnol.* **5,** 487–496 (2010).
19. Wu, Y. *et al.* High-frequency, scaled graphene transistors on diamond-like carbon. *Nature* **472,** 74–78 (2011).
20. Lee, D. *et al.* Black phosphorus nonvolatile transistor memory. *Nanoscale* **8,** 9107–9112 (2016).
21. Guttinger, J. graphene quantum dots. (2011).
22. Bacon, M., Bradley, S. J. & Nann, T. Graphene Quantum Dots. *Part. Part. Syst. Charact.* **31,** 415–428 (2014).
23. He, C. *et al.* Multilevel Resistive Switching in Planar Graphene/SiO2 Nanogap Structures. *ACS Nano* **6,** 4214–4221 (2012).
24. Chang, L. L., Esaki, L. & Tsu, R. Resonant tunneling in semiconductor double barriers. *Appl. Phys. Lett.* **24,** 593–595 (1974).
25. Soderstrom, J. & Andersson, T. G. A multiple-state memory cell based on the resonant tunneling diode. *IEEE Electron Device Lett.* **9,** 200–202 (1988).
26. Liu, H. C. & Coon, D. D. Heterojunction double-barrier diodes for logic applications. *Appl. Phys. Lett.* **50,** 1246–1248 (1987).
27. Capasso, F., Mohammed, K. & Cho, A. Resonant tunneling through double barriers, perpendicular quantum transport phenomena in superlattices, and their device applications. *IEEE J. Quantum Electron.* **22,** 1853–1869 (1986).
28. Lee, J.-S. Review paper: Nano-floating gate memory devices. *Electron. Mater. Lett.* **7,** 175 (2011).

29. Kang, M., Baeg, K.-J., Khim, D., Noh, Y.-Y. & Kim, D.-Y. Printed, Flexible, Organic Nano-Floating-Gate Memory: Effects of Metal Nanoparticles and Blocking Dielectrics on Memory Characteristics. *Adv. Funct. Mater.* **23,** 3503–3512 (2013).
30. White, S. I., Vora, P. M., Kikkawa, J. M. & Winey, K. I. Resistive Switching in Bulk Silver Nanowire–Polystyrene Composites. *Adv. Funct. Mater.* **21,** 233–240 (2011).
31. Zhang, Q., Pan, J., Yi, X., Li, L. & Shang, S. Nonvolatile memory devices based on electrical conductance tuning in poly(N-vinylcarbazole)–graphene composites. *Org. Electron.* **13,** 1289–1295 (2012).
32. Wu, C., Li, F., Guo, T. & Kim, T. W. Controlling memory effects of three-layer structured hybrid bistable devices based on graphene sheets sandwiched between two laminated polymer layers. *Org. Electron.* **13,** 178–183 (2012).
33. Chen, K. J., Akeyoshi, T. & Maezawa, K. Monolithic integration of resonant tunneling diodes and FET's for monostable-bistable transition logic elements (MOBILE's). *IEEE Electron Device Lett.* **16,** 70–73 (1995).
34. Lehovec, K. GaAs enhancement mode FET-tunnel diode ultra-fast low power inverter and memory cell. *IEEE J. Solid-State Circuits* **14,** 797–800 (1979).
35. Mizuta, H. & Tanoue, T. *The Physics and Applications of Resonant Tunnelling Diodes*. (Cambridge University Press, 2006).
36. Luryi, S. Quantum capacitance devices. *Appl. Phys. Lett.* **52,** 501–503 (1988).
37. Santini, C. A. *et al.* Oxygenated amorphous carbon for resistive memory applications. *Nat. Commun.* **6,** 8600 (2015).
38. Wu, C., Li, F. & Guo, T. Formation and carrier transport properties of single-layer graphene/poly (methyl methacrylate) nanocomposite for resistive memory application. *Vacuum* **101,** 246–249 (2014).
39. Khasanvis, S., Habib, K. M. M., Rahman, M., Lake, R. & Moritz, C. A. Low-Power Heterogeneous Graphene Nanoribbon-CMOS Multistate Volatile Memory Circuit. *J Emerg Technol Comput Syst* **12,** 15:1–15:18 (2015).
40. Stokbro, K. *et al.* Semiempirical model for nanoscale device simulations. *Phys. Rev. B* **82,** 075420 (2010).
41. Brandbyge, M., Mozos, J.-L., Ordejón, P., Taylor, J. & Stokbro, K. Density-functional method for nonequilibrium electron transport. *Phys. Rev. B* **65,** 165401 (2002).

42. Fattebert, J.-L. & Bernholc, J. Towards grid-based O(N) density-functional theory methods: Optimized nonorthogonal orbitals and multigrid acceleration. *Phys. Rev. B* **62,** 1713–1722 (2000).

43. Landauer, R. Spatial Variation of Currents and Fields Due to Localized Scatterers in Metallic Conduction. *IBM J. Res. Dev.* **1,** 223–231 (1957).

44. Pauling, L., The Nature of the Chemical Bond, Third Edition, Cornell University Press, Ithaca, New York, 1960.

5. DIRECT GROWTH OF PATTERNED GRAPHENE ON WAFER SCALE

In this chapter, based on the aforementioned GQD model, a fabrication proposal is put forward with each step being explained in detail. Experimental results for partial steps are demonstrated, including the successful direct growth of graphene thin-films on an ultra-nanocrystalline diamond (UNCD) wafer. The good quality of produced graphene is well-supported by the Raman spectroscopy. For uncompleted steps, discussions analysing existing results and suggestions for future work are presented. The fabrication process is described, which can open up a promising route for mass production of GQD structures and contribute to the further advances in the nanoelectronic field.

5.1. Introduction

Due to its exceptional properties in electronics, mechanics, optics and so forth, graphene and its derivatives are continuously attracting attentions in numerous fields, among which the wafer-scale fabrication raises plenty of interest[1–3]. Realization of this type of fabrication is believed to be dependent on an approach which enables the direct growth of large-scale patterned graphene layers on dielectric substrates. According to research work reported so far, methods have been provided on growing high-quality single- or multi-layered graphene on the surface of silicon dioxide (SiO_2)[4], silicon carbide (SiC)[5–8,4], hexagonal boron nitride (h-BN)[9,10], and even germanium (Ge)[11,12].

Recent studies reveal the possibility of diamond being regarded as a promising candidate for supporting substrates because of its unique material properties as shown in Table 5.1[13–22]. Compared to many other substrates, advantages offered by diamond include low energy dissipation, low trap density, high acoustic velocity, linear electromechanical effect, *etc*[23]. Besides, due to the progress in film fabrication, high-quality diamond has been able to grow uniformly on large-area substrates and can be easily integrated with other materials to realize extra functionality required or build ultra-complicated systems. Exfoliated graphene has been reported to be transferred onto the surface of diamond-like carbon (DLC) and synthetic diamond, and the ultimate electronic devices turn out to have improved characteristics, for instance, a better radio-frequency (RF) performance[24]. However, the amorphous diamond-like carbon, because of certain native defects, is comparatively less widely-used than the crystalline diamond. For example, the thermal conductivity of DLC at 300K is barely 0.2-3.5 W/m·K, indicating a low heat transfer rate in the material and probably resulting in an unfavourable heat accumulation. Therefore, in consideration of the intrinsic properties, the electrical performances as well as the mechanical compatibility with modern semiconductor technologies, synthetic diamond is accepted as a more viable alternative to replace conventional substrate materials in graphene-related devices. In fact, the diamond has been demonstrated to act as an exceptional platform for graphene-based structures, since due to its superb thermal conductivity the breakdown current density of devices can reach $10^9 A/cm^2$. Despite the enormous benefit mentioned above, several

fabrication challenges need to be taken to practically realize the selective growth of graphene on diamond.

Table 5.1 Comparison of physical and mechanical properties at 300K between Si, SiO_2, SiC, h-BN and diamond

Property	Si	SiO_2	SiC	h-BN	Diamond
Lattice Constant(Å)	5.43	-	3.09	2.50	3.57
Cohesive Energy(eV/atom)	4.64	12.94	6.34	6.65	7.36
Young's Modulus (GPa)	130	70	450	800	1,200
Electron mobility($cm^2/V{\cdot}s$)	≤1,400	20±3	≤900	≤930	≤1,000
Thermal conductivity(W/m·K)	149	1.1-1.4	360-490	1,700-2,000	2005

Based on published research work, epitaxial graphene layers have been grown on diamond with transition metals being catalysts. Garcia *et al.*[25] demonstrated the role of nickel (Ni) as a strong catalyst to promote the segregation of carbon atoms from the single-crystalline diamond (SCD) into the transition metal. In the process, carbon atoms were firstly dissolved and diffused, and then recombined in the form of graphene on the top surface. Cooil *et al.*[26] showed an iron-mediated catalytic approach for producing graphene films on the surface of carbon-rich substrates including diamond. Wu *et al.*[30], based on the surface-mediated mechanism, presented a process of growing graphene sheets epitaxially on the copper substrate with the graphene orientation being well controlled. The good quality of produced graphene was revealed by different types of spectroscopy in each study. However, further improvement can still be made. Instead of choosing diamond (001), diamond (111) can offer better performances as its lattice parameters are highly-matched with those of graphene. In addition, polycrystalline diamond, rather than SLD, can be used because it reduces the cost without negatively affecting the quality of resulting films.

In this chapter, a process for patterned graphene synthesis is discussed. The pattern is on the basis of the simulated model presented in the previous two chapters. The overall fabrication procedure is mainly dependent on the EBL patterning of channels and electrodes, as well as the rapid thermal annealing of an ultra-nanocrystalline (UNCD) substrate with the metal Ni film being the catalyst which is deposited by PVD. Due to the direct growth method, transfer processes are avoided, which decreases the risk of

causing damages to the GQD structure. Raman spectroscopy is applied to examine the quality of produced graphene layers. Even though the EBL step has not been completed, existing results are illustrated, and possible solutions are proposed for future work. Generally speaking, the fabrication process demonstrated in this chapter provides a path to produce high-performance GQD-based devices.

5.2. Results and Discussion

The schematic of the whole fabrication process for the fundamental two-terminal GQD structure studied previously is shown in Fig. 5.1. The commercial UNCD substrate consists of a.300um-thick Si layer, a 1um-thick dielectric layer, and a 1um-thick non-conductive UNCD layer. The grain size of the UNCD is only around 2-5nm, which indicates a large grain boundary (GB) volume fraction. EBL defines the deposition position of Ni on the diamond surface. After RTA, graphene grows exclusively on the Ni-covered area. More experimental details are presented in the following sub-sections.

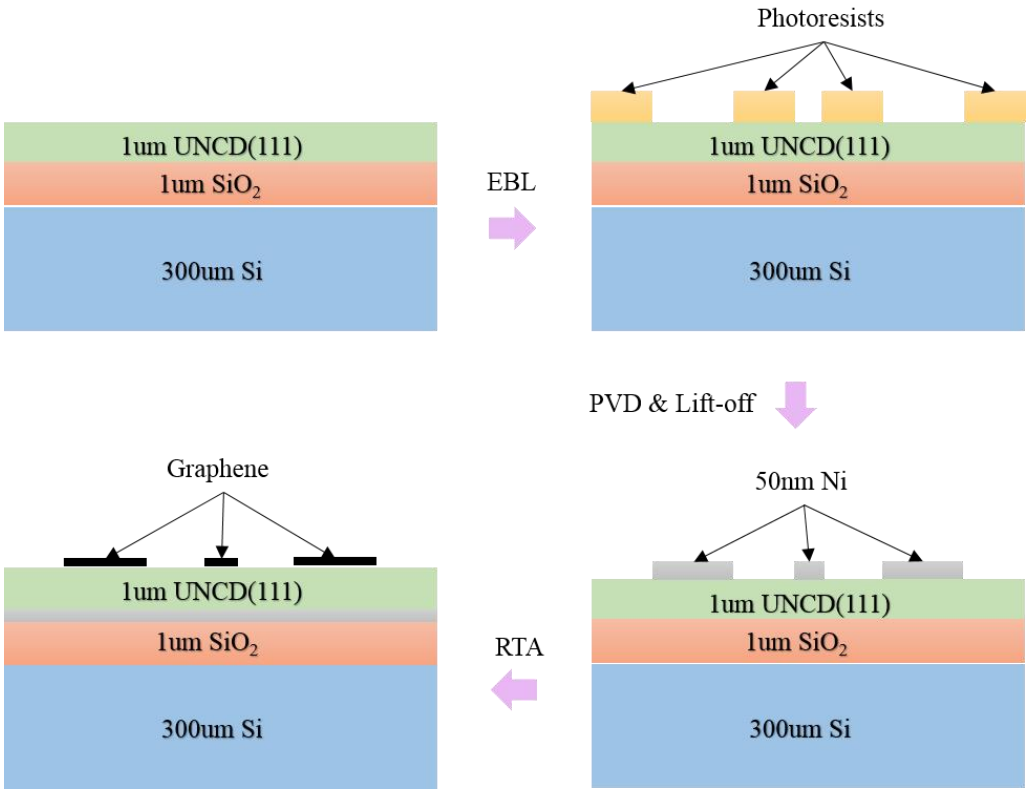

Figure 5.1 The schematic illustration of the GQD structure fabrication process.

5.2.1. Non-pattern Growth of Graphene Layers on UNCD

To verify the carbon segregation induced by RTA, the direct growth of non-patterned graphene is first conducted. The UNCD sample was cleaned in a standard preparation procedure: sonicating in acetone for 5 mins, rinsing in isopropanol (IPA), rinsing in deionized water (DI water), blowing dry under nitrogen. The Ni deposition is then executed using the e-beam evaporator system (PVD 75 – Kurt J. Lesker). When the deposition chamber was evacuated to 1.6×10^{-7}Torr, known as the base pressure, electrons from the beam source started hitting the evaporation material. The deposition rate was set to be 1Å/s. Once deposition completed, the sample was left in the vacuum chamber for at least 30 mins to cool down for the purpose of preventing oxidation or other contaminations. The thickness of deposited Ni film is confirmed by

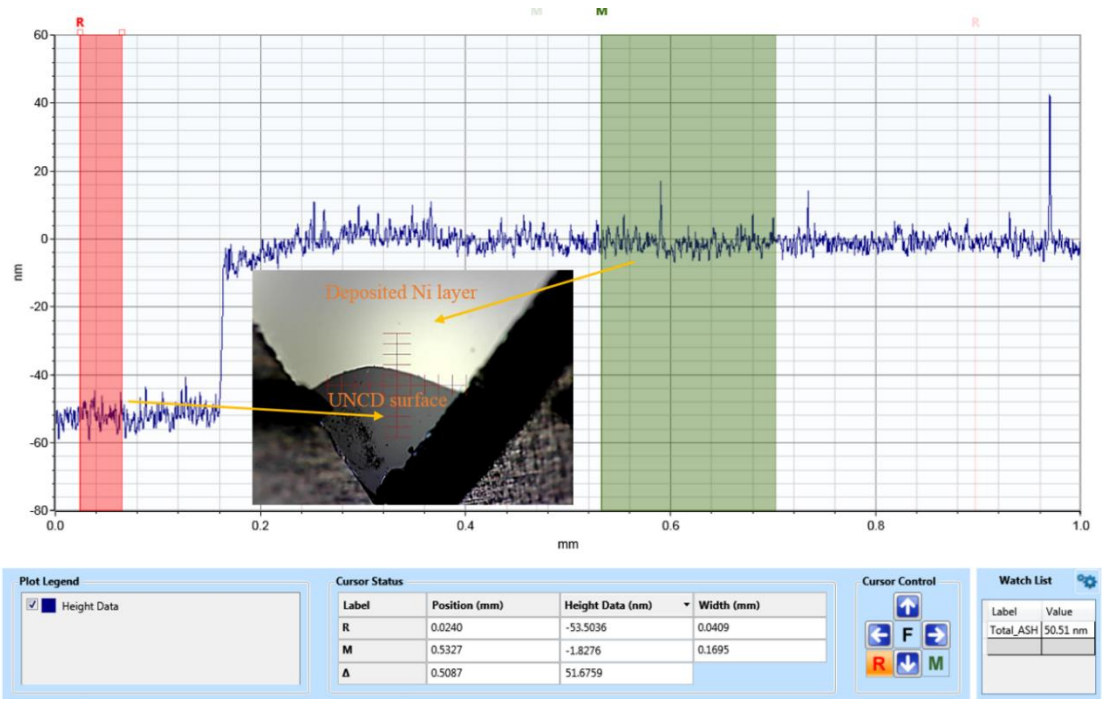

Figure 5.2 The data analysis window displayed in the software after the scan. Inset, the optical image of the scanned sample corner. The positions of the R and M cursors on the scan show locations of the measurement. To achieve a more accurate expression of the height difference, both height values for the Ni-covered and Ni-free areas are averaged over certain range, as indicated by the width of the two cursors. In the inset, the superimposed cross-hair target denotes the starting point of the scan. During the scan, the displacement direction of the sample is downward.

using a stylus profiling system (Bruker Instruments, DektakXT Stylus Profiler). Fig. 5.2 displays the software data analysis window. 52±2.6nm (5% deviation) turned out to be the measured height difference which is in conformity with the expected value.

Furthermore, the X-ray powder diffraction (XRD) was applied for the crystal phase identification by using the wide-angle XRD system (Bruker: D4 Endeavor & Bruker: Diffrac EVA V4.2 software). The fundamental principle of XRD is closely related to the Bragg's law which is schematically represented in Fig. 5.3. When incident X-rays strike a crystalline plane and interact with the sample, corresponding diffracted X-rays are produced, resulting in the constructive interference. The Bragg's law reveals the relationship between the lattice parameter and the X-ray property, and can be expressed as[27]:

$$n\lambda = dsin\theta \tag{5.1}$$

where n represents a positive integer, λ and θ refer to the wavelength and the incident angle of the incident X-ray respectively, d is the lattice spacing between planes. As the lattice spacing (d) is an intrinsic parameter and is unique for each material, the sample composition can be detected by processing information contained in the diffracted rays. Fig. 5.4 illustrates the phase constitution for the deposited sample, in which a broad range of peaks are involved.

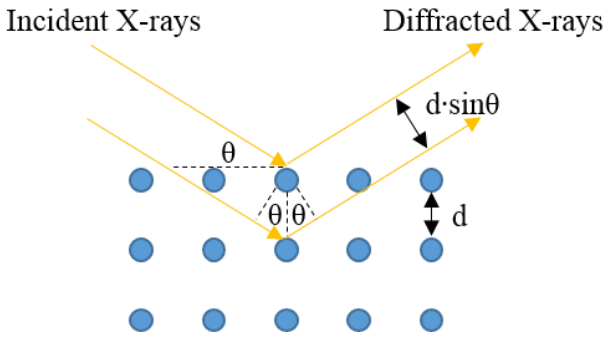

Figure 5.3 The schematic illustration of the Bragg's law.

The fact that Ni (111) predominates the crystal orientation of the evaporated film reflects the impact of UNCD lattice properties on the film growth. The existence of minor crystalline peaks (such as Ni (200)) and other amorphous ones is attributed to the impurity of the substrate.

The RTA process (Fig. 5.5(a) and (b)) is finally carried out to produce graphene films by using the 1100 Quartz Tube Furnace system. The furnace chamber was pre-heated 800°C, while the sample stayed in the Ni-only tube where the temperature is much lower. The forming gas (4.08% H_2, Ar balance) was continuously purged with the flowing rate being 0.5 s.c.c.m. When the base pressure goes down to nearly 10 Torr, the sample started being shifted into the chamber through the entrance and kept in the

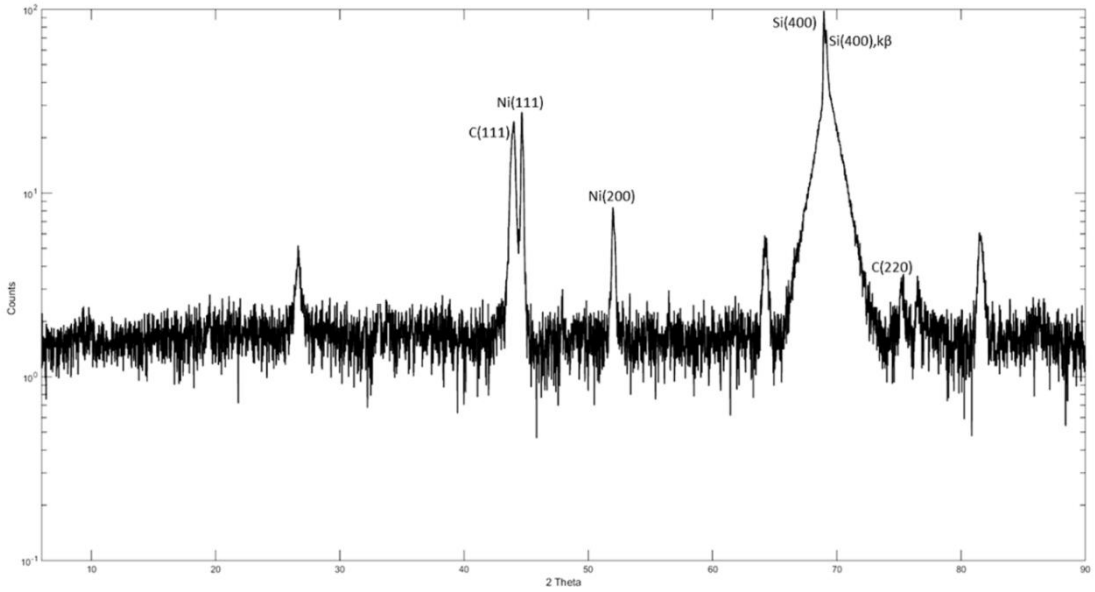

Figure 5.4 The XRD analysis of the Ni-deposited UNCD (111) substrate. "C" refers to the carbon element in the UNCD.

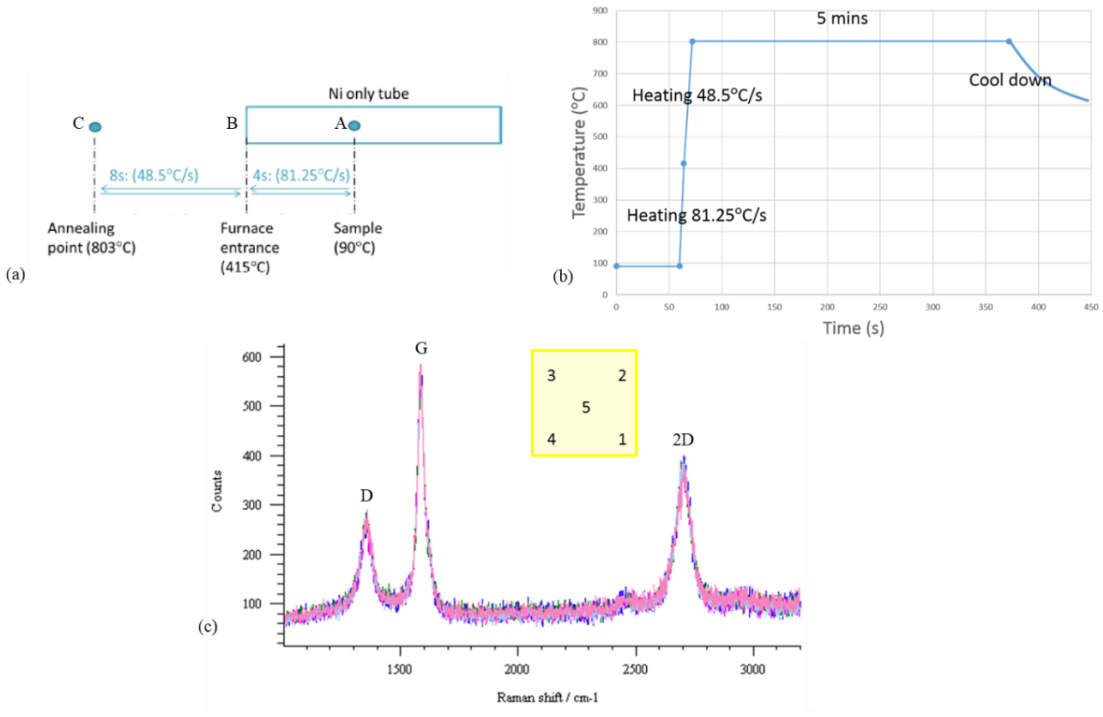

Figure 5.5 Growth of graphene on UNCD. (a) The schema of the RTA process. Position A and C denotes the location of the sample in the tube and chamber respectively, whilst position B is the chamber entrance. Temperatures in the three points are monitored and controlled. The sample moves forward from A to C to be annealed and backward passing position A to the end of the tube to be cooled down. (b) Recipe for the thermal annealing process illustrates the rapid heating of the sample whose temperature goes up to 803°C and was maintained in the high level for 5mins before naturally dropping down. (c) The Raman spectroscopy analysis of the sample. Inset, a symbolic diagram of the sample (5mm×5mm) top view with five Raman test points presented.

high-temperature environment for 5mins. During the thermal annealing, since the diffusion rate of Ni atoms is higher through the UNCD GBs than through the grains, most atoms ultimately spread out to the UNCD/SiO_2 interface, leaving only a few on the UNCD surface. The remaining Ni islands then serve as nucleation centres and catalyse the graphene epitaxial growth, even though in the end diffusion is still inevitable for the small amounts of Ni residue. Besides, the growth of graphene over the whole wafer area is also attributed to the constant supply of carbon atoms counter-diffusing from the UNCD layer to the top. Characteristics of the produced graphene films are revealed via Raman spectroscopy (Renishaw Instrument, inVia^{TM} confocal Raman microscope).

As is shown in Fig. 5.5(c), a uniform graphene coverage has been achieved in the wafer scale, which is supported by the fact that Raman spectrums at different test points almost coincide. The ratio of peak 2D (at around 2700cm^{-1}) to peak G (at around 1600cm^{-1}) indicates the multilayer structure of the film, whilst the value of peak D (at around 1335cm^{-1}) denotes the existence of certain defects, for instance folds and wrinkles.

5.2.2. Pattern Growth of Graphene Layers on UNCD

To realize the pattern growth of graphene layers, the EBL process is indispensable (see Fig. 5.1) and generally consists of fixed steps including the pattern design, the sample preparation, machine calibration, exposure, development, and lift-off. Fig. 5.6 schematically illustrate the general EBL process, in which the photoresist is assumed to be positive.

Firstly, the pattern to be exposed was designed by using the KLayout Editor and exported in the common GDS format. The GDS data were then translated into a GPF file by using the Layout Beamer – a propriety Vistec EBPG software, and therefore can be read by the EBL system (Vistec Instrument, EBPG 5000plusES). All necessary instructions required by the pattern generator are involved in the file to control the movement of the beam.

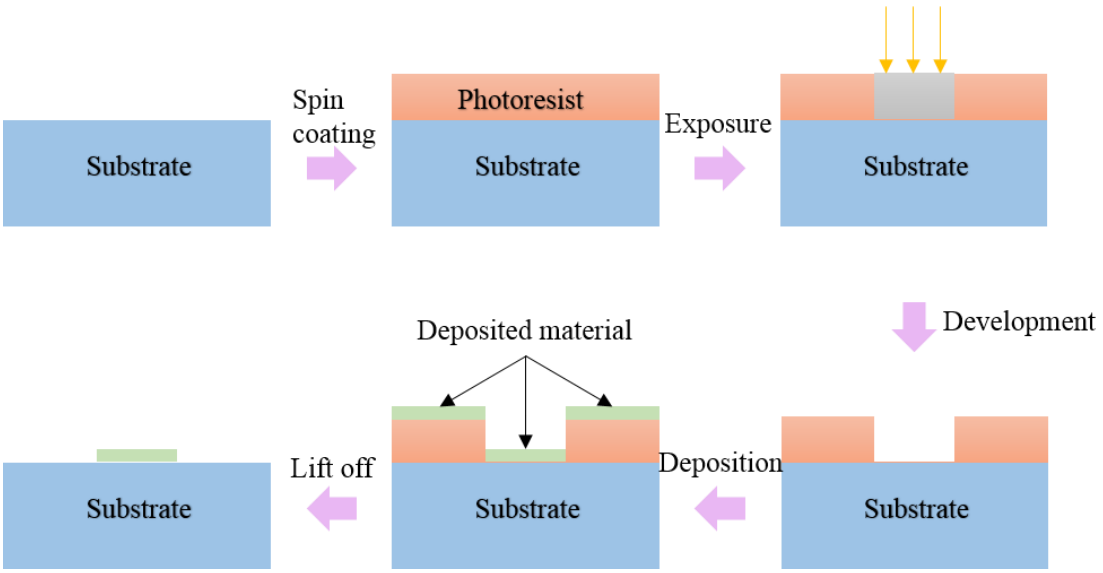

Figure 5.6 Schema of the standard EBL process[28].

Secondly, because of the restricted focus length of the electron beam, a high surface flatness is needed for the sample. Thus, the commercial UNCD wafer was carefully cleaned: sonicating in acetone for 10 mins, rinsing in IPA, blowing dry under nitrogen. The cleaned wafer was subsequently spin coated in the speed of 3000rpm with bilayer resists (50nm EL3/150nm PMMA A2) by using a spin-coater (SUSS Delta 80RC). EL stands for the ethyl lactate solvent for copolymer resists, whilst PMMA is dissolved in anisole (notated as "PMMA A"). After direct writing, the sample was developed using the M/I 1:3 (1:3 MIBK to IPA) developer so that resists on the electron-beam-exposed region are entirely removed. The sample is then ready for the following deposition. The thickness of the deposited layer is usually 1/3-1/2 of the resist thickness. Finally, the lift-off step was carried out to remove all resists and keep only the metal pattern remained. The sample was immersed in acetone for 2 hours followed by a 30s ultrasonic bath.

Fig. 5.7 shows the pattern design and the experimental results of the EBL process under 100kV acceleration voltage. Two separate layers were contained in the KLayout design (see Fig. 5.6(a)). Due to the difference in size and resolution requirements, independent beam apertures and beam currents were utilized in the exposure for each layer. For the 1st layer, a small-aperture beam whose current is 5-10nA was applied to achieve 80nm resolution, whilst for the 2nd layer, a large-aperture beam whose current is 100nA was

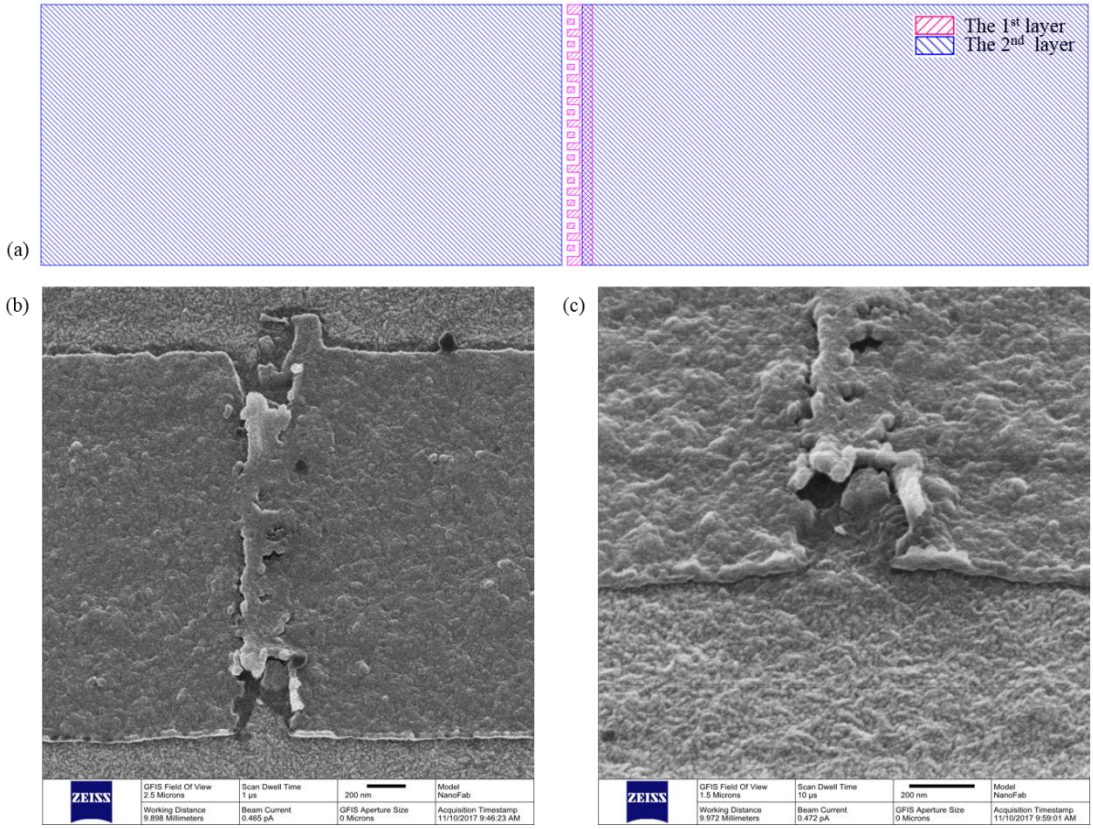

Figure 5.7 The EBL pattern on the UNCD sample. (a) The KLayout design of patterns on the UNCD surface. The red/blue colour denotes the 1st/2nd exposure layer. (b) The top and (c) the side view of the sample surface after the lift-off. Both images are obtained by HIM.

applied to efficiently scan the two 4um×2um rectangular areas. Four doses were tested, which are 500uC/cm^2, 600uC/cm^2, 700uC/cm^2, and 800uC/cm^2. It turns out that the dose does not significantly affect the ultimate result. The helium ion microscopy (HIM) images, obtained by using the ORION NanoFab Helium Ion Microscopy, showed in Fig. 5.6(b) and (c) are based on the dose of 700uC/cm^2. It can be clearly observed that the lift-off was not successful in the fine channel area. The fact that Ni coverage exists between the two large pads (marked in blue in Fig. 5.6(a)) means graphene will grow in the same position, resulting in the lack of the resonant tunneling channel. The resist

collapse is thought to be the cause of the problem, therefore, more concentrated resists (such as PMMA A4) are suggested to be used. Compared to the PMMA A2, PMMA A4 offers an extra thickness of 100nm with the same spin speed[29], and is capable of providing stronger support to the deposited Ni layer. The accomplishment of an effective EBL process is a major target in future work.

5.3. Conclusion

In summary, a process has been demonstrated in this chapter to realize the direct growth of high-quality GQD structure in the UNCD wafer. The RTA method has been proved to be able to transform diamond into graphene layers without introducing any transfer step. The performance of graphene layers is confirmed by Raman spectroscopic characteristics. Furthermore, the EBL technique is specifically discussed for the achievement of the ultimate GQD structure, and an increase in the concentration of photoresists is suggested in future work for satisfactory experimental outcomes.

References

1. Bonaccorso, F., Sun, Z., Hasan, T. & Ferrari, A. C. Graphene photonics and optoelectronics. *Nat. Photonics* **4,** 611–622 (2010).
2. Liao, L. *et al.* High-speed graphene transistors with a self-aligned nanowire gate. *Nature* **467,** 305–308 (2010).
3. Balandin, A. A. Thermal properties of graphene and nanostructured carbon materials. *Nat. Mater.* **10,** 569–581 (2011).
4. Wang, X. & Shi, Y. CHAPTER 1:Fabrication Techniques of Graphene Nanostructures. in *CHAPTER 1:Fabrication Techniques of Graphene Nanostructures* 1–30 (2014).
5. Berger, C. *et al.* Ultrathin epitaxial graphite: 2D electron gas properties and a route toward graphene-based nanoelectronics. *J. Phys. Chem. B* **108,** 19912–19916 (2004).
6. de Heer, W. A. *et al.* Epitaxial graphene. *Solid State Commun.* **143,** 92–100 (2007).
7. Emtsev, K. V. *et al.* Towards wafer-size graphene layers by atmospheric pressure graphitization of silicon carbide. *Nat. Mater.* **8,** 203–207 (2009).

8. Kim, J. *et al.* Layer-Resolved Graphene Transfer via Engineered Strain Layers. *Science* **342,** 833–836 (2013).
9. Son, M., Lim, H., Hong, M. & Choi, H. C. Direct growth of graphene pad on exfoliated hexagonal boron nitride surface. *Nanoscale* **3,** 3089–3093 (2011).
10. Tang, S. *et al.* Nucleation and growth of single crystal graphene on hexagonal boron nitride. *Carbon* **50,** 329–331 (2012).
11. Wang, G. *et al.* Direct Growth of Graphene Film on Germanium Substrate. *Sci. Rep.* **3,** 2465 (2013).
12. Lee, J.-H. *et al.* Wafer-Scale Growth of Single-Crystal Monolayer Graphene on Reusable Hydrogen-Terminated Germanium. *Science* **344,** 286–289 (2014).
13. Levinshtein, M. E., Rumyantsev, S. L. & Shur, M. S. *Properties of Advanced Semiconductor Materials: GaN, AIN, InN, BN, SiC, SiGe*. (John Wiley & Sons, 2001).
14. Auciello, O. *et al.* Are Diamonds a MEMS' Best Friend? *IEEE Microw. Mag.* **8,** 61–75 (2007).
15. Kaloni, T. P. & Mukherjee, S. COMPARATIVE STUDY OF ELECTRONIC PROPERTIES OF GRAPHITE AND HEXAGONAL BORON NITRIDE (h-BN) USING PSEUDOPOTENTIAL PLANE WAVE METHOD. *Mod. Phys. Lett. B* **25,** 1855–1866 (2011).
16. Francis, A., Abdu, S., Haruna, A. & Eli, D. Computation of the Cohesive Energies of NaCl, SiO2 and Al Using Density Functional Theory. *Phys. Sci. Int. J.* **11,** 1–9 (2016).
17. Nelson, W. E., Halden, F. A. & Rosengreen, A. Growth and Properties of β-SiC Single Crystals. *J. Appl. Phys.* **37,** 333–336 (1966).
18. Pernot, J. *et al.* Hall electron mobility in diamond. *Appl. Phys. Lett.* **89,** 122111 (2006).
19. Burzo, M. G., Komarov, P. L. & Raad, P. E. Thermal transport properties of gold-covered thin-film silicon dioxide. *IEEE Trans. Compon. Packag. Technol.* **26,** 80–88 (2003).
20. Gritsenko, V. A. Hot electrons in silicon oxide. *Phys.-Uspekhi* **60,** 902 (2017).
21. Ouyang, T. *et al.* Thermal transport in hexagonal boron nitride nanoribbons. *Nanotechnology* **21,** 245701 (2010).

22. Wei, L., Kuo, P. K., Thomas, R. L., Anthony, T. R. & Banholzer, W. F. Thermal conductivity of isotopically modified single crystal diamond. *Phys. Rev. Lett.* **70,** 3764–3767 (1993).

23. Berman, D. *et al.* Metal-induced rapid transformation of diamond into single and multilayer graphene on wafer scale. *Nat. Commun.* **7,** 12099 (2016).

24. Wu, Y. *et al.* High-frequency, scaled graphene transistors on diamond-like carbon. *Nature* **472,** 74–78 (2011).

25. García, J. M. *et al.* Multilayer graphene grown by precipitation upon cooling of nickel on diamond. *Carbon* **49,** 1006–1012 (2011).

26. Cooil, S. P. *et al.* Iron-mediated growth of epitaxial graphene on SiC and diamond. *Carbon* **50,** 5099–5105 (2012).

27. Bragg, W. H. & Bragg, W. L. The reflection of X-rays by crystals. *Proc R Soc Lond A* **88,** 428–438 (1913).

28. Han, G. *et al.* Infrared spectroscopic and electron microscopic characterization of gold nanogap structure fabricated by focused ion beam. *Nanotechnology* **22,** 275202 (2011).

29. Shamsuddin, L., MdIzah, S. S. & Mohamed, K. Comparative Study of PMMA 120K and 996K for Electron Beam Lithography Application. *Aust. J. Basic Appl. Sci.* 5 (2014).

30. Wu, R. *et al.* Edge-epitaxial Growth of Graphene on Cu with a Hydrogen-free Approach. *Chem. Mater.* (2019).

6. CONCLUSIONS AND FUTURE WORK

This thesis has put forward a novel thought for the definition of nanoelectronic systems. By taking advantages of emerging 2D materials, a platform has been built for the fulfillment of thoroughly planar electronic devices. Based on the definition, studies have been made on a variety of nanoscale electronic devices obtaining interesting characteristics. This chapter presents a brief statement of the main points in this thesis as well as discusses the possible application of 2D materials in the future. It is hoped that this thesis work will make certain contribution to the further development of nanoelectronics.

6.1. Conclusions

In this thesis, the concept of NDR effect and its influence to GQD-based electronic devices (particularly, energy filters and memristors) have been explored. The GQD structures have been simulated, analysed, and partially fabricated. The quality of the produced thin films has been examined. The primary outcomes and observations are listed as follows:

I. Extended Hückel theory has been applied in the software simulation to calculate the material intrinsic features including the electronic band structure as well as device properties including the current-voltage characteristics, the transmission spectrum, the local density of states, and so forth. This semi-empirical simulation method shortens the total calculation period but still maintains the accuracy and reliability. It is suggested that the same simulation approach can be used in the efficient analysis of graphene-based structure models.

II. The negative differential resistance effect has been investigated and exploited to produce novel devices. The discrete energy level owing to the spatial confinement on quantum dots is the key element that gives rise to the effect. As is closely related to the resonant tunneling mechanism, this effect has been widely utilized in modern electronics. For example, due to their fast switching speed and bi-stability, NDR devices are functional in static memory circuits and high-frequency oscillator systems. In addition, they are also applied as energy filters and improve the overall energy efficiency.

III. A GQD structure has been demonstrated to be capable of decreasing the energy and power dissipation in the system at room temperature, which means the costly cryogenic technique can be avoided. The high electron/hole mobilities and prominent thermal performance make graphene an advantageous material for energy filters. Based on the simulation, the impact of device geometry on the systematic signal-to-noise ratio has been presented. This relationship suggests the flexibility of the GQD structure design, since it is possible to apply adjustments on the device for the purpose of meeting corresponding practical demands.

IV. A two-terminal all GQD-based resistive memory device, whose switching mechanism depends on the resonant electron tunneling, has been proposed. The generalized definition for resistive memories has been described. Analyses have been made on indicating the viability of control on memory characteristics including the number and noise margin of states, which is beneficial to promote the device flexibility. Three-terminal devices have also been designed to achieve multiple states as well as increase the systematic tunability. Finally, comparisons on different material-based memory concepts have been made to prove the exceptional performance of the volatile GQD memristors.

V. A carbon segregation method has been utilized in the fabrication of the GQD-based device with a commercial UNCD wafer being the substrate. Proved by the Raman spectroscopy, uniform graphene films with high quality have been produced via the rapid thermal annealing technique. In addition, the e-beam lithography has been applied on the UNCD surface to prepare the GQD pattern. It is suggested that the density of resists (especially photoresists) can greatly affect the outcome of the lift-off, which will guide the direction of future work.

6.2. Future Work

The progress in graphene research has been astonishingly fast since 2004. A tremendous number of devices have been fabricated and applied to numerous applications. As discussed in this thesis, GQDs, as an prominent constituent of graphene derivatives, provide multiple benefits due to their special properties in electronics, optics, mechanics, and so forth[1,2]. Even though elaborate theoretical and experimental studies have provided encouraging ideas for feasible applications, the research on GQDs is still facing many challenges.

On the one hand, it is indispensable to further enhance the quality of the synthesized graphene. The graphene synthesis has experienced many periods, including the simple mechanic exfoliation of graphite, the direct deposition based on catalyst-induced chemical reactions, the optimization of thermal annealing processes with precise requirements being made on the substrate[3]. However, the limit on the synthetic techniques has far from ideal. Considering the direct growth method mentioned in this thesis, the absolute elimination of residual Ni on the surface of UNCD is important,

therefore practical purification approaches are necessary to guarantee the quality of the UNCD/graphene interface. Besides, as the size and edge state of quantum dots are key impact factors to the GQD properties, it is significant to develop innovative strategies in the accurate control of GQD synthesis. Apart from the Raman spectroscopy, techniques such as high-resolution TEM, SEM and AFM can be proper tools for presenting more detailed GQD characteristics including the layers, the crystal structure, the surface state, *etc.*

On the other hand, mass production methods need to be developed for commercially feasible technologies in the GQD production. Apart from energy filters and memristors, GQDs have been demonstrated promising in many other fields[4–6]. Nevertheless, the thriving development of GQDs in these areas requires wafer scale production that is free of defects and free of grain boundaries, *etc*[2]. Current technologies have not yet been able to realize such performances. Thus, a lot of work remains to be done for the ultimate realization of graphene thoroughly substituting silicon as the most commonly used commercial material. Graphene and its derivatives (especially GQD) will undoubtedly still be one of the most important research topics for years to come.

References

1. Geim, A. K. & Novoselov, K. S. The rise of graphene. *Nat. Mater.* **6,** 183–191 (2007).
2. Randviir, E. P., Brownson, D. A. C. & Banks, C. E. A decade of graphene research: production, applications and outlook. *Mater. Today* **17,** 426–432 (2014).
3. Allen, M. J., Tung, V. C. & Kaner, R. B. Honeycomb Carbon: A Review of Graphene. *Chem. Rev.* **110,** 132–145 (2010).
4. Cooper, D. R. *et al.* Experimental Review of Graphene. *ISRN Condens. Matter Phys.* **2012,** 1–56 (2012).
5. Tan, H., Wang, D. & Guo, Y. Thermal Growth of Graphene: A Review. *Coatings* **8,** 40 (2018).
6. Li, X., Rui, M., Song, J., Shen, Z. & Zeng, H. Carbon and Graphene Quantum Dots for Optoelectronic and Energy Devices: A Review. *Adv. Funct. Mater.* **25,** 4929–4947 (2015).